The Role of Melatonin in Amyloid Interactions with the Model Neuronal Membranes

by

Nanqin Mei

A thesis
presented to the University of Waterloo
in fulfillment of the
thesis requirement for the degree of
Doctor of Philosophy
in
Physics (Nanotechnology)

Waterloo, Ontario, Canada, 2023
© Nanqin Mei 2023

Examining Committee Membership

The following served on the Examining Committee for this thesis. The decision of the Examining Committee is by majority vote.

External Examiner:	Drew Marquardt Associate Professor, Dept. of Chemistry and Biochemistry, University of Windsor
Supervisor(s):	Zoya Leonenko Professor, Dept. of Physics and Astronomy, Dept. of Biology, Waterloo Institute for Nanotechnology, University of Waterloo
Internal Member:	Michel Gingras Professor, Dept. of Physics and Astronomy, University of Waterloo
Internal Member:	Joe Sanderson Professor, Dept. of Physics and Astronomy, University of Waterloo

Internal-External Member: Patricia Nieva
Professor, Dept. of Mechanical and Mechatronics Engineering,
University of Waterloo

Author's Declaration

This thesis consists of material all of which I authored or co-authored: see Statement of Contributions included in the thesis. This is a true copy of the thesis, including any required final revisions, as accepted by my examiners.

I understand that my thesis may be made electronically available to the public.

Statement of Contributions

I prepared Chapter 1 independently. Figures 1.1, 1.2, 1.3 and 1.4 in the Introduction section are cited from other published works and included for illustration.

I led all projects under the guidance of my supervisor, Prof. Zoya Leonenko. Collaborations are briefly acknowledged in the following text and detailed at the start of each chapter.

In Chapter 2, I collaborated with Prof. James H. Davis and Dr. Morgan Robinson. Dr. Robinson assisted with experimental setup and initial sample preparation and also contributed to the introduction section of the paper. Prof. Davis trained me on the NMR instrument and then he accomplished data collection. I collaborated with him on data analysis and the writing of the Methods and Results sections in the paper.

For Chapter 3, I designed and led the project, trained undergraduate student Jingwen Liang on the LSPR instrument, and solely undertook data analysis. Dr. Danielle M. McRae aided in writing the abstract and editing the manuscript.

Chapter 4 was entirely my work, with instrument training and data analysis insights from colleagues Carina Filice and Yue Xu. Undergraduate student Gexu Liu assisted with early data collection and preliminary data analysis. I managed the main data collection, statistical analysis, and authored the chapter.

Abstract

The amyloid cascade hypothesis has long directed research efforts in understanding the pathogenesis of Alzheimer's disease (AD), ever since it was first proposed through clinical evidence by Hardy and Higgins in 1992. Currently, amyloid-β (Aβ) species have attracted significant interest, particularly as they demonstrate profound cellular membrane toxic effects. When there is no cure for AD, the current research direction shows there is a need to develop the protective strategies. One natural molecule, melatonin, has been shown to be protective against amyloid toxicity in animal and cellular studies, while the molecular mechanisms are not well understood. One of the hypothesis is that melatonin can alter the membrane structure and thus reduce amyloid toxicity to lipid membranes. In this thesis research, how the incorporation of melatonin to the lipid membrane would change the structure of the membranes and protect the membrane from amyloid toxicity was examined.

This thesis focuses on investigations on the neuroprotective effects of melatonin against Aβ toxicity were achieved using various membrane models that mimic cellular membranes at different stages of AD. Utilizing a range of advanced nanotechnology tools including nuclear magnetic resonance (NMR), localized surface plasmon resonance (LSPR), atomic force microscopy (AFM), black lipid membrane (BLM) studies, complemented by neutron scattering, neutron reflectivity, and molecular dynamics (MD) simulations, the study explores the intricate molecular mechanisms behind melatonin's interaction with Aβ peptides. Different membrane models representing various disease states were employed to assess melatonin's multifaceted effects. The research uniquely contributes by combining these diverse techniques to offer a comprehensive understanding of the potential therapeutic role of melatonin in AD, paving the way for the development of more targeted and effective treatments. Future exploration into melatonin's interactions with various forms of Aβ aggregates may further enhance therapeutic strategies.

The research employs a range of neuronal membrane models — simple model (SPM) (DPPC/POPC/cholesterol) and complex (DPPC/POPC/cholesterol/SM/GM1) models — to elucidate the protective role of melatonin against Aβ toxicity. Each complex model represents a different disease state of membrane (healthy model (HM), early diseased model

(EDM) and late diseased model (LDM)), allowing tests on multifaceted effects of melatonin in varying biological contexts and disease states.

The studies demonstrated that melatonin changed the phase separation of lipid membranes, altered the amyloid binding to the membranes, and enhanced the resilience of membranes against amyloid-induced damage. Insights from the NMR study presented in Chapter 2 indicated that melatonin promoted DPPC/POPC phase separation in a simple lipid membrane model. The LSPR study, complemented with AFM in Chapter 3, showed that melatonin altered the amyloid binding to complex lipid membrane models. Interestingly, the intensity of this effect varied depending on the disease state, with the most pronounced protective effects of melatonin observed in EDM. The BLM study in Chapter 4 further investigated melatonin's effect on different types of amyloid-induced membrane damages. The results clearly demonstrated melatonin's ability to enhance the longevity of lipid membranes and increase the membrane's resistance to rupturing.

The advancement of knowledge on melatonin's membrane protective effects can pave the way for the development of new preventive strategies and potentially open doors for innovative therapeutic approaches.

Acknowledgements

I would like to send my deepest gratitude to my supervisor, Prof. Zoya Leonenko, for her invaluable guidance over the past six years. Her extensive knowledge, unwavering enthusiasm for research, and innate curiosity about science have been a constant source of inspiration for me. She also actively encouraged me to establish collaborations with other research groups which significantly benefits my skills in both research and task management. More than a academic supervisor, Prof. Leonenko has been supportive in my life. As an international student, navigating life and academics alone—particularly during the pandemic delays in my experimental work—has been challenging. Prof. Leonenko has always been attentive to my well-being, offering the support I needed both academically and emotionally. I feel incredibly fortunate to have had a supervisor who not only fueled my research interests but also equipped me with essential skills, guided the direction of my project, and supported my mental health.

The Waterloo Institute for Nanotechnology (WIN) graciously awarded me an annual WIN fellowship, which has provided substantial support throughout my graduate studies.

I would also like to extend my thanks to Dr. Brenda Yasie Lee, who has been both a mentor in my academic journey and a cherished friend in my life. Dr. Lee introduced me to this lab and has consistently offered unwavering support for both my academic endeavors and personal well-being. I am deeply grateful for her guidance and friendship.

I would like to further extend my gratitude to my labmates — Dr. Morgan Robinson, Dr. Danielle McRae, Carina Filice, Yue Xu, among others — who have been invaluable colleagues and friends. They have contributed to an enriching atmosphere, fostering collaborative discussions about research challenges, helping to find solutions, and collectively maintaining a well-organized lab environment. I am deeply thankful for their support.

To my beloved friends at the university, who have been pillars of support in my life. They have encouraged and uplifted me through many challenging times. Special mentions go to Junjie Yin, Tong Hong, and Yiqi Zhang, as well as all the kind individuals I have had the privilege to meet here in Waterloo. I hold great affection for each and every one of you.

Last but certainly not least, I would like to thank my parents and family. They have shaped me into a better person and equipped me with the courage and dedication to pursue knowledge. Without their solid support, I could not have achieved what I have in my life.

In the end, my deepest thanks go out to everyone who has been a part of this journey. I wish each and every one of you a wonderful and fulfilling life.

Dedication

This is dedicated to the one I love.

Table of Contents

Examining Committee Membership ii

Author's Declaration iv

Statement of Contributions v

Abstract vi

Acknowledgements viii

Dedication x

List of Figures xvi

List of Tables xxv

List of Abbreviations xxvii

1 Introduction 1

1.1 Alzheimer's Disease and Amyloid-β 1

1.2 Lipid Bilayer Membranes 3

1.3 Melatonin 9
1.4 Methods 10
1.4.1 Nuclear Magnetic Resonance 10
1.4.2 Surface Plasmon Resonance Techniques 14
1.4.3 Atomic Force Microscopy 17
1.4.4 Black Lipid Membrane 20

2 Nuclear Magnetic Resonance to Study Melatonin Effect on Lipid Phase Behaviour of DPPC/POPC/Cholesterol Lipid Membranes 22

2.1 Overview 22
2.1.1 Summary of Published Work 22
2.1.2 Contributions 23
2.1.3 Challenge and Future Directions 23
2.2 Abstract 24
2.3 Introduction 25
2.4 Materials and Methods 27
2.4.1 Sample Preparation 27
2.4.2 ^{2}H NMR 28
2.5 Results and Discussion 34
2.5.1 ^{2}H NMR Spectra and Methyl Group Quadrupolar Splitting Analysis 34
2.5.2 First Moment M_1 Analysis 45
2.5.3 Significance and Physiological Implications 46
2.6 Conclusion 48

3 Localized Surface Plasmon Resonance and Atomic Force Microscopy Study of Model Lipid Membranes and Their Interactions with Amyloid and Melatonin **50**

3.1 Overview . . . 50

3.1.1 Summary of Submitted Work . . . 50

3.1.2 Contributions . . . 51

3.1.3 Challenges and Future Directions . . . 51

3.2 Abstract . . . 52

3.3 Introduction . . . 52

3.4 Materials and Methods . . . 54

3.4.1 Lipid Membrane . . . 54

3.4.2 Aβ Solution Preparation . . . 56

3.4.3 Atomic Force Microscopy . . . 56

3.4.4 LSPR Theory and Experiments . . . 57

3.5 Results and Discussion . . . 61

3.5.1 AFM Imaging . . . 61

3.5.2 LSPR Results . . . 65

3.6 Conclusion . . . 70

4 Melatonin Affects Membrane Permeability Changes Caused by Amyloid-Membrane Interaction: A Black Lipid Membrane Study **72**

4.1 Overview . . . 72

4.1.1 Summary of the Work . . . 72

4.1.2 Contributions . . . 73

4.1.3 Challenges and Future Directions . . . 73

4.2 Introduction . . . 75
4.3 Materials and Method . . . 77
4.3.1 Lipid Membrane and Amyloid . . . 77
4.3.2 Black Lipid Membrane . . . 78
4.3.3 BLM Signal Category . . . 79
4.3.4 Data Analysis . . . 84
4.4 Results and Discussion . . . 87
4.4.1 Evaluating Trial Activity . . . 87
4.4.2 Event Count . . . 88
4.4.3 Voltage-current Curve Analysis . . . 91
4.4.4 Activity Duration . . . 97
4.5 Conclusion . . . 98

5 Thesis Conclusions **99**
5.1 Melatonin's Effect in Simple Model Membrane Phase Behaviour . . . 99
5.2 Melatonin Affects Binding of Amyloid to the Model Membranes . . . 100
5.3 Melatonin's Effect on Amyloid Induced Membrane Damage to Simple Model Membrane . . . 100
5.4 Conclusion . . . 101
5.5 Future Works . . . 101

Letter of Copyright Permission **103**

References **111**

APPENDICES **137**

A Neutron Scattering and Molecular Dynamics to Study Complex Lipid Model Membranes **138**

A.1 Overview . . . 138

A.2 Introduction to Neutron Scattering . . . 139

A.3 Introduction to Molecular Dynamics . . . 141

A.4 Experiments . . . 142

A.4.1 Neutron Scattering . . . 142

A.4.2 Molecular Dynamics Simulation . . . 143

A.5 Preliminary Results . . . 143

A.6 Next Steps . . . 144

B Neutron Reflectivity to Study Simple Model Lipid Membranes **148**

B.1 Overview . . . 148

B.2 Introduction to Neutron Reflectivity . . . 148

B.3 Experiment . . . 149

B.4 Preliminary Results . . . 151

B.5 Next Steps . . . 155

C High-Speed Atomic Force Microscopy to Study the Dynamics of the Membrane-Amyloid Interaction in the Presence and Absence of Melatonin **156**

C.1 Overview . . . 156

C.2 High-Speed Atomic Force Microscopy . . . 157

List of Figures

1.1 **Phase Transition of Lipid Membrane**. In the solid crystalline phase (L_c), lipids are tightly ordered and closely packed. The orientation of lipid hydrocarbon chains can vary, leading to a gel phase ($L_{\beta'}$). The transition from gel to fluid phase (L_α) occurs at phase transition temperature, also known as the melting point (T_m). Before this transition, there is often a pre-transition phase featuring a ripple phase ($P_{\beta'}$) with one-dimensional ripples. In the fluid phase, lipids become highly disordered, losing their lattice order, and exhibit increased lateral and rotational diffusion [1]. . . . 4

1.2 **Comparison of monolayer structure and electrical characteristics across three different models**. AFM topography images (gold) and KPFM electrical surface potential images (blue) are shown for the three model systems: healthy (A/D), early diseased model (B/E), and late diseased model (C/F). Figure is cited from Drolle *et al.* 2017 [2]. 7

1.3 **Comparison of Aβ incubation on the three model membranes for 1 and 6 hours**. AFM images in liquid show different Aβ accumulation between 1 and 6 hours of incubation time on healthy (A/D), early diseased model (B/E), and late diseased model (C/F). Figure is cited from Drolle *et al.* 2017 [2]. 8

1.4 **Molecular Dynamics Simulations** of (A) DPPC and (C) DOPC bilayers with and without melatonin. Melatonin molecules are shown in orange, and simulation for the bilayers with melatonin are shown on the right. [1] 10

1.5 **Energy Levels for Hydrogen and Deuterium Nucleus** when place in an external magnetic field $\vec{B}_0$. The gyromagnetic value of hydrogen nucleus is larger than that of deuterium. 12

1.6 **Schematic of SPR Working Principle**. Incident polychromatic light is reflected on the metal/water interface, with partial energy transferred to SPP. The light with the wavelength matched the resonance condition is absorbed by the SPP and therefore appears as a dark band in the reflected spectrum. When molecules bind to the interface, the absorbed wavelength shifts. The measurement on $\Delta\lambda$ indicates the binding activity happens on the interface. 16

1.7 **Schematic Diagram of LSPR.** Electron cloud of the gold nanoparticles oscillates with a static electric field, generating localized surface plasmon. . 17

1.8 **AFM Imaging Schematic.** A laser shines on the back of the cantilever and its reflection shines on a detector. The deflection of the cantilever results in a shift on the reflected spot on the detector. 18

1.9 **Force Curve and Imaging Modes of AFM**. In the attractive region, the net force between the cantilever tip and the sample surface increases as the attractive force increases. In the repulsive region, the net force increases with the increasing repulsive force. A minimum potential point occurs at a distance of d_m, where the attractive and repulsive forces balance each other. Contact mode takes place in the repulsive region, intermittent contact mode covers both repulsive and attractive regions, and noncontact mode occurs in the attractive region. 19

1.10 **Schematic of BLM.** Two electrodes are placed in the buffer on the opposite sides of the middle barrier, and an electric bias is applied. A lipid membrane is spread over the aperture and covers it entirely. Ion current occurs when there are holes or discontinuities in the membrane, and this can be recorded in the circuit. [2] 21

2.1 **Schematic of the Simple Model System**. Lipid bilayer membrane consisting of POPC, DPPC, cholesterol (*yellow*) and melatonin (*blue*), and their molecular structures showing on the right: (A) POPC, (B) DPPC, (C) cholesterol and (D) melatonin. The coexistance of ℓ_o and ℓ_d phases is represented. Liquid ordered phases have tails that are aligned and more rigid than disordered tails. The orientation of cholesterol and melatonin predicted from MD simulations is shown [3], with melatonin decreasing the lipid ordering and cholesterol having opposing effects. 27

2.2 **Calibration Curve of Accurate Temperature VS Set Temperature in the NMR Spectrometer**. The function of the fitted curve is expressed as: $T_A = A + B * T_{set} + C * {T_{set}}^2 + D * {T_{set}}^3$. 30

2.3 **^{2}H NMR Spectra of Lipid Membrane without Melatonin.** (A) pure POPC-d_{31}, (B) POPC-d_{31}/DPPC/cholesterol, (C) pure DPPC-d_{62} and (D) DPPC/POPC-d_{62}/cholesterol. The lipid membranes in B and D are SPM. 35

2.4 **^{2}H NMR Spectra of POPC-d_{31}/DPPC/cholesterol Lipid Membranes** with (A) 5% melatonin and (B) 10% melatonin. ^{2}H-NMR spectra of DPPC/POPC-d_{62}/cholesterol lipid mixture with (C) 5% melatonin and (D) 10% melatonin. The molar proportions of the lipids in all of the four mixtures are 3:3:2. 36

2.5 **Expansion of Methyl Group Component of the ^{2}H NMR Spectra of SPM.** The left column shows the methyl group spectra observed on samples with POPC-d_{31} and the right column shows the methyl group spectra observed on samples with DPPC-d_{62}. The melatonin concentration is 0%, 5%, and 10% from top to bottom. 40

2.6 **Methyl Group Quadrupolar Splittings of Samples with POPC-d_{31} (*red*) and Samples with DPPC-d_{62} (*black*)**, shown with temperature dependence. (A) shows the quadrupolar splitting values of pure deuterated lipid samples and (B), (C), (D) show that of DPPC/POPC/cholesterol lipid mixture at molar proportions of 3:3:2 with 0%, 5%, and 10% melatonin, respectively. Lower values of splittings correlate with less order of the lipid tails, while higher values of splittings indicate the opposite way. 43

2.7 **First Moments of the ^{2}H Spectra** of Pure samples (*blue*) and lipid mixture of DPPC/POPC/cholesterol at molar proportions of 3:3:2 with 0% (*black*), 5% (*red*), and 10% (*green*) melatonin, shown with temperature dependence. Samples with POPC-d_{31} are shown in (A), samples with DPPC-d_{62} are shown in (B). 44

3.1 **Schematic of the LSPR Induced by Electric Field** The electric field associated with the incident light induces the electron cloud of the gold nanoparticles to oscillate collectively to generate a localized surface plasmon. 58

3.2 **The LSPR Experiment Design and Measurement Principle** (A) Schematic view of an LSPR sensing surface used in the experiment. A lipid membrane assembles onto the GNP sensor. The solution containing Aβ flows over this membrane, leading to the accumulation of oligomers on the surface. Incident light travels through the sensing area, starting from the GNP side, and the transmitted light is then measured on the opposite side. Simplified model demonstrating the adsorbed layers producing LSPR signals for analysis is shown on the right. (B) The initial absorption spectrum of the transmitted light is shown as a black curve. As layers of molecules accumulate on the sensor, the absorption peak of the spectrum shifts, shown as the orange curve. This shift, represented as $\Delta\lambda$, is recorded for analysis. 58

3.3 **LSPR Sensorgram.** LSPR sensogram shows the change in wavelength of absorbance peak VS time after each injection: first is the liposome solution and formation of lipid bilayer followed by amyloid injection and build up of amyloid layer on the top of the membrane. Each pair of blue dashed line and circle indicates the time point of each solution injection. The two orange arrows indicate the respective sensor responses due to each layer formation. The responses are labeled as $\Delta\lambda_{mem}$ and $\Delta\lambda_{A\beta}$, respectively. The orange dashed lines indicate where the baseline of each injection response is taken. 61

3.4 **AFM Topography Images** of (A) an LSPR sensor surface covered with GNPs, (B) a supported healthy model (HM) membrane formed on mica, and (C) the HM membrane supported on the GNP covered LSPR sensor. Each image size is 1 μm $\times$ 1 μm. The cross-section plot below each image shows the height profile along the white line on the AFM image. 63

3.5 **AFM Topography Images of Supported Early Diseased Model (EDM) Membranes on Mica with and without Amyloid.** [A] untreated EDM membrane and [B] treated with 50 μM amyloid for 60 minutes. Images [C] to [F] are enlarged images of the black square area shown in [B] after amyloid treatment of 60 minutes, 90 minutes, 120 minutes and 180 minutes. 65

3.6 **Lipid Membrane Thickness Profiles (T_{mem})** of HM, EDM, and LDM membranes (from left to right). The vertical axis is unitless because the membrane thickness and l_d are both in nanometer units. The red bars show the control group while the blue bars show the experimental group treated with 400 μM melatonin. 68

3.7 **Adsorbed Amyloid Layer Thickness Profiles ($T_{A\beta}$)** on HM, EDM, and LDM membranes (from left to right). The vertical axis is unitless because the membrane thickness and l_d are both in nanometer units. The red bars show the control group while blue bars show the experimental group treated with 400 μM melatonin. 69

3.8 **$T_{mem}/T_{A\beta}$ of HM, EDM, and LDM membranes** (from left to right). Red bars show the control group, and blue bars show the experimental group treated with 400 μM melatonin. 71

4.1 **An Illustration of the BLM Experiment Setup**. The same amount of solution was added to both side of the Teflon barrier. A pair of electrodes, connected to a voltage bias, was placed inside the solution on each side of the barrier. Amyloid was injected on only one side of the barrier and interact with the lipid membrane that spreads across the central hole on the Teflon barrier. A closer view of this interaction is shown on the right of the figure. The ammeter records the current throughout an experiment. 79

4.2 **Representative BLM Trial Plot.** The recorded current and the applied voltage are plotted versus time (min). Amyloid was introduced to the bath at 50 mV, incubated for 15 minutes, and then measured for 15 minutes at 90 mV. This was followed by measurements at incremented voltages of 100, 110, and 120 mV, each for 5 minutes. There are multiple types of signals included in this example, and the detailed explanations are provided in the BLM Signal Category section. 80

4.3 **Schematic of the Interaction between Aβ Oligomers/Aggregates and the Lipid membrane**: Individual oligomers can penetrate into the tail region of the membrane (C), while small aggregates may accumulate on the membrane surface (A), creating indentations (B). As the aggregates grow to larger sizes, they can disrupt membrane continuity, forming either stable ion channels with cylindrical structure (F)) or less stable pores (E). This process can lead to increased lipid loss, contributing to further damage. Over time, this can result in hole formation (D) and, ultimately, membrane rupture. 81

4.4 **A Sample Spike Signal.** The spike signal occurs at time (t) = 0.7 s and lasts for approximately 6 ms, with a peak current at 30 pA. 82

4.5 **Sample Instability Signals.** Signals between time (t) = 0 s to 8 s and between 17 s to 25 s are the major instabilities where numerous spike signals overlap. The signal between these two major instabilities has an unstable baseline. 82

4.6 **A Sample Step Signal.** Current elevates at t = 3 s. Then the current reduces at t = 12 s to a new baseline which is higher than the original baseline before the step occurs. 83

4.7 **Sample Multilevel Signals.** There are three consecutive multilevel signals that occur, during t = 2 s to 2.8 s, 2.8 s to 3.5 s and 3.5 s to 4.5 s. 83

4.8 **A Sample Erratic Signal.** The current is over 1 nA and keep increasing without a stable baseline. 84

4.9 **Event Distributions** for the control, with 50 μM melatonin and with 100 μM melatonin groups. 90

4.10 **I-V Curves of the Inactive Trials in the Control Group.** The voltages are 50 mV, 90 mV, 100 mV, 110 mV and 120 mV. Linear fit for each plot is shown in blue, and the slope is labeled in each plot. 92

4.11 **I-V Curves of the Inactive Trials in the Group with 50 μM Melatonin.** The voltages are 50 mV, 90 mV, 100 mV, 110 mV and 120 mV. Linear fit for each plot is shown in blue, and the slope is labeled in each plot. 92

4.12 **I-V Curves of the Inactive Trials in the Group with 100 μM Melatonin.** The voltages are 50 mV, 90 mV, 100 mV, 110 mV and 120 mV. Linear fit for each plot is shown in blue, and the slope is labeled in each plot. 93

4.13 **I-V Curves of the Active Trials in the Control Group.** The voltages are 50 mV, 90 mV, 100 mV, 110 mV and 120 mV. Linear fit for each plot is shown in red, and the slope is labeled in each plot. 93

4.14 **I-V Curves of the Active Trials in the Group with 50 μM Melatonin.** The voltages are 50 mV, 90 mV, 100 mV, 110 mV and 120 mV. Linear fit for each plot is shown in red, and the slope is labeled in each plot. 94

4.15 **I-V Curves of the Active Trials in the Group with 100 μM Melatonin.** The voltages are 50 mV, 90 mV, 100 mV, 110 mV and 120 mV. Linear fit for each plot is shown in red, and the slope is labeled in each plot. 94

4.16 **Inactive and Active Trial Conductances.** The unit of conductance is 10^{-12} S (pS). The distribution of the data are shown in box plots with the mean value represented by a half filled square. The violin curve associated with each box plot shows the data point density. Each data point is shown as a black diamond. 96

4.17 **Amyloid Activity Duration.** The distribution of the data were shown in box plots with the mean value represented by a half filled square. The violin curve associated with each box plot shows the data point density. Each data point is shown as a black diamond. 97

A.1 Rendering of the HM membrane that gives lateral arrangements of lipid molecules. 144

A.2 Rendering of the EDM membrane that gives lateral arrangements of lipid molecules. 144

A.3 A side view on the rendering of the HM membrane. 144

A.4 A side view on the rendering of the EDM membrane. 144

A.5 An illustration of the normalized mass density profile for the each composite lipid for (Left) HM, and (Right) EDM. The symmetric peaks indicate the location of the PO_4 groups (DPPC, POPC and DPSM) as well as the GM_1 bead from DPG1. The location of the peaks can be considered to be a measure of the lipid dependent membrane thickness. 145

A.6 Thickness maps for the membrane patch of HM. The upper and lower leaflet were separated at each time-step. The highest and lowest point was determined for each lipid and the membrane thickness at every point was calculated by subtracting both values. 146

A.7 Thickness maps for the membrane patch of EDM. The upper and lower leaflet were separated at each time-step. The highest and lowest point was determined for each lipid and the membrane thickness at every point was calculated by subtracting both values 147

B.1 Illustration of reflections of an incident beam on silicon/membrane and membrane/water interfaces. 150

B.2 Neutron reflectivity profiles and fitted curves of the SPM lipid membrane before adding Aβ. 152

B.3 Density profiles of each layer from fitted curves before adding Aβ. 153

B.4 Neutron reflectivity profiles and fitted curves of the SPM lipid membrane after adding Aβ. 154

B.5 Density profiles of each layer from fitted curves after adding Aβ. 155

List of Tables

1.1 **Lipid Compositions of the Three Complex Lipid Models and the Simple Model** mimicking different disease states of neuronal cell membranes in AD: healthy model (HM), early diseased model (EDM), and late diseased model (LDM). The ratios are shown in weight. Adapted from Drolle *et al.* 2017 [2]. The simple model removed SM and GM1 from the neuronal models. 6

2.1 **Slopes (dM_1/dT) of the Linear Regression Lines Shown in Fig 2.7 for All the Samples.** 46

3.1 **Lipid Compositions of the Three Model Membranes** mimicking different disease states of neuronal cell membranes in AD: healthy model (HM), early diseased model (EDM), and late diseased model (LDM) membranes. The ratios are shown by weight. Adapted from Drolle *et al.*, 2017 [2]. . . . 55

3.2 **Roughness and Height Difference (Δh) for the AFM Images Shown in Figure 3.4.** Roughness was calculated by built-in statistical functions in Gwyddion software [4], which is computed from the second central moment of data values. The average Δh is calculated from the difference between the minimum and maximum values of the image, also using the functions from Gwyddion [4]. 64

3.3 **The Thicknesses Profiles of Lipid Membrane Models (T_{mem}) and Adsorbed Amyloid Layers ($T_{A\beta}$) with and without Melatonin.** This table shows the thicknesses of each layer calculated from LSPR response using Equation (3.4) for each membrane model. The thickness values are divided by the evanescent field decay length l_d, denoted as a dimensionless parameter T as the thickness profile [see Equation (3.5)], and the table is divided into three parts. Part 1 and Part 2 show T of the membrane (T_{mem}) and adsorbed amyloid ($T_{A\beta}$) layer, respectively. Part 3 shows the ratio of amyloid layer thickness to the membrane thickness $T_{A\beta}/T_{mem}$. The table includes the thickness or ratio results of the control group (without melatonin) and the melatonin group (with 400 μM melatonin). 67

4.1 **Active/Inactive Trial Count.** Active trials with events and inactive trials without events were counted and the percentages of the active trials are included in the last column. The number of incomplete trials due to membrane rupture are shown in the brackets in the active trials column. . 88

4.2 **Event Count for Complete Active Trials.** Trials analyzed are all the complete active trials of each group. Event frequency is calculated as total events divided by total trials. 89

4.3 **Mean Values of the Conductance of the Inactive and Active Trials.** The values are represented as average ± standard error. 95

A.1 **Lipid Compositions of the Lipid Model Membranes** mimicking different disease states of neuronal cell membranes in AD: HM, and EDM membranes. The ratios are shown by weight. Adapted from Drolle *et al.*, 2017 [2]. 142

B.1 **List of Four Contrasts of Liquid Buffers and Their Composition**. . 150

List of Abbreviations

ℓ_d liquid-disordered xviii, 3, 24–27, 31–34, 36–39, 41, 42, 45, 46, 48

ℓ_o liquid-ordered xviii, 3, 24–27, 31–34, 37–39, 41, 42, 45, 48

Aβ amyloid-β vi, xiii, xvi, xxi, xxiv, 1–3, 5, 6, 8, 9, 24, 50, 52–54, 56, 59, 60, 70, 75–77, 79, 81, 100, 102, 152–155

AD Alzheimer's disease vi, xxv, 1–3, 5, 6, 9, 20, 24, 50–55, 68, 71, 75–77, 101

AFM atomic force microscopy vi, vii, xvii, xx, xxv, 5, 17–20, 50, 52, 54–56, 61–64, 69, 71, 100, 157

APP amyloid precursor protein 2, 53

BLM black lipid membrane vi, vii, xvii, xxi, 20, 21, 72–74, 76–80, 84, 85, 98, 100, 102

DLPC 1,2-dilauroyl-sn-glycero-3-phosphocholine 5

DOPC 1,2-dioleoyl-sn-glycero-3-phosphocholine 5, 9

DOPS 1,2-dioleoyl-sn-glycero-3-phospho-L-serine 77

DPPC 1,2-dipalmitoylphosphatidylcholine vi, vii, xviii, xix, 5, 6, 9, 22–24, 26–29, 32, 33, 35–46, 48, 53–55, 66, 73, 76, 77, 99, 100, 142

EDM early diseased model vi, vii, xx, xxiii, xxv, xxvi, 6, 55, 62, 63, 65–71, 100, 141–145, 147, 157

EFG electric field gradient 13

GM1 ganglioside M1 vi, xxv, 5, 6, 54, 55, 99, 142

GNP gold nanoparticles xix, xx, 57–63, 65, 70

HEPES 4-(2-hydroxyethyl)-1-piperazineethanesulfonic acid 55, 77

HFIP hexafluoroisopropanol 56, 77

HM healthy model vi, xx, xxiii, xxv, xxvi, 6, 55, 62, 63, 65–71, 76, 141–146, 157

LDM late diseased model vii, xx, xxv, 6, 55, 66–71

LSPR localized surface plasmon resonance vi, vii, xiii, xvii, xix, xx, xxvi, 14, 16, 17, 20, 50–52, 54–65, 67, 70–72, 100, 102

LUV large unilamellar vesicle 102

NAS N-Acetylserotonin 53

NMR nuclear magnetic resonance vi, vii, xii, xviii, 6, 10–13, 22–26, 28, 29, 31, 33–38, 40, 48, 99, 101, 102

NP nanoparticle 14, 16

POPC 1-palmitoyl-2-oleoyl-sn-glycero-3-phosphocholine vi, vii, xviii, xix, 5, 6, 22–24, 26–29, 33, 35–48, 53–55, 66, 73, 76, 77, 99, 100, 142

POPE 1-palmitoyl-2-oleoyl-sn-glycero-3-phosphoethanolamine 77

RF radio frequency 12

SLB supported lipid bilayer 55

SM sphingomyelin vi, xxv, 5, 6, 54, 55, 99, 142

SPM simple model vi, xviii, xxiv, 35, 40, 99, 150–152, 154, 157

SPP surface plasmon polaritons xvii, 14–16

SPR surface plasmon resonance xvii, 14–16

TIR total internal reflection 14

Chapter 1

Introduction

1.1 Alzheimer's Disease and Amyloid-β

Alzheimer's disease (AD) is a progressive neurodegenerative disorder that accounts for approximately 60-80% of dementia cases worldwide, making it the most common form of dementia for the elderlies [5, 6]. It is characterized by gradual cognitive decline, including impairments in memory, thinking, and behaviour, that interferes with daily life and activities [6, 7, 8]. The cause of AD is complex and multifactorial, involving a combination of genetic, environmental, and lifestyle factors. Despite its high prevalence and the significant symptoms on patients, there is currently no cure for AD [6].

AD was first identified by German psychiatrist Alois Alzheimer in 1906, who described the distinct neuropathological features of the disease: there were altered fibrils within cells that lead to disintegration [9]. Later research found that neurofibrillary tangles and neuritic plaques are commonly found in the cerebral cortex of the elderly, often due to normal aging, while amyloid, which forms the core of the plaques, is a hallmark of AD [9]. The neuropathological changes in AD are believed to begin decades before the onset of clinical symptoms, with amyloid-β (Aβ) accumulation being one of the earliest pathological changes. Amyloid cascade hypothesis postulates that the accumulation of Aβ in the brain is the primary event driving AD pathogenesis [10]. This hypothesis has been the leading

theoretical framework guiding AD research and drug discovery efforts for nearly three decades.

Aβ is a small peptide that is produced through the sequential cleavage of the amyloid precursor protein (APP), by β-secretase and γ-secretase [11]. There are two primary isoforms of Aβ found in the brain, Aβ (1-40) and Aβ (1-42), with the latter being more prone to deposition and therefore more commonly found in amyloid plaques [6, 11]. Over time, Aβ peptides aggregate to form soluble oligomers, which are believed to be the most neurotoxic species, and further to insoluble fibrils, which deposit in the brain to form amyloid plaques [12, 13, 14, 15]. These aggregates disrupt cellular processes, leading to synaptic dysfunction, neuronal death, and ultimately, the clinical symptoms of AD.

Accumulating evidence suggests that the cellular membrane is a crucial site of Aβ action. Aβ can bind to the lipid membrane and accumulate on the membrane surface, triggering a variety of damage on the lipid membrane, ultimately leading to cellular dysfunction and death [15]. For instance, surface-adsorbed Aβ oligomers can cause lipid peroxidation [16, 17]. They can form pore-like structures or ion channels in the membrane, allowing uncontrolled passage of ions and small molecules across the membrane [2, 18, 19]. They can also act as surface detergents, creating holes in lipid membranes by extracting lipid molecules [20]. Each of these interactions can profoundly affect cell membrane integrity and function, potentially leading to cellular dysfunction and neuronal death.

Previously in Leonenko's lab (Drolle *et al.*) it has been shown that the changes in the membrane structure are the key factor to amyloid toxicity [2]. This opens new possibilities to investigate the role of the lipid membranes and to develop new preventive strategies to protect cellular membrane from amyloid toxicity in AD, making it the main motivation of my studies. In the following sections, I will provide a review of lipid membranes, investigating their critical role in cellular function and their susceptibility to disruption by Aβ. A thorough exploration of these aspects could shed light on the critical yet intricate relationship between Aβ, lipid membranes, and the devastating neurodegeneration witnessed in AD.

1.2 Lipid Bilayer Membranes

The cell membrane, or plasma membrane, is a biologically complex structure primarily composed of lipids and proteins [21]. The primary constituents are phospholipids, sphingolipids and cholesterol [22]. The structure and biophysical properties of the lipid bilayer, including fluidity, phase behaviour, permeability, and lateral organization, play pivotal roles in numerous cellular processes, emphasizing its fundamental importance in cellular biology [23]. Lipid bilayer membranes formed with lipid species possess ordering properties that are dependent on the phases of lipid molecules (shown in Figure 1.1). The lipid membrane can stay in the gel ($L_{\beta'}$) phase below the melting temperature, where the lipid molecules are closely packed and have limited mobility. When the temperature is higher than the melting point, the lipid membrane becomes in the fluid (L_α) phase and possesses high mobility [1]. However, when cholesterol is incorporated into lipid membranes, it alters lipid ordering properties and induces phase separation in the fluid phase. This leads to the coexistence of liquid-ordered (ℓ_o) and liquid-disordered (ℓ_d) phases in cholesterol-containing lipid membranes [24]. There is a large variety of lipids in cellular membranes and each lipid has its own melting temperature, which results to a rich phase co-existence and presence of nanoscale domains in model and cellular membranes. These nanodomains play important role in the membrane interactions with other biomolecules, including Aβ.

With the progression of age, the neuronal cell membranes undergo significant changes in composition and structure, a phenomenon that has been implicated in various neurodegenerative disorders, including AD [25, 26]. As the brain ages, alterations in lipid composition, such as decreases in polyunsaturated fatty acids and increases in cholesterol, have been noted [27]. Such shifts directly impact membrane fluidity and permeability, potentially impairing various cellular functions. Moreover, age-related oxidative stress can lead to lipid peroxidation [28], generating reactive lipid species that can further destabilize membranes and promote neurotoxicity [29]. These changes in the aged neuronal cell membranes can alter their interactions with proteins such as Aβ, which is critical to AD pathogenesis [2].

Another result from the lipid composition change is the alteration of the lipid membrane physical structure, particularly the existence and dynamics of microdomains known as lipid rafts, may influence Aβ toxicity [2, 30, 31]. These rafts, enriched in cholesterol and

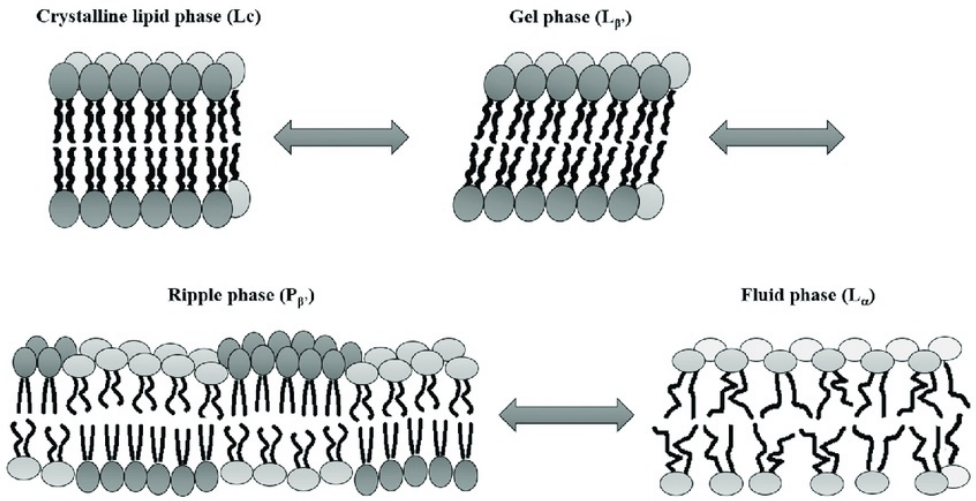


Figure 1.1: **Phase Transition of Lipid Membrane**. In the solid crystalline phase (L_c), lipids are tightly ordered and closely packed. The orientation of lipid hydrocarbon chains can vary, leading to a gel phase ($L_{\beta'}$). The transition from gel to fluid phase (L_α) occurs at phase transition temperature, also known as the melting point (T_m). Before this transition, there is often a pre-transition phase featuring a ripple phase ($P_{\beta'}$) with one-dimensional ripples. In the fluid phase, lipids become highly disordered, losing their lattice order, and exhibit increased lateral and rotational diffusion [1].

sphingolipids, provide a favorable environment for the clustering of APP and secretases, thereby promoting Aβ production [32]. They also serve as platforms for the accumulation of Aβ, which may enhance its local toxicity [33]. Furthermore, defects within the membrane induced by initial Aβ-membrane interaction, might modulate the distribution and aggregation of Aβ, eventually leading to enhanced toxicity [19].

Therefore, since the membrane serves as the primary target for amyloid-membrane interactions, there is a significant opportunity to membrane composition properties to affect amyloid toxicity. When research focuses on the molecular details on the amyloid-membrane interaction, model systems are widely used such that the effects from other cellular membrane components in live cells or membrane extracts could be maximally eliminated. These model lipid membrane systems can range from monocomponent to pentacomponent, increasing in complexity and heterogeneity with each added component [2, 31, 34, 35, 36]. Alvarez *et al.* [34] has shown that the unstaturated lipid (POPC) triggers Aβ aggregation using monocomponent lipid system, while Korshavn *et al.* [35] has shown that the saturated lipid (DLPC) inhibits the Aβ fibrillation. While simpler lipid model systems allow research to more easily focus on one or two lipid species, more complex multicomponent lipid membranes offer a more suitable platform to study phenomena such as lipid phase separation and to mimic domain structures, because the difference in lipid head group sizes and tail lengths bring rise to surface topography diversity on the membranes. The differing attributes of the lipid molecules within these multicomponent systems, such as their head group size, acyl chain length, and degree of saturation, give rise to diverse structures and behaviours that can be tailored to simulate the varying conditions in neuronal cell membranes [37]. These models allow researchers to investigate the interaction of Aβ peptides with cell membranes, which is considered a key factor in AD pathogenesis [38]. Azouz *et al.* [31] have demonstrated that the Aβ preferably aggregates on lipid domains in tertiary membrane systems composed with DPPC/DOPC/cholesterol and SM/DOPC/cholesterol. They also showed that the presence of GM1 and cholesterol in POPC membranes favors the binding of Aβ. Drolle *et al.* [2] have shown that a variation in lipid ratio alters the aggregation of Aβ on lipid model composed with DPPC, POPC, cholesterol, SM and GM1 that mimics different diseased states. Moreover, the lipid membrane models are highly compatible with a range of advanced biophysical techniques, such as AFM [2, 31, 36, 39],

NMR [40, 41], neutron reflectometry and neutron scattering [41, 42], and other nanotechnological tools.

In my thesis research, I used the neuronal cell membrane models developed by Drolle *et al.* in 2017 and its simplified form composed with DPPC, POPC and cholesterol, to form lipid membranes. The compositions of these model systems that mimic the healthy or diseased lipid membranes are listed in Table. A.1. These lipid membranes have distinct surface structures and electrostatic properties, as shown in Figure 1.2, which lead to their different interactions with Aβ. Figure 1.3 illustrates different Aβ accumulations on the three model membranes at 1 hour and 6 hours of incubation time. From this perspective, the structural differences in the membranes were shown to be related to the Aβ interaction. Therefore, it is reasonable to propose that altering the structure of the membrane could potentially affect the nature of the Aβ-membrane interaction, resulting in changes to Aβ toxicity. Melatonin, which will be introduced in the following session, possesses the ability to alter membrane structure. This property makes it an interesting molecule for investigating its potential to modify amyloid toxicity. Therefore, I used melatonin throughout my thesis research.

	Lipid Composition in weight ratio (molar ratio)				
Lipid Models	DPPC	POPC	Cholesterol	SM	GM1
Healthy Model (HM)	37 (35.3)	37 (34.1)	10 (18.1)	10 (9.8)	6 (2.7)
Early Diseased Model (EDM)	39 (36.5)	39 (35.2)	10 (17.8)	10 (9.7)	2 (0.9)
Late Diseased Model (LDM)	42 (39.4)	42 (38.0)	10 (17.8)	4 (3.9)	2 (0.9)
Simple Model (SPM)	41.9 (37.5)	43.4 (37.5)	14.7 (25)	0	0

Table 1.1: **Lipid Compositions of the Three Complex Lipid Models and the Simple Model** mimicking different disease states of neuronal cell membranes in AD: healthy model (HM), early diseased model (EDM), and late diseased model (LDM). The ratios are shown in weight. Adapted from Drolle *et al.* 2017 [2]. The simple model removed SM and GM1 from the neuronal models.

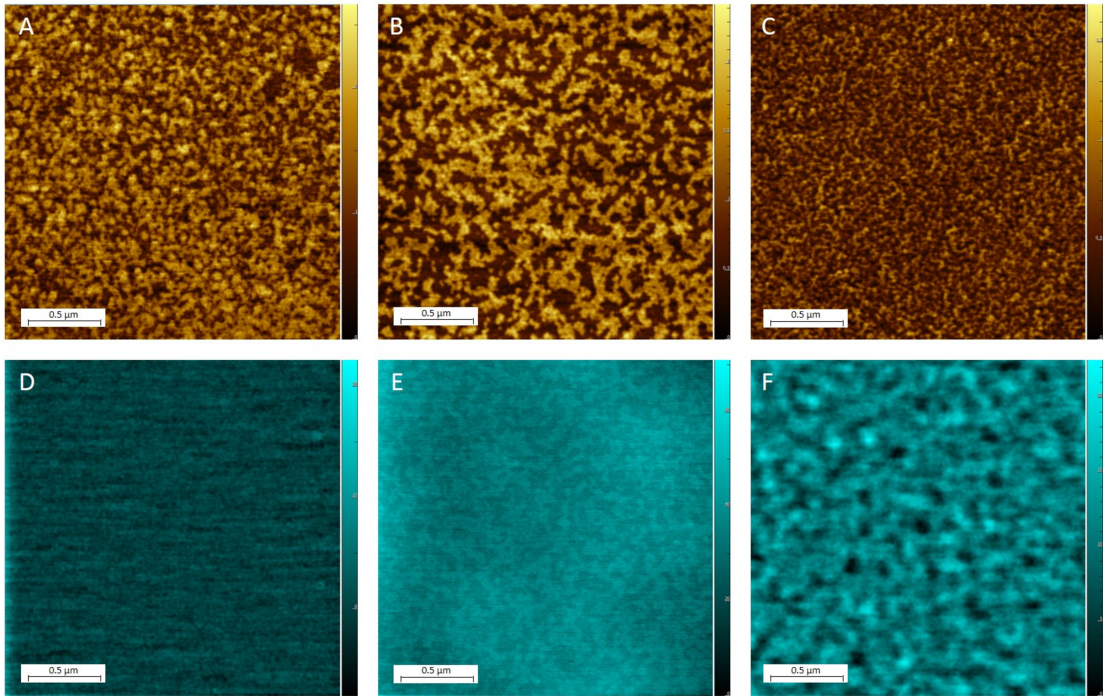


Figure 1.2: **Comparison of monolayer structure and electrical characteristics across three different models**. AFM topography images (gold) and KPFM electrical surface potential images (blue) are shown for the three model systems: healthy (A/D), early diseased model (B/E), and late diseased model (C/F). Figure is cited from Drolle *et al.* 2017 [2].

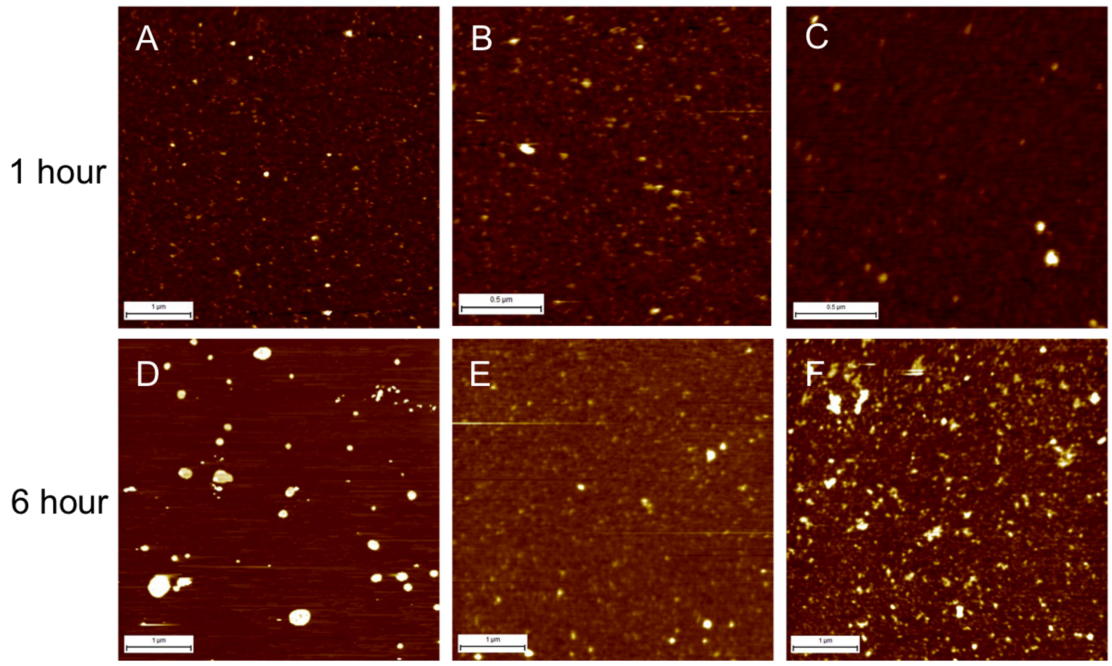


Figure 1.3: **Comparison of Aβ incubation on the three model membranes for 1 and 6 hours**. AFM images in liquid show different Aβ accumulation between 1 and 6 hours of incubation time on healthy (A/D), early diseased model (B/E), and late diseased model (C/F). Figure is cited from Drolle *et al.* 2017 [2].

1.3 Melatonin

Over the years, considerable efforts have been directed towards studying the symptoms of AD or Aβ accumulation with the aim of finding cures for AD. Melatonin, a lipophilic hormone primarily secreted by the pineal gland, plays vital roles in regulating circadian rhythms, seasonality, and antioxidative and immune response effects [7, 43, 44]. There are consistent indications that melatonin can act protectively against Aβ neurotoxicity or AD symptoms, even though the exact molecular pathways remain to be deciphered [45, 46, 47]. Gong *et al.* showed that melatonin improves cognitive function on mice models with cognitive impairment induced by Aβ (1-42) [48]. Clinical trials carried out by Cardinali *et al.* demonstrated that melatonin treatments to patients benefit their cognition significantly [49].

Studies have underscored that general melatonin levels decrease with aging and neurodegeneration, and disruptions in melatonin rhythmicity often appear with these processes [50]. Molecular studies on melatonin's effect on model membranes have further revealed its ability to fluidize the membrane, enhance lipid dynamics, and increase area per lipid. Melatonin was shown to incorporate into and fluidize the lipid monolayer composed with DPPC by Choi *et al.* in 2014 [3]. Research on DPPC or DOPC-containing membrane systems reported by Drolle *et al.* and Kondela *et al.* showed that melatonin reduces the lipid membrane thickness and increases area per lipid [24, 51]. This work from Drolle *et al.* in 2013 also revealed that melatonin preferentially associates with lipid head groups using molecular dynamics simulation, as shown in Figure 1.4 [24]. Moreover, melatonin's demonstrated an ability to alter lipid phase separations in model membranes in Refs. [52, 53] suggests that it may significantly alter the surface properties of the membrane. This alteration could potentially affect non-specific interactions between amyloid and cellular membranes, contributing to the protective effects against amyloid toxicity. Understanding the intricate relationship between melatonin and Aβ-membrane interactions offers an exciting frontier in unraveling the mechanisms of melatonin protection and may open new avenues for therapeutic interventions in AD.

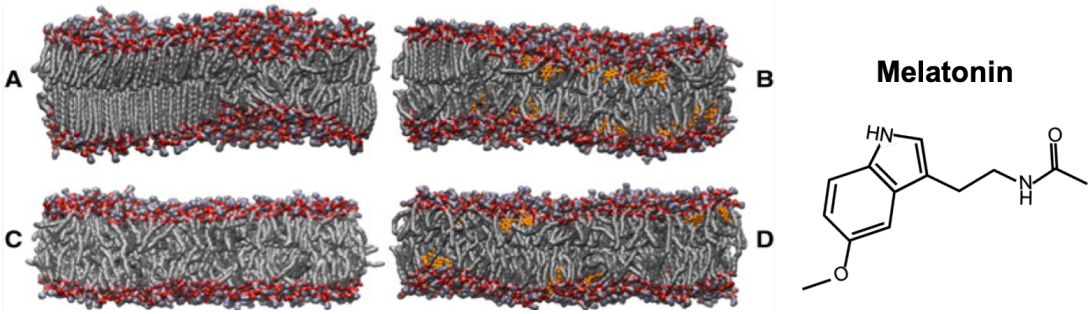


Figure 1.4: **Molecular Dynamics Simulations** of (A) DPPC and (C) DOPC bilayers with and without melatonin. Melatonin molecules are shown in orange, and simulation for the bilayers with melatonin are shown on the right. [1]

1.4 Methods

1.4.1 Nuclear Magnetic Resonance

Nuclear magnetic resonance (NMR) spectroscopy is a powerful analytical technique used to determine the molecular structure, dynamics, and interactions of molecules [54]. It is an essential tool for various disciplines, including chemistry, biology, and physics. By harnessing the magnetic properties of atomic nuclei, particularly those with a non-zero magnetic moment such as ^{1}H (proton) or ^{13}C (carbon-13), NMR offers i nsights i nto the local electronic environment surrounding these nuclei and their positions within a molecule [55]. These nuclei resonate at specific frequencies when subjected to a magnetic fi eld. These frequencies are then detected and provide vital structural details.

The atomic nuclei consists of protons and neutrons bound together by the nuclear force. While electrons orbit the nucleus and determine an atom's chemical properties, it is the nucleus that plays a pivotal role in NMR techniques. One fundamental property of certain atomic nuclei is their spin, which is an intrinsic form of angular momentum. Not all nuclei possess a nuclear spin; only those with either an odd number of protons, an odd number

[1]Reprinted with permission from Elizabeth Drolle *et al.* Effect of melatonin and cholesterol on the structure of DOPC and DPPC membranes. *Biochimica et Biophysica Acta (BBA) - Biomembranes*, 1828(9):2247–2254, 2013. Copyright 2013 by Elsevier.

of neutrons, or both have non-zero nuclear spin [56]. This nuclear spin gives rise to a magnetic moment, making these nuclei responsive to magnetic fields.

The magnetic moment ($\vec{\mu}$) of a nucleus is directly proportional to its spin $\hat{I}$:

$$\vec{\mu} = \gamma \hat{I} \tag{1.1}$$

Here, γ is the gyromagnetic ratio, which is specific to each type of nucleus. For instance, the proton (^{1}H) has a particularly high gyromagnetic ratio, making it one of the most commonly studied nuclei in NMR [57]. Isotopes such as ^{1}H (proton), ^{13}C (carbon-13), and ^{2}H (deuterium) have non-zero magnetic moments and are thus NMR active. While ^{1}H is abundant and gives strong NMR signals, ^{13}C is less abundant in nature but provides crucial structural information when employed in NMR experiments. Deuterium (^{2}H), being a heavy isotope of hydrogen, has its own unique applications in NMR, especially in studies requiring isotopic labeling or in solvent suppression techniques and is widely applied in lipid membrane research [40, 58, 59].

When atomic nuclei with non-zero magnetic moments are placed in an external magnetic field, they tend to align with the direction of this field. Figure 1.5 shows the energy states of the hydrogen nucleus ($I = 1/2$) and the deuterium nucleus ($I = 1$). The magnetic moment associated with the nuclear spin interacts with the external magnetic field, resulting in two main energy states: one where the moment is aligned parallel with the field (lower energy state) and another where it is aligned anti-parallel (higher energy state) [56].

The difference in energy between these two states is directly proportional to the strength of the external magnetic field and is given by the equation:

$$\Delta E = \gamma \hbar B_0 \tag{1.2}$$

Where ΔE is the energy difference, γ is the gyromagnetic ratio of the nucleus, $\hbar$ is the reduced Planck's constant and B_0 is the strength of the external magnetic field [60]. As the external magnetic field strength increases, the energy difference between these states also increases.

The total magnetic moment due to all the spins in a sample gives rise to the net magnetization. In the absence of the external magnetic field B_0, these magnetic moments

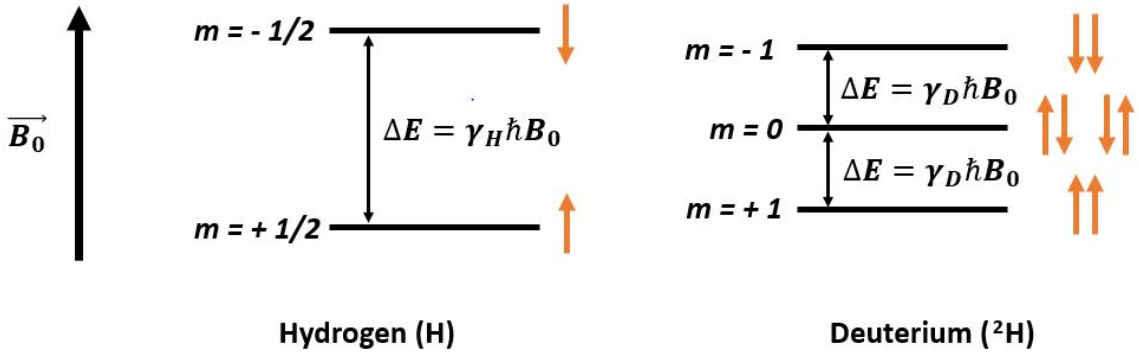


Figure 1.5: **Energy Levels for Hydrogen and Deuterium Nucleus** when place in an external magnetic field $\vec{B_0}$. The gyromagnetic value of hydrogen nucleus is larger than that of deuterium.

are randomly oriented, resulting in a net magnetization of zero. But when a strong external magnetic field is applied, they tend to align with the field, giving rise to a net macroscopic magnetization along the direction of the magnetic field [57].

Nuclear spins in an external magnetic field can be thought of as tiny bar magnets with a tendency to align along the field direction. However, with the application of a perpendicular radio frequency (RF) pulse, these spins can be disturbed from their equilibrium positions. The RF radiation's frequency should match the energy difference between the two spin states (parallel and anti-parallel) for effective perturbation, a condition known as the resonance condition [57, 61].

$$v = \gamma B_0 \tag{1.3}$$

where v is the resonance frequency. When this resonance condition is met, nuclei absorb the RF energy, causing their spins to flip from the lower energy state to the higher energy state. Once the RF pulse is turned off, these perturbed spins tend to return to their equilibrium states, producing an NMR signal in the process [61].

After the RF pulse is switched off, the nuclear spins do not immediately return to their equilibrium positions. The process through which they regain their equilibrium is termed relaxation, and it can be understood through two primary mechanisms: T1 Relaxation

(Spin-Lattice Relaxation) and T2 Relaxation (Spin-Spin Relaxation) [57, 62]. T1 relaxation refers to the interaction of spins with their surrounding molecular environment or lattice. During T1 relaxation, the spins release energy to the lattice until the net magnetization of the sample returns to their initial alignment with the applied external magnetic field. Unlike T1 relaxation, T2 relaxation does not involve an exchange of energy with the lattice. Instead, it describes the loss of coherence among spins due to their interactions with neighboring spins. This process results in the dephasing of spins. The associated T2 relaxation time provides a measure of how swiftly the in-phase transverse magnetization diminishes, and this decay often transpires more rapidly than T1 relaxation.

Apart from these two primary relaxation mechanisms, quadrupolar splitting is another parameter that provides information about the structure and orientation of the molecules in a system. Nuclei with a spin quantum number I greater than 1/2 possess a non-spherical charge distribution, leading to a property called quadrupole moment. When such a nucleus is positioned in an environment with an asymmetric electronic cloud, a local electric field gradient (EFG) exists at the location of the nucleus. Quadrupolar splitting arises from the interaction between this quadrupole moment and the EFG. This interaction can perturb the energy levels of the nuclear spins, leading to distinct splittings in the NMR spectra. The exact nature and magnitude of this splitting depend on several factors, including the magnitude of the quadrupole moment, the strength and orientation of the EFG, and the molecular dynamics. For instance, in solid-state environments where molecular motion is restricted, the full effect of the quadrupolar interaction becomes evident, resulting in pronounced splittings. However, in liquid-state environment where molecules rapidly tumble, these interactions often average out, diminishing the observable effects. The intricate patterns of quadrupolar splitting can be harnessed to gain insights into the local structural environment, molecular orientations, and dynamics surrounding the nucleus. In systems like lipid membranes, where ^{2}H NMR is employed, understanding quadrupolar interactions becomes pivotal to decipher lipid phase behaviour, orientation, and interactions at the atomic level [40, 57]. For this reason, I conducted a study using the ^{2}H NMR to explore the lipid phase behaviours of a simple membrane model under the effect of melatonin. The detailed explanation on quadrupolar splitting and its analysis are provided in Chapter 2.

1.4.2 Surface Plasmon Resonance Techniques

Localized surface plasmon resonance (LSPR) sensing capitalizes on the unique properties of surface plasmons in a nanoparticle (NP) to detect changes in the local refractive index, particularly in biochemical applications. Through the excitation of localized surface plasmons and precise monitoring of resonance shifts, LSPR sensors offer highly sensitive and selective detection in real time. LSPR occurs when the conductive electrons cloud in metallic NPs oscillate in response to an incident electromagnetic wave. These oscillations can be highly confined to the NP surface, leading to a significant enhancement of the electric field near the particles [63]. The principle of LSPR inherits from SPR and I am going to introduce the basic physcis theory behind SPR first.

Total internal reflection (TIR) is a fundamental optical phenomenon that underpins the operational principle of SPR sensors. It occurs when light travels from a medium with a higher refractive index, n_1, to a medium with a lower refractive index, n_2, at an angle greater than the critical angle, θ_c. The critical angle can be determined using Snell's law:

$$\theta_c = sin^{-1}(\frac{n_2}{n_1}) \tag{1.4}$$

Without the entirety of the energy being reflected, a small portion of the light's energy, in the form of an evanescent wave, penetrates a short distance into the less dense medium. The intensity of this wave decays exponentially as it moves away from the interface. This evanescent wave plays a crucial role in SPR as it can excite propagating plasmons, which are referred to as surface plasmon polaritons (SPP), at the metal-dielectric interface when conditions are right [64]. The exact depth to which the evanescent wave penetrates depends on factors such as the wavelength of the incident light and the angle of incidence, but is typically on the order of a few hundred nanometers [64].

SPPs are collective oscillations of conduction electrons that are localized at the interface between a metal and a dielectric. The nature of SPPs arises due to the interaction between the electric field from light and the free electrons in a metal. This interaction confines the electromagnetic field at the interface, leading to a unique evanescent wave. The phenomenon of SPPs can be better understood through its dispersion relationship, wave vector, and resonance condition. Let us write the wave vector of the incident light as

$\vec{k} = (k_x, k_y)$, then the following equation provides the resonance condition of the surface plasmon.

$$k_{SP} = \frac{\omega}{c}\sqrt{\frac{\epsilon_m * \epsilon_d}{\epsilon_m + \epsilon_d}} = k_x \tag{1.5}$$

where ω is the angular frequency of the incident light, ϵ_m is the dielectric constant of the metal, ϵ_d is the dielectric constant of the dielectric. At the resonance condition of SPs, the SP wave vector $\vec{k}_{SP}$ equals to the wave vector of the incident light along the x-direction, $\vec{k}_x$; in other words, surface plasmon resonance SPR occurs when the incident light's frequency matches the natural frequency of the surface plasmon oscillations. In an SPR instrument, light composed of a spectrum with broadband wavelengths incidents on the metal/water interface, as shown in Figure 1.6. The light with matched wave vector (can be converted into wavelength by $k = 2\pi/\lambda$) to the SPP is absorbed and its intensity is low on the reflection band, appearing as a dark band. When molecules bind to the metal/water interface from the water side, the average ϵ_d in the vicinity of the interface would shift, leading to a change in k_{SP}. Therefore, the wave vector for the incident light that matches the resonance condition is changed and a new absorbance band is observed. By measuring the absorbance of reflected light, one can detect the binding of molecules to the sensor site [65].

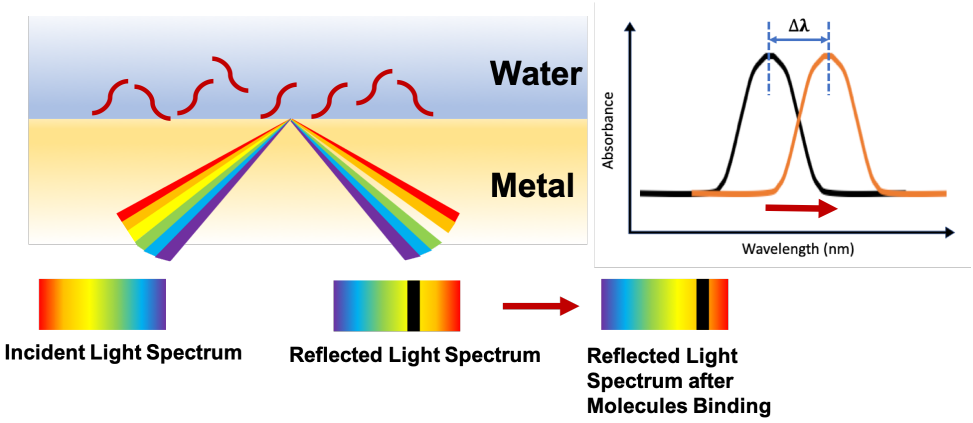


Figure 1.6: **Schematic of SPR Working Principle**. Incident polychromatic light is reflected on the metal/water interface, with partial energy transferred to SPP. The light with the wavelength matched the resonance condition is absorbed by the SPP and therefore appears as a dark band in the reflected spectrum. When molecules bind to the interface, the absorbed wavelength shifts. The measurement on $\Delta\lambda$ indicates the binding activity happens on the interface.

LSPR utilizes metal NP, typically sized between 10-200 nanometers, as opposed to the flat metal films used in conventional SPR. This modification in the sensing setup leads to an amplification of the incident light energy by 100-10,000 times, restricting the sensing area to a proximity of 10-50 nanometers around the nanoparticles [66]. NPs exhibit optical properties distinct from bulk materials. Metallic NPs lead to a distinct electron bands and size-dependent plasmon resonance influenced by NP surface distribution. In contrast to the propagating SPPs in SPR, the LSPR plasmon wave is localized. As shown in Figure. 1.7, when a small NP is exposed to a plane wave, the fluctuating electric field triggers synchronized movement of electrons in the conduction band, resulting in the buildup of polarization charges on the NP surface [67]. Details on the experimental measurement of LSPR signals and equations describing the approach to extract molecule binding results are discussed in Chapter 3.

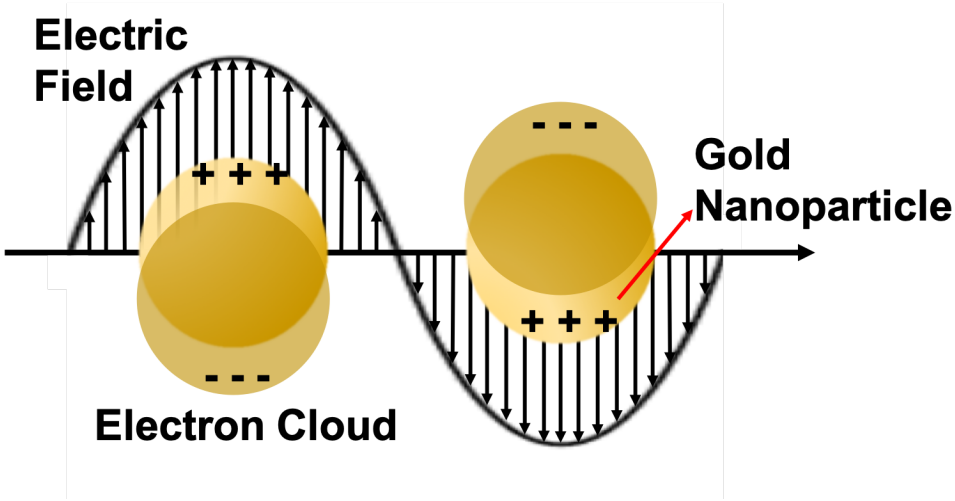


Figure 1.7: **Schematic Diagram of LSPR.** Electron cloud of the gold nanoparticles oscillates with a static electric field, generating localized surface plasmon.

1.4.3 Atomic Force Microscopy

Atomic force microscopy (AFM) is a type of scanning probe microscopy that allows for high-resolution imaging of surfaces at the nanoscale. Introduced by Binnig, Quate, and Gerber in 1986 [68], this technique operates by scanning a sharp probe, typically a cantilever with a fine tip, over the sample surface. As illustrated in Figure. 1.8, the deflection of the cantilever is measured as it interacts with surface features, enabling the creation of topographical images with atomic resolution. AFM can be applied under various conditions, including ambient air, vacuum, and even liquids, making it versatile for different types of samples, from hard inorganic materials to soft biological specimens.

The key theory of AFM imaging is the application of Hooke's Law, represented as $F = -kx$. F stands for the spring force, k denotes the spring constant, and x is the displacement of the spring from its equilibrium position. In AFM, the cantilever functions as a spring. Figure. 1.9, shows a potential curve of the cantilever-tip interaction. When the cantilever tip nears the sample surface, attractive forces dominate the cantilever-sample interaction, primarily cause the cantilever to bend towards the sample. However, as the tip gets closer, repulsive forces gradually take over, making the cantilever deflect away from

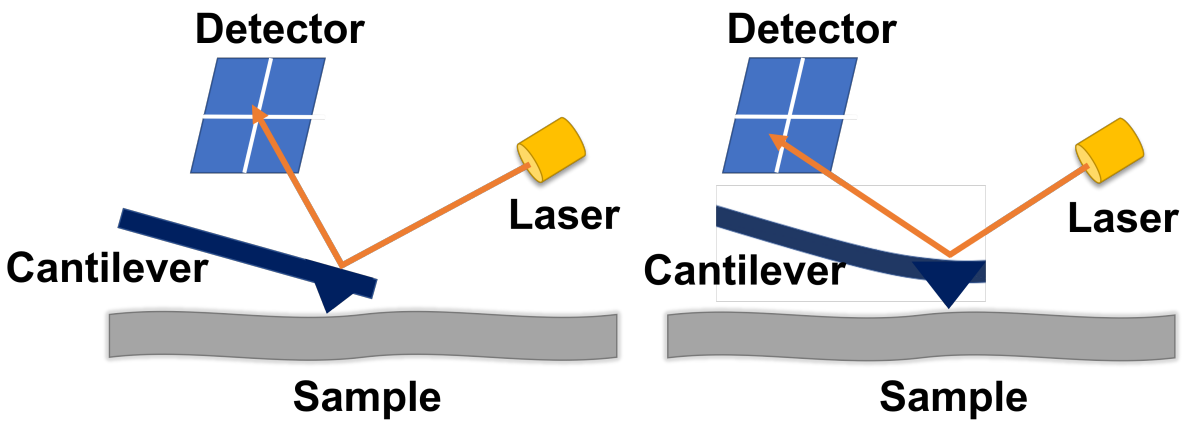


Figure 1.8: **AFM Imaging Schematic.** A laser shines on the back of the cantilever and its reflection shines on a detector. The deflection of the cantilever results in a shift on the reflected spot on the detector.

the surface. It is this deflection that gives insights into the sample's surface features.

Scanning in AFM primarily has three modes: contact mode, intermittent contact mode and noncontact mode [69, 70, 71]. Schematic of these imaging modes are included in Figure. 1.9. The contact mode is in the repulsive region of the potential curve. It involves the cantilever tip mechanically contacting the sample. While scanning the surface, a feedback system keeps the cantilever's deflection constant, generating images based on voltage adjustments to the piezoelectric actuator. However, this mode can cause damage due to strong lateral forces and lacks a consistent zero-force reference. The intermittent contact mode cover the repulsive and the attractive region of the potential curve. It is widely used in ambient air and liquid settings. The cantilever oscillates near its free resonance frequency. As the sample approaches the surface, the cantilever's amplitude decreases to a set value. The feedback mechanism maintains this oscillation amplitude while scanning the surface. Unlike the contact mode AFM, which uses the static deflection of the cantilever as its feedback signal, the intermittent contact mode AFM utilizes the oscillation amplitude. Noncontact AFM utilizes weak attractive forces, differing from contact mode techniques. The method involves small oscillations of the cantilever tip, detecting small forces. Nonetheless, it is widely used for various materials, offering advantages like minimal

sample contact, making it suitable for soft samples.

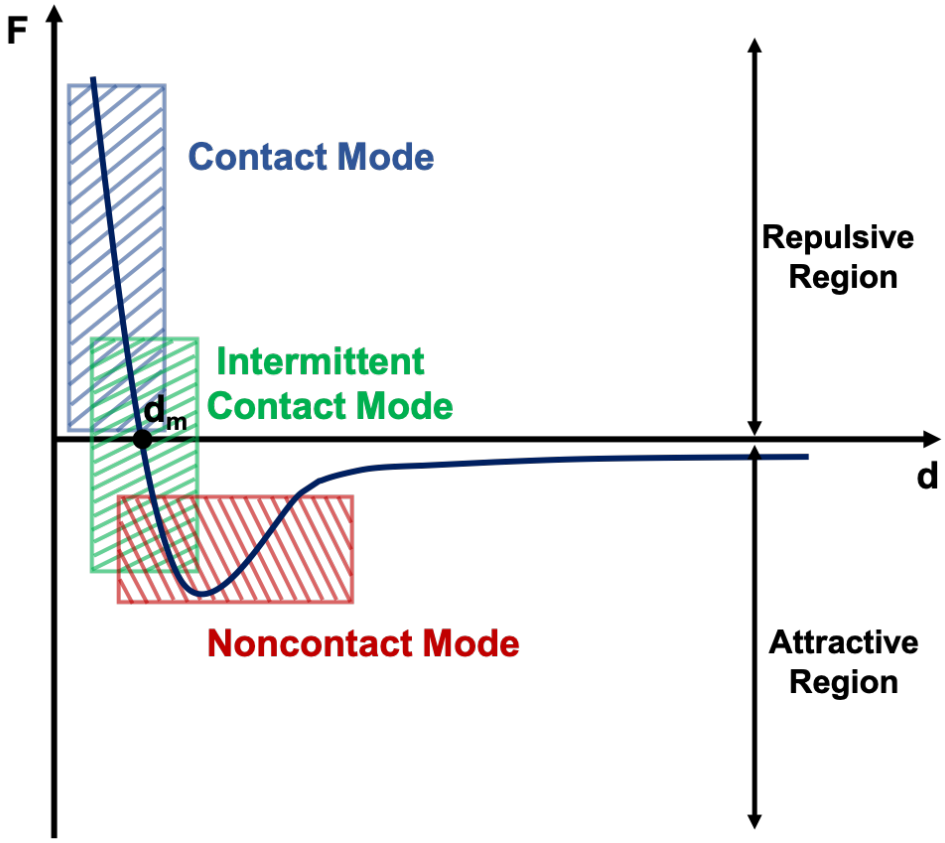


Figure 1.9: **Force Curve and Imaging Modes of AFM**. In the attractive region, the net force between the cantilever tip and the sample surface increases as the attractive force increases. In the repulsive region, the net force increases with the increasing repulsive force. A minimum potential point occurs at a distance of d_m, where the attractive and repulsive forces balance each other. Contact mode takes place in the repulsive region, intermittent contact mode covers both repulsive and attractive regions, and noncontact mode occurs in the attractive region.

AFM is widely applied in biology field in imaging of cellular morphologies and dynamics relevant to diseases, as well as the structure of proteins or peptides and their interactions with cell membranes. For instance, Alsteens *et al.* delved into the nano-level analysis of a hormone receptor on fixed human bladder cancer cells [72]. Additionally, the Leonenko group explored the self-aggregation of amyloids and their interactions with model cellular membranes, shedding light on AD [36, 73]. In this thesis, AFM was employed to visualize lipid membranes and the damages caused by amyloids, providing insights for the LSPR study. Chapter 3 provides an in-depth look at the experimental setup and data analysis methodologies.

1.4.4 Black Lipid Membrane

The black lipid membrane (BLM) technique offers a versatile platform for studying the functional properties of membrane channels and the interactions of various agents with lipid bilayer membranes. This self-assembled membrane closely mimics the properties of natural cell membranes, making it invaluable for physiological and biophysical studies. First introduced in the early 1960s by Mueller and Rudin, the BLM technique involves the formation of a lipid membrane across a small aperture in a partition that separates two aqueous compartments [74]. Figure 1.10 shows a schematic of the BLM instrument configuration. A membrane forms on the middle of the Teflon divider, splitting the buffer bath into two sections. A voltage bias is introduced on the opposing side of the barrier. A near-zero current is observed when the membrane is intact; however, if there are holes or channels in the membrane, a detectable current can be recorded. Using the BLM setup, one can monitor and measure ionic currents, which provides insights into channel functions, ion transport processes, and the effects of drugs or toxins on membranes.

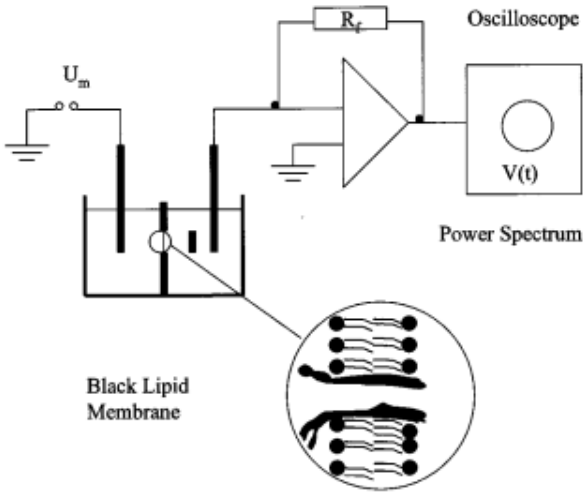


Figure 1.10: **Schematic of BLM.** Two electrodes are placed in the buffer on the opposite sides of the middle barrier, and an electric bias is applied. A lipid membrane is spread over the aperture and covers it entirely. Ion current occurs when there are holes or discontinuities in the membrane, and this can be recorded in the circuit. [2]

The BLM technique is applied in studying lipid membrane function and its interaction with membrane proteins or peptide, therefore research can focus on the lipid membrane composition [75] and protein or peptide types [18], or to study the mechanisms of protein-membrane interaction [76]. As well it can serve as the media for holding membrane ion channels and contribute to characterizing the ion channels [77, 78]. In Chapter 4 of this thesis, I employed the BLM approach to explore the amyloid-membrane interaction. I investigated various membrane damages resulting from this interaction. By introducing melatonin into the system to modify the membrane composition, I aimed to study its effect on the amyloid-membrane interaction. Comprehensive details regarding the methodology and data analysis are discussed in the Method section of Chapter 4.

[2]Reprinted with permission from Mathias Winterhalter. Black lipid membranes. *Current Opinion in Colloid & Interface Science*, 5(3-4):250–255, 2000. Copyright 2000 by Elsevier.

Chapter 2

Nuclear Magnetic Resonance to Study Melatonin Effect on Lipid Phase Behaviour of DPPC/POPC/Cholesterol Lipid Membranes

2.1 Overview

2.1.1 Summary of Published Work

This chapter is reproduced from the work published in Biophysical Journal:
Nanqin Mei, Morgan Robinson, James H Davis, and Zoya Leonenko. Melatonin alters fluid phase coexistence in POPC/DPPC/cholesterol membranes. *Biophysical Journal*, 119(12):2391–2402, 2020.

In this ^{2}H-NMR study, I explored melatonin's effect on the DPPC/POPC/cholesterol lipid membrane phase separation. We discovered that melatonin promotes $\ell_d : \ell_o$ phase

coexistence in the DPPC/POPC/cholesterol mixed membranes, with a preferential interaction with the unsaturated POPC lipids. Concurrently, melatonin appears to displace cholesterol in disordered phases, enhancing disorder and redirecting cholesterol towards the DPPC's ordered phase. Moreover, due to perdeuteration of lipids, melting temperature differences between POPC-d_{31} and DPPC increase, while differences between DPPC-d_{62} and POPC decrease. In this model, melatonin boosts membrane fluid phase diversity, shedding light on its potential protective role at the membrane level.

2.1.2 Contributions

Under the supervision of Prof. Zoya Leonenko, I designed the work and the experimental plan for this study, and I was also responsible for sample preparation. Dr. Morgan Robinson contributed by providing insights into melatonin properties, assisting in determining the optimal melatonin concentration for our experimental groups, and helping with initial sample preparation and Introduction writing for the paper (Dr. Robinson prepared Figure 2.1). I reached out to Prof. James H. Davis from the University of Guelph (UofG) for his expertise in NMR work related to lipid membrane models, as well as access to the NMR facility at UofG. Prof. Davis provided training on the solid-state NMR instrument, managed the data collection for this set of experiments, and collaborated with me on data analysis. Together, we co-authored the Method section in the manuscript.

2.1.3 Challenge and Future Directions

In this study, I used a simple neuronal membrane model composed of ??, ?? and cholesterol because its structure is easier to predict and understand. However, there is a lot of potential for future research in this area. Researchers could look into more detailed and intricate models, such as the 5-component models of neuronal cell membranes I mention in other parts of this thesis. Other avenues to explore would be to add amyloid to the lipid membrane and see how is changes in amyloid structure, as well as the lipid odering parameters. It would be particularly interesting to observe how these amyloid structures might change based on different combinations of lipids and varying levels of melatonin.

This could provide deeper insights into the broader impacts on cell health and function in relation to AD.

2.2 Abstract

The structure and biophysical properties of lipid membranes are important for cellular functions in health and disease. In Alzheimer's disease (AD) the neuronal membrane is a target for toxic amyloid-β (Aβ). Melatonin is an important pineal gland hormone that has been shown to protect against Aβ toxicity in cellular and animal studies, but the molecular mechanism of this protection is not fully understood. Melatonin is a small membrane active molecule, which has been shown to interact with model lipid membranes and alter the membrane biophysical properties, such as membrane molecular order and dynamics. This effect of melatonin has been previously studied in simple model bilayers with one or two lipid components, to make it more relavant to neuronal membranes we used a more complex ternary lipid mixture as our membrane model. In this study, we used ^{2}H-NMR to investigate the effect of melatonin on the phase behaviour of DPPC, POPC and cholesterol lipid membranes. We used deuterium labelled POPC-d_{31} and DPPC-d_{62}, separately, to probe the changes in hydrocarbon chain order as a function of temperature and melatonin concentration. We find that DPPC/POPC/cholesterol at molar proportions of 3:3:2 is close to ℓ_d/ℓ_o phase separation and that melatonin can induce phase separation in these ternary mixtures by preferentially incorporating into the disordered phase and increasing its level of disorder. At 5 mol% melatonin, we observed phase separation in samples with POPC-d_{31}, but not with DPPC-d_{62}, while at 10 mol% melatonin phase separation was observed in both samples with either POPC-d_{31} or DPPC-d_{62}. These results indicate that melatonin can have a strong effect on membrane structure and physical properties, which may provide some clues to understanding how melatonin protects against Aβ, and that choice of chain perdeuteration is an important consideration from a technical point of view.

2.3 Introduction

Cellular membranes are complex structures composed of phospholipid bilayers and multiple membrane proteins. In natural membranes, lipids and protein are unevenly distributed producing a heterogeneous structure of lateral domains. These membrane domains (caveolae-enriched and lipid rafts) have been proposed to compartmentalize different cellular processes [23, 79]. Model lipid membranes composed of synthetic lipids are widely used to mimic the plasma membrane and study membrane properties [2, 24, 80]. One such property is the phase behavior of lipid membranes which can undergo transitions depending on their composition, temperature, pressure and other thermodynamic properties. Phase separation can occur where two or more domains co-exist due to an immiscibility of the constituent components. These properties have been studied by a variety of biophysical techniques including nuclear magnetic resonance (NMR) [80], scattering [81] and fluorescence techniques [82, 80] and atomic force microscopy (AFM) [83]. The coexistence of liquid-ordered (ℓ_o) and liquid-disordered (ℓ_d) phases has been extensively observed in model lipid systems [80, 82, 84, 85] and there is some evidence of nanodomains in living systems [86]. In general, domains rich in cholesterol and saturated lipids have a higher degree of molecular order compared to the whole membrane system [80] and correspond to the membrane domains in natural cell membranes. Because membrane domains facilitate important cellular processes, changes to phase behavior and membrane structure that occur in cells can have important implications for homeostasis and thus for disease pathogenesis [87, 88].

The maintenance of membrane properties and structure is important for proper function and damage caused by free radicals and toxins, and proteins needs to be prevented, mitigated, and/or repaired. In Alzheimer's disease (AD), the accumulation of amyloid-β (Aβ) on the plasma membrane leads to membrane perforation, disruption of membrane domains and potential, oxidative stress and lipid peroxidation as well as a whole host of other pathological changes that ultimately lead to cell death [89, 90, 91, 92]. Membrane damage and toxicity caused by Aβ is lipid composition dependent [2, 93]. Small molecules, for instance vitamin E, can associate with and protect lipid bilayers from damage or otherwise aid in maintaining optimal structure which are important in maintaining cellular home-

ostasis [94]. Melatonin is a tryptophan-derived pineal gland hormone that is important for regulating circadian rhythm and in animal and cell studies has demonstrated potent antioxidant properties and neuroprotective activity against Aβ toxicity [95, 96, 97, 98, 99]. Interestingly, the protective effect of melatonin was found to be receptor independent [100], yet the complete molecular mechanisms are not well-understood, for this reason the effects of melatonin on the membrane may be of specific importance.

Melatonin is a potent antioxidant that has been shown to prevent lipid peroxidation and the subsequent increase in membrane rigidity caused by peroxidation [101]. In addition, melatonin has also been shown to directly affect membrane properties having fluidizing effects on phosphatidylcholine monolayers and liposomes [3, 102, 103], reducing membrane thickness of phosphatidylcholine bilayers [24, 104] and causing an increase in membrane disorder in these systems. Molecular dynamics simulations predict that melatonin sits near the interfacial headgroup region, oriented in the plane of the bilayer membrane in contrast to cholesterol which orients perpendicular to the membrane plane (shown in Figure 2.1). More recently, small angle neutron scattering, and fluorescence microscopy showed that melatonin stabilized ℓ_d:ℓ_o phase transitions in DSPC/DPPC/POPC/cholesterol membranes suggesting it prevented formation of the ℓ_d phase [105]. Previous studies in single component lipid systems may not generalize to more complicated model and natural membranes, and thus more work is needed to fully elucidate the molecular mechanisms of melatonin's effect on more complex lipid membranes, before exploring how it may affect interactions with Aβ.

Solid state ^{2}H NMR has been widely employed to study phase equilibria phenomena in lipid membrane systems [80, 84, 106]. In this work, we use ^{2}H NMR to measure the influence of melatonin on the phase equilibria of tertiary model lipid membranes containing POPC-d_{31}/DPPC/cholesterol and DPPC/POPC-d_{62}/cholesterol. We show that melatonin induces ℓ_d:ℓ_o phase coexistence in both models, however phase coexistence was detected at 50% lower concentration in POPC-d_{31} containing membranes compared to DPPC-d_{62}. These results may be attributed to a stronger interaction of melatonin with the more disordered lipid membrane regions containing higher abundance of POPC (illustrated in Figure 2.1). This may have important implications for the role of melatonin as an antioxidant since a preference for the more disordered lipid domains, which are more susceptible to

peroxidation would expect to contribute to its membrane protective effects. How these results might explain the direct amyloid-membrane interactions are less clear but may involve domain stabilization, prevention of amyloid induced defects or membrane binding affinities. We consider the effects caused by POPC-d_{31} vs DPPC-d_{62} chain perdeuteration which may inform isotopic labelling effects in future lipid membrane studies.

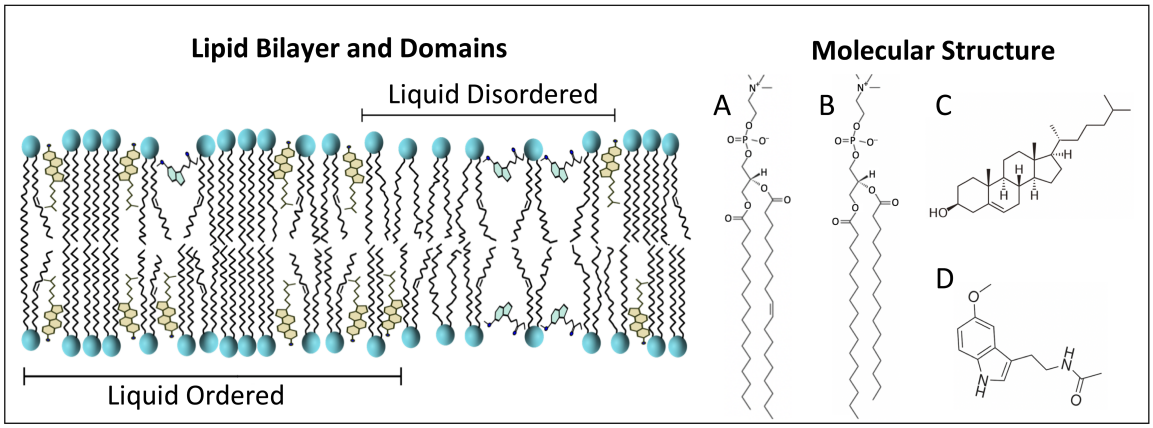


Figure 2.1: **Schematic of the Simple Model System**. Lipid bilayer membrane consisting of POPC, DPPC, cholesterol (*yellow*) and melatonin (*blue*), and their molecular structures showing on the right: (A) POPC, (B) DPPC, (C) cholesterol and (D) melatonin. The coexistance of ℓ_o and ℓ_d phases is represented. Liquid ordered phases have tails that are aligned and more rigid than disordered tails. The orientation of cholesterol and melatonin predicted from MD simulations is shown [3], with melatonin decreasing the lipid ordering and cholesterol having opposing effects.

2.4 Materials and Methods

2.4.1 Sample Preparation

All lipids were purchased from Avanti Polar Lipids, cholesterol and melatonin were purchased from Sigma-Aldrich and their molecular structures are shown in Figure 2.1. These

chemicals were used without further purification. Lipid stock solutions were prepared using chloroform at a concentration of 10 mg/ml and melatonin stock solution was prepared with ethanol at 10 mg/ml. A lipid model system composed of POPC, DPPC and cholesterol at molar proportions of 3:3:2 was used throughout. Two types of deuterium labelled lipid mixtures, POPC-d_{31}/DPPC/cholesterol and DPPC/POPC-d_{62}/cholesterol, were prepared. Melatonin was added to each type of lipid mixture at molar ratios of 0, 5 and 10% to obtain a sequence of samples. Also, pure POPC-d_{31} and pure DPPC-d_{62} samples were tested to determine the effect of perdeuteration to the lipid melting temperature.

To prepare the lipid samples, standard solutions were mixed in a round bottom flask, according to the desired molar proportions while insuring the deuterated lipid in each mixture was at least 5 mg. Because the quadrupolar splittings of ^{2}H NMR are very sensitive to the concentration of cholesterol in the liquid-crystalline phase, a heterogeneous distribution of cholesterol will lead to a broad distribution of splittings [84]. Ethanol has been shown to reduce the heterogeneity of lipid mixtures when compared with chloroform [80, 84]. Thus, after lyophilization from chloroform overnight, ethanol was used to dissolve the lipid mixtures and melatonin stock solution was added and mixed in the meantime. The sample was then freeze-dried overnight from ethanol and scraped out from the bottom of the flask. Each sample was transferred into a snap-cap centrifuge tube and resuspended in 50 mM phosphate buffer (pH 7.0), at weight ratio of lipid to buffer of 4:3. The sample was mixed with a thin glass rod and the whole mixture was centrifuged into the bottom of the tube. This process was repeated 2-3 time to create a uniformly-distributed multilamellar mixture [84]. The whole mixture was transferred into a 3 mm diameter NMR tube by centrifugation through a small hole that was cut on the bottom of the snap-cap tube. The NMR sample tube was sealed with silicone and was given at least 2 hours for the silicone cap to dry out. The entire sample tube was then weighed before and after each use to monitor any possible loss of water during the experiment.

2.4.2 ^{2}H NMR

At the beginning of each series of NMR measurements the sample was heated to an initial set point of 324 K (actual sample temperature of 50.9 °C) in order to assess the sample

homogeneity from the ^{2}H NMR spectrum itself. Spectra were then taken as a function of temperature, cooling the set point in 1 K steps from 324 down to 268 K (50.9 °C to -5.2 °C), except for pure POPC-d_{31}, where the temperature was lowered to 258 K (-15.2 °C). Since the sample temperature is not always exactly equal to the set point temperature, the NMR probe temperature was calibrated using the temperature dependent frequency shift of $Pb(NO_3)_2$ [107, 108]. Figure 2.2 shows the calibration curve. The melting points of DPPC/water and DMPC/water were used as references for the calibration.

The temperatures used in the text of results and discussion, shown on the figures are the corrected sample temperatures. At each cooling step the temperature was allowed to come to equilibrium at the new set point temperature after which the sample was allowed an additional 10 minutes to equilibrate before the spectrum was taken. Each spectrum consisted of the accumulation of 4096 scans obtained using the quadrupolar echo sequence [109]. At the end of each temperature series the samples were then reheated to a set point of 300 K (26.9 °C) and subsequently to 324 K (50.9 °C) where spectra were again taken to verify the reproducibility of the spectra and the stability of the sample. After all NMR experiments were completed on a given sample, the sample was weighed for comparison with the initial weight. In this fashion, we were able to ensure that little water was lost during any of the measurements. It takes at least 18 water molecules per lipid to fully hydrate phosphatidylcholine lipid membrane, the samples used here were prepared with nominally 30-31 waters per lipid (including DPPC, POPC and cholesterol) [110]. Sample weights after experiments were completed indicate, that in the worst case, water loss, of no more than 1 mg total water, left at least 28 waters/lipid.

All NMR experiments were performed on a Bruker Avance II Plus 500 MHz spectrometer operating at a ^{2}H NMR resonance frequency of 76.72 MHz using a transverse coil. The quadrupolar echo sequence consists of two 90^o pulses, each 2.9 μs long, separated by an echo forming delay τ of 25 μs. In order to refocus the precession due to the quadrupolar interaction during τ, the second pulse is phase shifted relative to the first by 90^o [109]. The relaxation delay between scans was 0.5 s.

Because ^{2}H is a spin 1 nucleus, the ^{2}H NMR spectrum is dominated by the quadrupolar interaction between the electric quadrupolar moment of the nucleus, eQ, and the electric field gradient at the nucleus, eq [40]. This interaction results in two peaks to the spectrum of

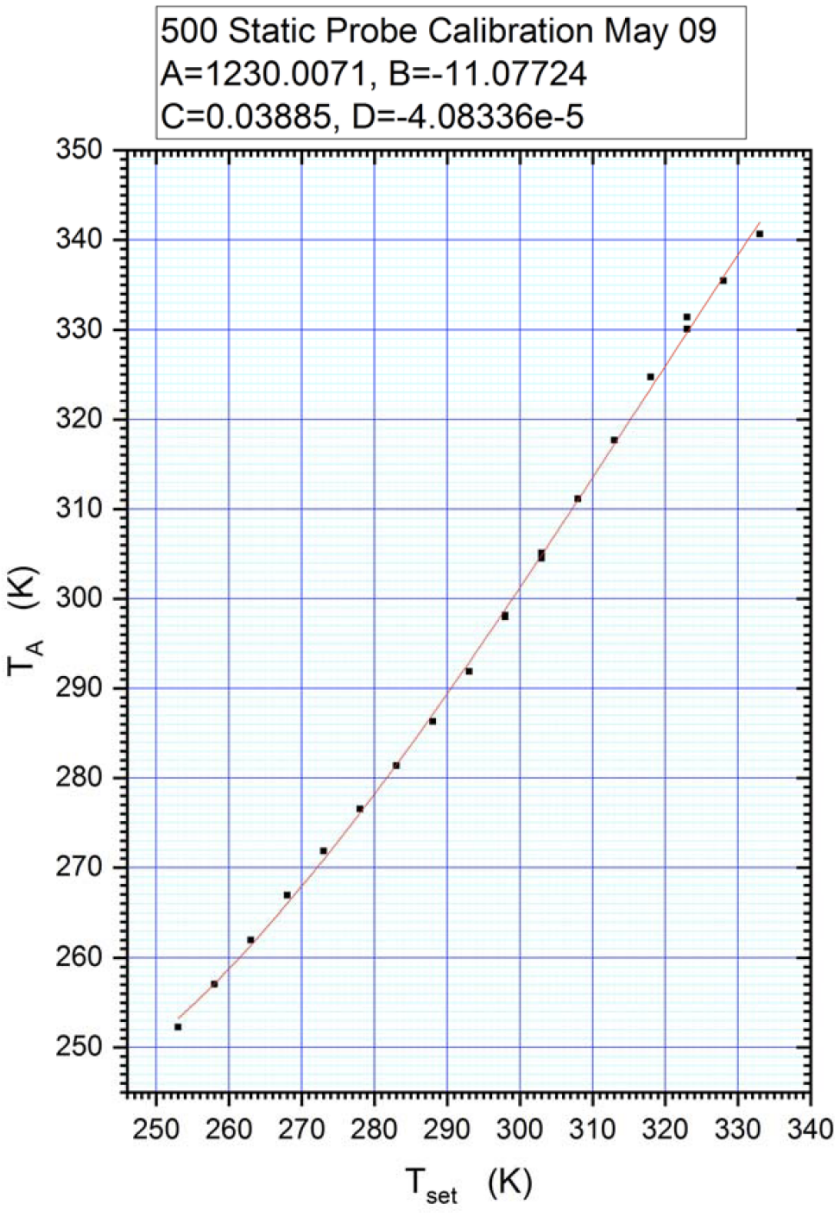


Figure 2.2: **Calibration Curve of Accurate Temperature VS Set Temperature in the NMR Spectrometer**. The function of the fitted curve is expressed as: $T_A = A + B * T_{set} + C * {T_{set}}^2 + D * {T_{set}}^3$.

a single ^{2}H, which are separated by the quadrupolar splitting. The value of the quadrupolar splitting depends on the orientation of the principal axis of the electric field gradient (aligned along the C-^{2}H bond in lipids) and the external magnetic field

$$\Delta\nu_Q = \frac{3}{4}\frac{e^2qQ}{h}[(3\cos^2\beta - 1) + \eta\cos 2\alpha \sin^2\beta] \tag{2.1}$$

Where the angles α and β are Euler angles specifying the orientation of the principal axis system of the electric field gradient tensor relative to the external magnetic field $\mathbf{B_0}$ and h is Planck's constant. This expression is significantly simplified for ^{2}H in C-^{2}H bonds because the asymmetry parameter, η, is very small and can be taken to be 0. The maximum quadrupolar splitting for ^{2}H occurs when there is no molecular reorientation relative to the magnetic field and is found when the C-^{2}H bond is aligned parallel to the field. In that case the observed splitting would be 252 kHz. In fluid lipid bilayers there is a lot of molecular motion so that the quadrupolar splittings observed are greatly reduced. The experimental value of the quadrupolar splitting for a ^{2}H nucleus in a C-^{2}H bond provides a useful measure of the degree of molecular motion experienced by that segment of the molecule. It can range from a value of 0, observed for rapid isotropic molecular reorientation, to the rigid lattice limit of 252 kHz [40].

In fluid phase (ℓ_d or ℓ_o) lipid bilayers and biological membranes under physiological conditions [40, 106], the local bilayer normal is an axis of symmetry for molecular reorientation. Under these conditions, the quadrupolar Hamiltonian is projected onto the axis of symmetry and the quadrupolar splitting is reduced to

$$\Delta\nu_Q = \frac{3}{4}\frac{e^2qQ}{h}[(3\cos^2\beta - 1)]\cdot < 3\cos^2\theta - 1)/2 > \tag{2.2}$$

where θ is now the angle between the C-^{2}H bond and the axis of symmetry for the motion and β is the angle between the motional symmetry axis and the external magnetic field. The angular brackets indicate an average over molecular reorientations which occur on a time scale shorter than the NMR time scale (in the present case the NMR time scale is in the range of 10 μs to 1 ms).

For an oriented sample where the local bilayer normal has a single well-defined orientation relative to the magnetic field one observes a simple quadrupolar doublet for each

C-^{2}H bond with a splitting given by the expression above. For a powder sample, where all orientations of the local bilayer normal are equally likely, a Pake doublet (powder pattern) spectrum is observed and the quadrupolar splitting is defined to be the separation between the two intense peaks corresponding to the 90° orientation of the bilayer normal relative to the magnetic field [106]. Since all of the samples used here are powder samples, the quadrupolar splittings we discuss are for the 90° edges.

Lipid hydrocarbon chain order is much higher for lipids within a ℓ_o phase domain than for lipids in a ℓ_d phase domain. For samples made with deuterium labelled lipids (such as DPPC which is deuterium labelled at a single chain position), at temperatures and compositions that are within a two phase, ℓ_d:ℓ_o, region we would expect to see two very distinct quadrupolar splittings. If the lipid chains are labelled at all positions then, because of the variation of C-^{2}H bond order with chain position [40], there will be a superposition of many quadrupolar splittings in the spectra but those lipids which are in the more ordered ℓ_o phase will have much larger quadrupolar splittings than those lipids which are in the relatively disordered ℓ_d phase [84, 106].

Moment and Quadrupolar Splitting Analysis

The multiple overlapping quadrupolar splittings from the chain methylene groups are frequently difficult to resolve. In order to compare chain order at different temperatures and different sample compositions, we typically calculate the first moment, M_1, of the ^{2}H spectrum since it is proportional to the average quadrupolar splitting [106]. The n'th moment of the symmetric ^{2}H spin 1 powder pattern spectrum is defined by

$$M_n = \frac{1}{A}\int_{-\infty}^{\infty} |\omega|^n f(\omega) d\omega$$

where A is the area of the spectrum, $f(\omega)$ is the spectral lineshape, and the integral is over all frequencies with the origin of the frequency axis at the centre of the spectrum. In practice the area and the moments are calculated by summing over the discrete spectrum (after multiplying by the n'th power of the frequency at each point of the spectrum), starting at some lower limit frequency, -ω_{lim}, and stopping at a symmetrically located upper limit frequency ω_{lim}. The limiting frequency is chosen such that there is no signal

intensity outside of this summation limit. In order to minimize the impact of noise on the moment calculation, the limit is chosen to be close to the outer edges of the experimental spectrum. The uncertainty in the first moment originates from several contributions. The quality of the spectrum is of prime importance in minimizing the uncertainty. By using intense, short 90° pulses and a short inter-pulse delay to form the quadrupolar echo we minimize the distortion of the spectrum [40, 111]. The signal to noise ratio of the spectrum contributes an uncertainty in M_1 of about 1% for the spectra reported here. The baseline irregularities, caused primarily by probe ring-down, introduce a further uncertainty in M_1 of about 1% for the results shown here. In all but one sample, the error bars for M_1 correspond to 2%, for that sample (POPC-d_{31}/DPPC/cholesterol/10% melatonin), the signal to noise is significantly poorer and error bars of 3% are used.

Fortunately, the chain terminal methyl group splittings are always distinguishable from those of the methylene groups so we also use their quadrupolar splittings in sample comparisons. The methyl group splittings were measured directly as the frequency difference between the peaks in the methyl group powder patterns found near the center of each spectrum.

^{2}H NMR and Domain Size

NMR, like other spectroscopic techniques, has a characteristic time scale defined by the lifetime of a given state or coherence. If the quadrupolar splitting depends on the orientation of a molecule in the magnetic field then changes in that orientation due to molecular motion will result in changes in the quadrupolar splitting. If these changes are fast, the NMR spectrum will reflect the average orientation over these motions. Similarly if the quadrupolar splitting depends on the local environment of a molecule, for example if the molecule can be in either of two phases (such as the ℓ_o and ℓ_d phases) where the quadrupolar splittings are very different, then in the absence of any process which would lead to a molecule sampling both of these environments, the ^{2}H NMR spectrum would consist of two components having different quadrupolar splittings characteristic of the two environments. In the presence of rapid lateral diffusion or of compositional fluctuations which result in the molecule sampling both environments during the NMR time scale the spectrum would

consist of a single component having a motionally averaged quadrupolar splitting with a value somewhere between those observed in the two environments in the absence of such rapid molecular exchange. If the motions occur on an intermediate time scale (being of the same order as the NMR time scale) a broadening of the spectrum is observed. The NMR time scale in such cases is defined by the difference between the quadrupolar splittings of the two environments. If the splittings differ by δ kHz then the time scale is $1/(2 \cdot \pi \cdot \delta)$ ms.

If lateral molecular diffusion or compositional fluctuations within the bilayer leads to exchange of molecules between ℓ_o and ℓ_d domains then the size of these domains plays an important role in whether we can observe one or two distinct quadrupolar splittings [84, 112]. In the fluid phases of membranes the lateral diffusion constant is of the order of $2 \times 10^{-12} m^2/s$ so that for time scales of the order of 10 to 1000 μ s the molecules can diffuse root mean square distances of from 3 to 90 nm. If the domains are in this size range the NMR spectrum will show broadening due to this exchange process. If the domains are smaller the spectra would show a single average splitting while if the domains are much larger than this the spectra will show two splittings characteristic of the two environments.

Of course, if the fraction of labelled lipid in one phase or the other is much smaller than 1 the component of the spectrum arising from that phase will be much smaller than that from the other dominant phase. What fraction of the weaker component can be detected depends on the signal to noise of the final averaged spectrum. For the spectra presented here one could expect to observe components as small as 5% of the total with no difficulty.

2.5 Results and Discussion

2.5.1 ^{2}H NMR Spectra and Methyl Group Quadrupolar Splitting Analysis

The magnitudes of the ^{2}H quadrupolar splittings observed in ^{2}H NMR spectra of deuterium labelled lipid acyl chains are determined by the rapid motions which partially average the quadrupolar Hamiltonian. The character and time scales of these motions depend on sample temperature and composition. Because of this the ^{2}H NMR spectra (Figure 2.3 and

2.4) can be used to study the phase equilibria of lipid mixtures [80, 113]. Due to the large number of overlapping ^{2}H NMR powder patterns observed when using chain perdeuterated samples it can be difficult to measure and to follow the changes in individual methylene group quadrupolar splittings. However, it is quite easy to measure the splittings of the chain terminal methyl groups as they are considerably smaller than those of the methylene groups and their peak intensity is larger. Figure 2.5 shows expansions of the spectra to show the methyl components for all of the samples containing cholesterol, with and without added melatonin.

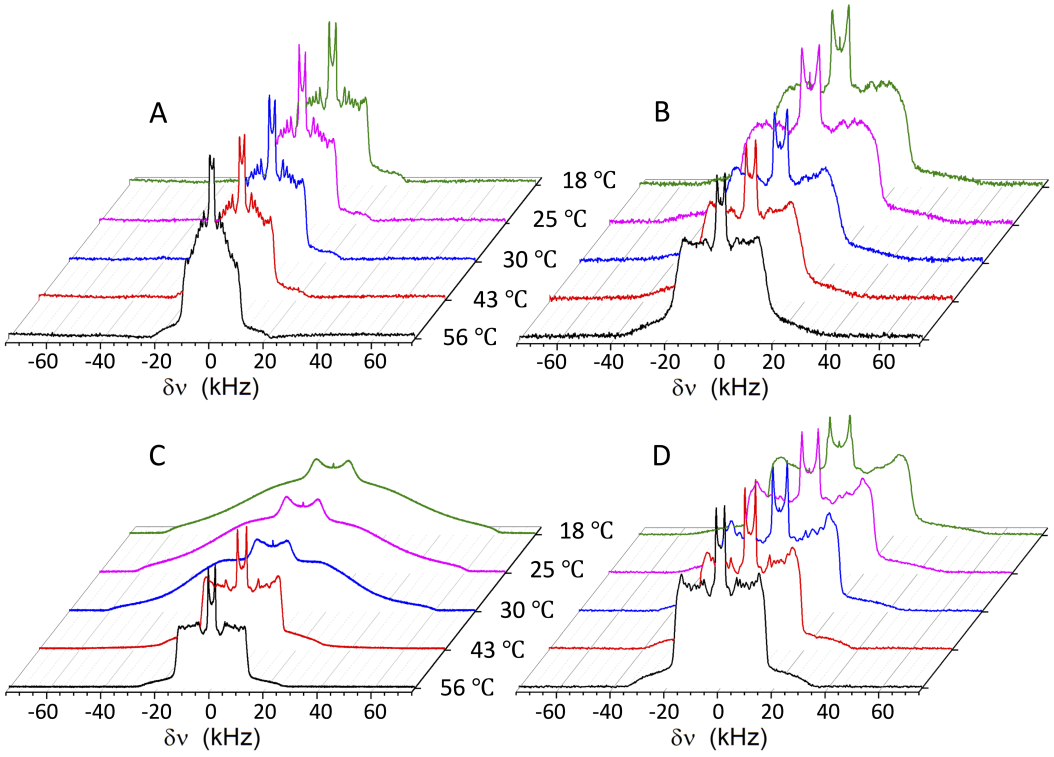


Figure 2.3: **^{2}H NMR Spectra of Lipid Membrane without Melatonin.** (A) pure POPC-d_{31}, (B) POPC-d_{31}/DPPC/cholesterol, (C) pure DPPC-d_{62} and (D) DPPC/POPC-d_{62}/cholesterol. The lipid membranes in B and D are SPM.

Figure 2.3A shows the temperature dependence of the ^{2}H NMR spectra observed in fully hydrated POPC-d_{31} bilayers. These spectra are characteristic of chain perdeuterated

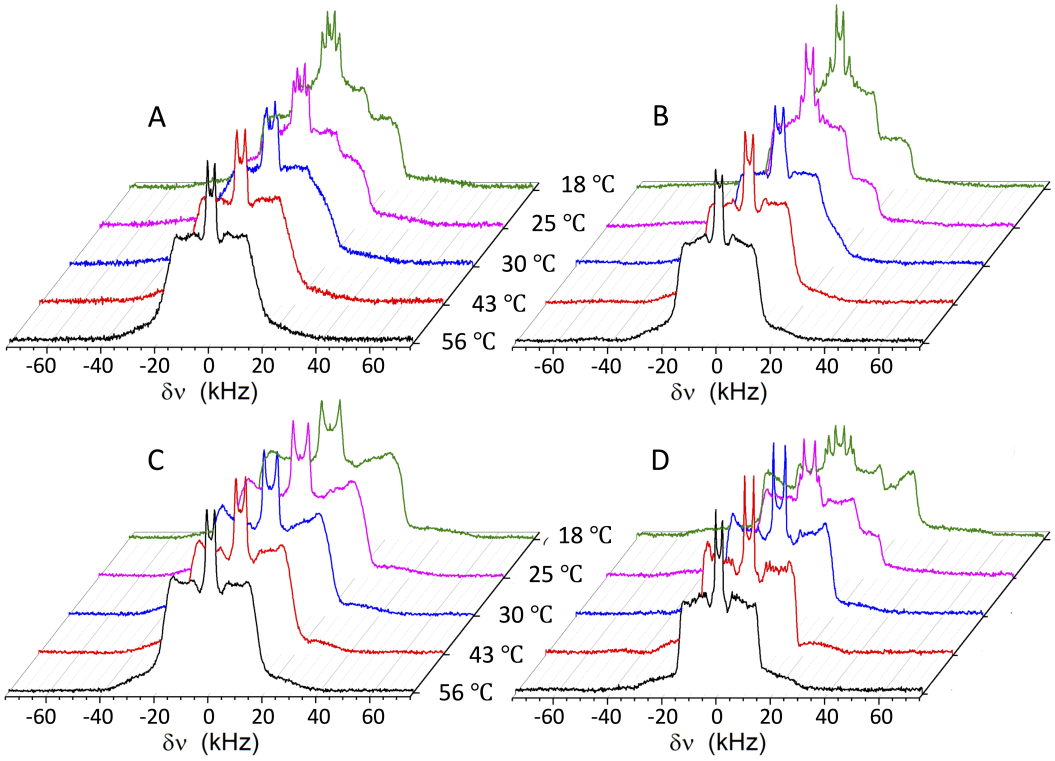


Figure 2.4: **^{2}H NMR Spectra of POPC-d$_{31}$/DPPC/cholesterol Lipid Membranes** with (A) 5% melatonin and (B) 10% melatonin. ^{2}H-NMR spectra of DPPC/POPC-d$_{62}$/cholesterol lipid mixture with (C) 5% melatonin and (D) 10% melatonin. The molar proportions of the lipids in all of the four mixtures are 3:3:2.

phospholipid lamellar dispersions in the 'fluid' or ℓ_d typically found in bilayers with little or no cholesterol. For POPC-d$_{31}$ the sample remains in the fluid phase to quite low temperatures because the chain melting transition occurs at around -4 °C for non-deuterated POPC [114]. We find that the transition for this sample of POPC-d$_{31}$ begins at approximately -7.5 °C but is more clearly evident at the next lower temperature, -9.5 °C.

Figure 2.3C shows the temperature dependence of the spectra of DPPC-d$_{62}$. Above about 37.75 °C [84] the sample is in the fluid phase but below that temperature it enters the gel phase where the ^{2}H NMR spectra are much broader due to the suppression of acyl chain *gauche-trans* isomerization resulting from the tighter chain packing in the gel

phase [106, 115]. The perdeuteration of DPPC lowers its melting temperature by about 4 degrees from 314 K to 310 K (41 °C to 37 or 38°C) [114]. Below this chain melting transition temperature, the chain motions are greatly restricted and their time scales are considerably longer. Thus, the ^{2}H NMR quadrupolar splittings are larger (less motional averaging) and the individual peaks in the spectrum are much broader (due to the slower motions). The spectral line shapes illustrated in Figure 2.3C are typical of fully hydrated phospholipid lamellar dispersions in the fluid and gel phases.

Over the range of cholesterol concentrations from 0 to at least 25%, the quadrupolar splittings in the fluid phase increase approximately linearly with increasing cholesterol concentration [116]. At sufficiently high cholesterol concentration, a phase separation into an ℓ_d:ℓ_o two phase region can occur [80, 84]. The ^{2}H spectra of chain perdeuterated lipids in the ℓ_o phase are similar to those of the ℓ_d phase except that the quadrupolar splittings are much larger (> 50 kHz compared to ≈ 22 kHz).

The spectra in Figure 2.3B are for a sample of POPC-d_{31}/DPPC/cholesterol with molar proportions of 3:3:2 while those in Figure 2.3D are for DPPC/POPC-d_{62}/cholesterol with the same molar proportions. For both samples the edges of the spectra have splittings $\Delta\nu_Q$ ranging from about 35 to over 55 kHz depending on temperature. These splittings are representative of a fluid lipid bilayer membrane at high cholesterol concentration [116]. In a ternary mixture containing a saturated chain phospholipid, an unsaturated chain phospholipid and a high concentration of cholesterol, one might have expected to find ℓ_d:ℓ_o phase coexistence (as for DOPC/DPPC/cholesterol mixtures [80]). The first row of spectra in Figure 2.5 shows expansions of the methyl group components of the spectra shown in Figure 2.3B and 2.3D. Careful inspection of this part of the spectra in Figure 2.3D reveals the inequivalence of the two hydrocarbon chains for DPPC-d_{62} which is a signature of a highly ordered phase [84, 116], with the values of the splittings plotted in Figure 2.6. Since only one chain is deuterated for POPC-d_{31} this feature is absent from the spectra in Figure 2.3B and Figure 2.5, and the detailed comparison of methyl splittings of the two sample kinds are displayed in Figure 2.6B. However, over the temperature range studied (from -7.5 to +57.3 °C), there is no evidence of coexistence of ℓ_d and ℓ_o phases. This agrees with other reports that do not detect microscale domains of similar ternary mixtures using POPC [82, 117, 118, 119, 120], This is in contrast to ternary systems

containing DOPC, with two unsaturated fatty acyl chains, where well-defined domains are observed by NMR [80, 82]. DPPC, having two unsaturated hydrocarbon chains, has a lower melting temperature, lower average hydrocarbon chain order parameter, and looser chain packing than POPC [114, 121] which has only a single unsaturated chain. In the presence of high concentrations of cholesterol, these factors seem to be sufficient to lead to detectable ℓ_d:ℓ_o phase separation in DOPC/DPPC/cholesterol but not in DPPC/POPC/cholesterol mixtures.

The addition of 5% melatonin (relative to total lipid, i.e., POPC plus DPPC plus cholesterol was 95%) to the DPPC/POPC/cholesterol mixtures with the same proportions used for Figure 2.4A and 2.4C has an interesting effect on the spectra. The sample with POPC-d_{31} shows a clear phase separation, and a closer look at the region of methyl group splitting on the spectra in Figure 2.5 also shows evident peak separation at 25 °C and 18 °C. By plotting the values of methyl group quadrupolar splittings as a function of temperature, as shown in Figure 2.6C, we see that the separation occurs at temperatures below about 28.4 °C. On the other hand, the sample with DPPC-d_{62} shows no evidence of phase separation over the temperature range studied. Repeating the experiments with a second set of samples having the same compositions gave identical results. Due to the looser chain packing of unsaturated lipids such as POPC, there is more room at the interfacial region (near the phospholipid headgroup) for melatonin to insert itself than in the more tightly packed regions rich in DPPC and cholesterol.

The average methyl group splitting for the POPC-d_{31} labelled sample with 5% melatonin is smaller than that of the corresponding sample with no melatonin primarily because of the presence of the much more disordered ℓ_d phase at temperatures below about 27.4 ° C. The addition of 5% melatonin slightly reduces the hydrocarbon chain order in this sample suggesting that melatonin preferentially partitions into the ℓ_d phase (see moment analysis below). The preferential partitioning of melatonin into regions rich in unsaturated lipids tends to enhance the difference in hydrocarbon chain order between areas rich in POPC and those rich in DPPC, especially since cholesterol interacts preferentially with saturated chain lipids and dramatically increases their hydrocarbon chain order. This competitive process between cholesterol and melatonin for the two different lipid species is supported by FT-IR and ^{1}H-NMR spectroscopy experiments of inverted lecithin micelles containing

melatonin and cholesterol that indicate an overlap in the stretching modes of melatonin's -NH with the -OH of cholesterol, and that chemical shifts of the NH protons of melatonin are sensitive to cholesterol content [122]. As noted above, chain perdeuteration shifts the phase transition temperature of either POPC-d_{31} or DPPC-d_{62} downward by about 4 °C. This has the effect of increasing the difference between the transition temperatures (and degrees of hydrocabon chain order) of the two lipids in the case of POPC-d_{31}/DPPC/cholesterol mixtures relative to DPPC/POPC/cholesterol, but it decreases those differences for the case of DPPC/POPC-d_{62}/cholesterol. The simple addition of melatonin at 5%, and the resulting decrease in chain order and transition temperature of POPC, seems to be enough to promote domain formation in one case but not in the other.

At 10% melatonin, the spectra of both samples, whether labelled with POPC-d_{31} or DPPC-d_{62}, show a broad region of ℓ_d:ℓ_o two phase coexistence in Figure 2.4B and 2.4D. It is also clear from the methyl group splitting in Figure 2.5, where a secondary peak with broader splitting appears over the original splittings as the temperature reduces. As might be expected, these spectra show that at a given temperature within the two phase region there is more of the unsaturated POPC in the ℓ_d phase and more of the saturated DPPC in the ℓ_o phase.

The expansions of the spectrum in Figure 2.5 showing the methyl group contributions at 0% melatonin, show only the presence of a single powder pattern above 25 °C for either POPC-d_{31} or DPPC-d_{62} labelled samples. For the DPPC-d_{62} sample, which has both chains deuterated, at 27 °C and below, we can see two partially resolved powder patterns indicative of the inequivalence of the two chains' methyl groups. This is a characteristic of a disaturated lipids in a highly ordered phase [80, 116]. In contrast, for samples containing 5% melatonin, the methyl group spectra clearly show two components for the POPC-d_{31} labelled sample due to ℓ_d:ℓ_o phase separation. The splitting of the ℓ_o phase component is slightly larger than the splitting observed in the absence of melatonin while the ℓ_d component has a significantly smaller splitting. The DPPC-d_{62} labelled sample shows the same general behaviour as in the absence of melatonin except that with the added 5% melatonin, the methyl splittings at lower temperatures are slightly larger than those in the absence of melatonin at the same temperatures. This is likely due to increased association of cholesterol with DPPC even though we cannot observe distinct ℓ_o phase domains at this

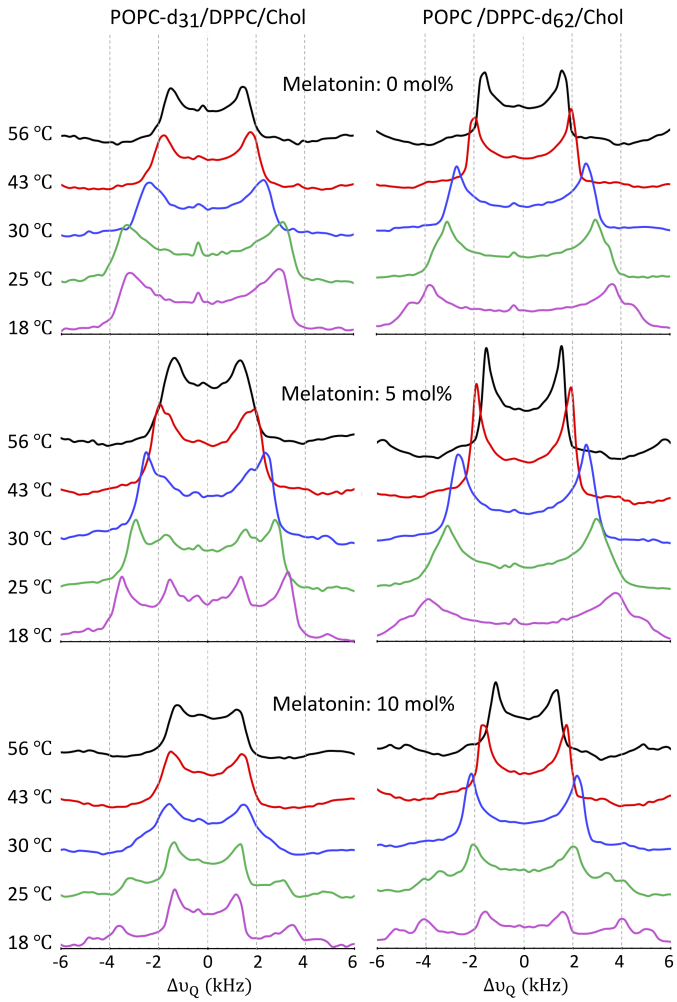


Figure 2.5: **Expansion of Methyl Group Component of the ^{2}H NMR Spectra of SPM.** The left column shows the methyl group spectra observed on samples with POPC-d_{31} and the right column shows the methyl group spectra observed on samples with DPPC-d_{62}. The melatonin concentration is 0%, 5%, and 10% from top to bottom.

concentration of melatonin. The methyl splittings of DPPC-d_{62} are slightly more sensitive to temperature in the presence of 5% melatonin than in the absence of melatonin. (See discussion below of the temperature dependence of the first moments of the full spectra).

With the addition of 10% melatonin, the methyl splittings of both samples show the phase separation in ℓ_o and ℓ_d phases. The relative intensities of the two components of these spectra show that at temperatures where both samples are in the two phase region (i.e., below about 26 °C), a larger fraction of the POPC-d_{31} is in the ℓ_d phase while more of the DPPC-d_{62} is in the ℓ_o phase. It should be pointed out that the small peaks near ±5 kHz in the spectra of the POPC-d_{31} labelled sample at 25 and 18 °C are due to the deuterium labels on the C-15 methylene group (notice how these splittings decrease with decreasing temperature), indicating that they arise from lipids in the ℓ_d phase while the larger methyl group splittings (near 4 kHz) are increasing as temperature is lowered indicating that they arise from lipid in the ℓ_o phase.

Figure 2.6A shows the temperature dependence of the methyl group splittings for samples of pure POPC-d_{31} and of pure DPPC-d_{62}. For POPC-d_{31}, there is only a gradual monotonic increase in the splitting of the single deuterated methyl group as the temperature is lowered from 59.8 °C to -6 °C. For DPPC-d_{62}, on the other hand, there are a couple of interesting changes. Just below 37.4 °C, there is a sharp increase in the splittings of both chain methyl groups as the sample is lowered through the chain melting transition from the fluid into the gel phase. This chain melting transition temperature is about 4 °C lower than the non-deuterated DPPC melting temperature at 41 °C [114]. In the gel phase at temperatures below the pre-transition from the L_α to the $P_{\beta'}$ phase but above the transition from the $P_{\beta'}$ phase to the $L_{\beta'}$ phase, the two methyl groups are inequivalent, one having a considerably larger splitting than the other [116]. This is because the *sn*-1 chain extends farther into the hydrophobic core than the *sn*-2 chain which is bent where it attaches to the phospholipid glycerol backbone. Even in the gel phase (in the pre-transition region ($P_{\beta'}$ phase)) there is significantly more chain mobility at the very center of the bilayer. However, below the pre-transition, the degree of order appears to have reached its maximum and the quadrupolar splittings of the two methyl groups are no longer distinguishable. In addition, at all temperatures above -7.5 °C, the methyl group splitting of POPC-d_{31} is smaller than those of DPPC-d_{62}.

The expanded portions of the spectra showing the methyl group components for the three component mixtures are shown in Figure 2.5, with the splitting values plotted against temperature in Figure 2.6B, 2.6C, and 2.6D. Here, at high temperatures, the POPC-d_{31} and DPPC-d_{62} methyl splittings are very similar with both gradually increasing as temperature is lowered. At about 27.4 °C we can see the development of the inequivalence of the two DPPC-d_{62} chains. This characteristic behaviour is observed whenever the lipid chains are sufficiently highly ordered [116]. We do not see any evidence of ℓ_d:ℓ_o phase separation, presumably due to the small size of any domains which may be present in the absence of melatonin [120].

For samples with 5% melatonin, Figure 2.6C shows that at higher temperatures the POPC-d_{31} and DPPC-d_{62} methyl splittings are again very similar. For the DPPC-d_{62} sample, however, below about 28.4 °C we see the return of the inequivalence of the two DPPC-d_{62} methyl groups but see no evidence of two phase coexistence. On the other hand, we see the appearance of two POPC-d_{31} methyl group splittings. These are due to the formation of the ℓ_d:ℓ_o two phase region observed in the full spectra in Figure 2.4A. An important signature of ℓ_d:ℓ_o two phase coexistence is the fact that in the ℓ_o phase domains the methyl group quadrupolar splitting (in the present case arising only from the single deuterated chain of POPC-d_{31}) increases as the temperature is lowered due to two factors: the reduced motional averaging at lower temperatures and the increased cholesterol content of the ℓ_o phase as the temperature is lowered. On the other hand, the methyl splitting of the ℓ_d phase decreases as the temperature is lowered due to the decreasing cholesterol content of the ℓ_d phase domains. This behaviour is conclusive evidence for the changing composition of the two phases with temperature.

Finally, in Figure 2.6D, we show the methyl group splittings for the samples containing 10% melatonin. At high temperatures, the methyl splittings for POPC-d_{31} are slightly smaller than those of DPPC-d_{62} due both to the increased chain disorder of unsaturated lipids relative to saturated lipids and to the higher affinity of melatonin for unsaturated lipids. Comparing the methyl group splittings with 5% melatonin (Figure 2.6C) to those at 10% melatonin, we also see that the increased melatonin concentration has reduced the hydrocarbon chain order and the methyl splittings.

At and below 30.9 °C, with 10% melatonin, the POPC-d_{31} methyl splitting has two com-

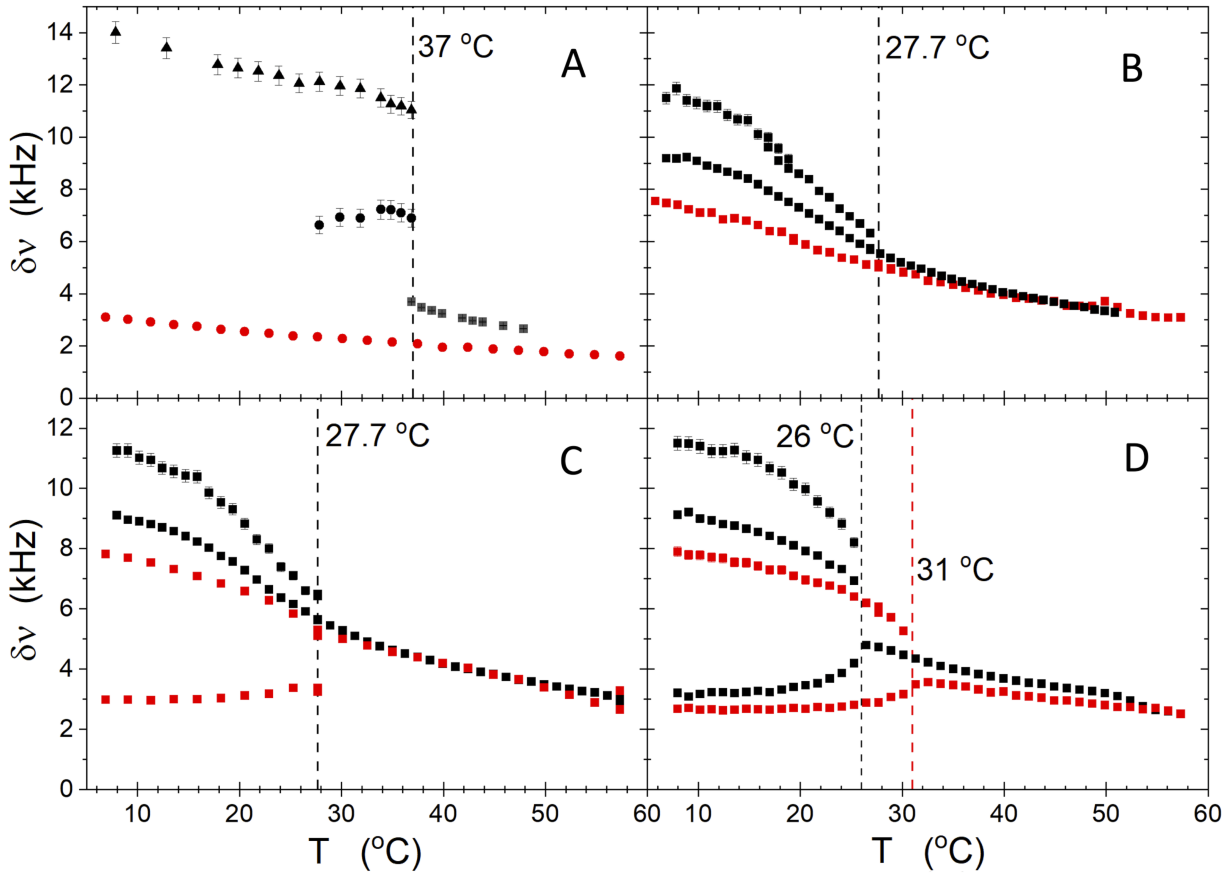


Figure 2.6: **Methyl Group Quadrupolar Splittings of Samples with POPC-d_{31} (*red*) and Samples with DPPC-d_{62} (*black*)**, shown with temperature dependence. (A) shows the quadrupolar splitting values of pure deuterated lipid samples and (B), (C), (D) show that of DPPC/POPC/cholesterol lipid mixture at molar proportions of 3:3:2 with 0%, 5%, and 10% melatonin, respectively. Lower values of splittings correlate with less order of the lipid tails, while higher values of splittings indicate the opposite way.

ponents indicating that the phase separation has begun. On the other hand, for the sample with DPPC-d_{62} the methyl splittings show that phase separation occurs only for temperatures below about 25.9 °C. Recall, however, that at 5% melatonin no phase separation was observed for the DPPC-d_{62} sample over the temperature range studied. As discussed above, chain perdeuteration of POPC-d_{31} increases the difference between POPC-d_{31} and DPPC

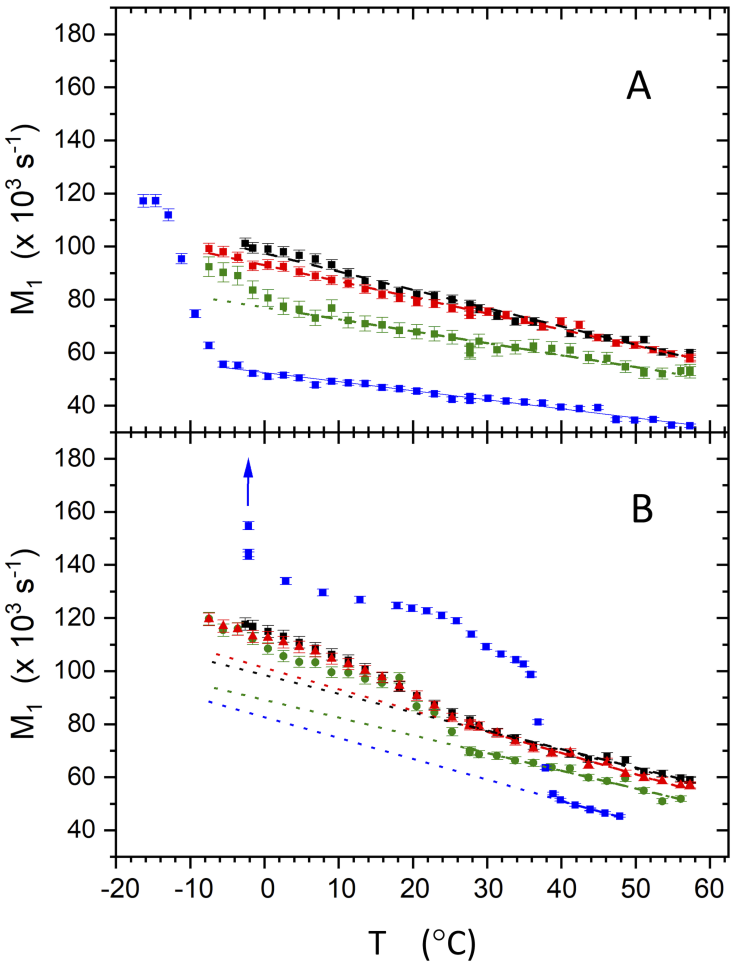


Figure 2.7: **First Moments of the ^{2}H Spectra** of Pure samples (*blue*) and lipid mixture of DPPC/POPC/cholesterol at molar proportions of 3:3:2 with 0% (*black*), 5% (*red*), and 10% (*green*) melatonin, shown with temperature dependence. Samples with POPC-d_{31} are shown in (A), samples with DPPC-d_{62} are shown in (B).

chain melting transition temperatures, while chain perdeuteration of DPPC-d_{62} reduces the difference between DPPC-d_{62} and POPC. Evidently the DPPC/POPC/cholesterol ternary mixture is closer to fluid-fluid phase separation when POPC-d_{31} is labelled as compared to perdeuteration of the DPPC chains which pushes the system farther from the phase coexistence regime so that higher concentrations of melatonin (in this case 10%) are required

to promote phase separation.

2.5.2 First Moment M_1 Analysis

Figure 2.7 shows the values of the first moment, M_1, of the ^{2}H spectra of all of the samples: Part (A) of the figure is for the spectra of samples prepared using POPC-d_{31} while part (B) is for those with DPPC-d_{62}. The blue squares are for the pure phospholipid/water dispersions, POPC-d_{31} in (A) and DPPC-d_{62} in (B). The rapid increase in M_1 of POPC-d_{31} below - 7.5 °C is due to the transition from the fluid or liquid-disordered phase into the gel phase. Similarly, the rapid increase at about 38 °C for the DPPC-d_{62} sample is due to its ℓ_d to gel phase transition.

The first moments of spectra from ternary mixtures of POPC, DPPC and cholesterol at molar proportions of 3:3:2, without melatonin, are shown as the black squares in the figure. At higher temperatures (above about 28 °C) the values of M_1 for samples with either deuterated POPC or deuterated DPPC are very similar, indicating that both lipids experience the same environment and have the same average hydrocarbon chain order. The addition of melatonin to these mixtures (at the 5% level) has little impact on the average chain order of either lipid (M_1 values for these sample are shown as red squares in the figure). Increasing the melatonin concentration to 10% results in a 10 to 15% reduction in M_1 for temperatures in the ℓ_d phase for both POPC and DPPC labelled samples.

Below about 26 °C the samples labelled with DPPC-d_{62} show a slightly more rapid increase in M_1 as the temperature is lowered. However, the slopes of the plots of M_1 vs temperatures for the samples labelled with POPC-d_{31} remain essentially unchanged at 5% melatonin but not at 10%. This is in spite of the fact that the spectra of the POPC-d_{31} samples with 5 and 10% melatonin show ℓ_d:ℓ_o phase coexistence, while the DPPC-d_{62} samples only show two phase coexistence for the 10% melatonin sample.

For all the samples studied these mixtures are in a single fluid phase at temperatures above about 30 °C (for the pure DPPC-d_{62}/water mixtures this is only true above about 38°C). Over this temperature range the variation of M_1 with temperature is approximately linear and we can determine the values of dM_1/dT by a linear fit of the values of M_1. The

Sample Composition	$dM_1/dT(s^{-1}/^{\circ}C)$	$\pm$
POPC-d_{31}	-341	10
POPC-d_{31}/DPPC/cholesterol/0% melatonin	-689	17
POPC-d_{31}/DPPC/cholesterol/5% melatonin	-606	11
POPC-d_{31}/DPPC/cholesterol/10% melatonin	-450	24
DPPC-d_{62}	-758	46
DPPC/POPC-d_{62}/cholesterol/0% melatonin	-698	42
DPPC/POPC-d_{62}/cholesterol/5% melatonin	-784	30
DPPC/POPC-d_{62}/cholesterol/10% melatonin	-668	42

Table 2.1: **Slopes (dM_1/dT) of the Linear Regression Lines Shown in Fig 2.7 for All the Samples.**

results for all samples are shown in Table 2.1. From this table it is clear that the hydrocarbon chain order of the DPPC-d_{62}/water mixture is much more sensitive to temperature (with a slope of - 758) than that of POPC-d_{31}/water (with a slope of -341). This results in the relatively high transition temperature from the ℓ_d phase to the gel phase.

For the ternary mixtures of DPPC/POPC/cholesterol the values of dM_1/dT are very similar whichever phospholipid is deuterated. The addition of melatonin has little effect on the values of dM_1/dT for the samples using DPPC-d_{62}. However, the addition of 10% melatonin to the sample with labelled POPC-d_{31} substantially reduces dM_1/dT.

2.5.3 Significance and Physiological Implications

The results of the work presented here have important implications in understanding fundamental physical properties of model lipid membranes and effect of small molecules, such as melatonin, on the lipid ordering in complex multicomponent bilayers, that are capable of forming domains.

In this regard, the work presented here may provide an insight on the molecular mechanism of melatonin protection in cellular membranes and thus has implications for health and disease. It is important to note that the DPPC/POPC/cholesterol model (with/without

melatonin) used here are completely fluid near physiological temperatures and do not exhibit detectable domain formation. Moreover, the physiological levels of melatonin are expected to be much lower than what was tested here, though local concentrations within membranes have not been determined *in vivo* [123]. Previous research from Garcia *et al* [124] showed that melatonin aids in maintaining membrane fluidity under oxidative stress and reducing lipid peroxidation products. Melatonin is a well-established, potent free radical scavenger [125], however it has not been shown to have oxidative chain reaction breaking properties in the membrane [126]. This may suggest that it is more likely to protect from lipid peroxidation by preventing free radicals in the aqueous phase from initiating oxidation processes, as suggested by others [122]. Our work indicates that the protective effects of melatonin may also be influenced by an intrinsic preference for the more disordered lipid phase with higher degree of unsaturated bonds (like POPC). A preference for disordered domains would position melatonin closer to the sites most susceptible to the initiation of lipid peroxidation.

The implications of this current work for direct membrane protection from Aβ toxicity in AD are less obvious, aside from the benefits of preventing oxidative stress and lipid peroxidation which are features of Aβ toxicity. It has been shown that Aβ accumulates preferentially on rigid ordered membrane domains [127], thus the ability of melatonin to induce phase separation may be expected to facilitate the binding of Aβ to ordered membrane domains, however the situation is much more complicated. The level of cholesterol within the membrane has been shown to inversely correlate with Aβ-membrane binding and cell death [128, 129] and electrostatic domains induced by cholesterol seem too affect membrane damage by Aβ [130], but in other studies increased cholesterol was associated with increased susceptibility to Aβ *without* any increase in Aβ-membrane interactions [93, 131]. Yet other studies have demonstrated the opposite correlation, where depletion of cholesterol increased cytotoxicity and cholesterol enrichment was shown to be protective [91, 132, 133]. These controversial and seemingly contradictory effects point to the fact of how complex Aβ-membrane interactions are in AD and thus we cannot preclude the possibility that stabilizing or inducing membrane phase separation is protective against Aβ. This controversial effect may depend on the size of the domains in the membrane. From our results here, it appears that melatonin is increasing the difference in order between the

domains to promote phase separation while simultaneously decreasing average fatty acid chain order. It is not clear whether the differences in order between membrane domains or the absolute order of the domains is more important for Aβ-membrane binding affinities or Aβ induced membrane damage. Obviously, complete elimination of membrane domains to protect them from Aβ toxicity is not feasible as these domains are necessary for cells to function. The question that needs to be answered in relation to melatonin's ability to modify membrane properties to prevent Aβ damage directly is far more nuanced and requires further study.

2.6 Conclusion

In this work we used ^{2}H-NMR to study phase separation of DPPC/POPC/cholesterol model lipid membranes to understand the effects of melatonin on phospholipid bilayers. Melatonin induces ℓ_d:ℓ_o phase coexistence in the DPPC/POPC/cholesterol mixtures, in both POPC-d_{31} and DPPC-d_{62} containing samples. This effect was observed in the POPC-d_{31} containing lipid mixtures at half the concentration as for the DPPC-d_{62} containing lipid mixtures, 5% melatonin compared to 10% melatonin, which suggests that melatonin preferentially interacts with the unsaturated lipid (POPC). Based on our results and other relevant literature we suggest that a competition between melatonin and cholesterol results in the displacement of cholesterol by melatonin in the more disordered phase, which acts to increase the disorder in that phase, while driving more cholesterol into the DPPC rich ordered phase and thus promoting the separation of ℓ_d:ℓ_o phases. POPC has a larger area per molecule than DPPC, therefore there is more free space in the headgroup region which allows more melatonin to incorporate into POPC enriched domains. This may help to explain melatonin's antioxidative mechanisms of action. In addition, the perdeuteration of lipid chains lowers the melting temperature of the corresponding lipid, which increases the difference between POPC-d_{31} and DPPC (from about 45 to about 47.5 °C), and reduces the difference between DPPC-d_{62} and POPC (from about 45 to about 41 °C). In this simple DPPC/POPC/cholesterol model membrane system, melatonin clearly acts to promote membrane fluid phase heterogeneity. Considering the importance of membrane domains in amyloid toxicity reported in the earlier work by Drolle *et al.* [2, 130], this data

will be important to guide future studies on melatonin's protective role on a membrane level.

Chapter 3

Localized Surface Plasmon Resonance and Atomic Force Microscopy Study of Model Lipid Membranes and Their Interactions with Amyloid and Melatonin

3.1 Overview

3.1.1 Summary of Submitted Work

The study explored the interaction of Aβ aggregates with lipid membrane models that represented different AD stages, using AFM and LSPR. It also aimed to study melatonin's protective effect on the model lipid membranes against amyloid toxicity. By using LSPR, the build-ups of the amyloid layer on the model lipid membranes were measured through changes in the effective thickness of the layer, resulting in shifts in absorbance wavelength. The impact of these amyloid aggregates was found to vary with the lipid

membrane composition, which was relevant to the disease state. The research discovered that both amyloid aggregation and melatonin's protective effect were dependent on the disease stage of the membrane, with early-stage disease showing the most amyloid aggregation and the strongest melatonin protection. The results suggested that melatonin might have counteracted amyloid aggregation on lipid membrane in the early stages of AD.

3.1.2 Contributions

Under the supervision of Dr. Zoya Leonenko, I designed this study using neuron cell lipid membrane models developed by Dr. Elizabeth Drolle [134] to correspond with different disease states. I led the entire project and supervised an undergraduate student, Jingwen Liang, for two terms. I trained her on the LSPR instrument and utilized her assistance in data collection. Later, I completed the data analysis independently. Dr. Danielle M. McRae assisted with manuscript preparation, contributing to the abstract writing, LSPR theory, and discussion editing, as well as providing general proofreading. I would like to thank them both for their contributions to this study.

3.1.3 Challenges and Future Directions

The work with LSPR proceeded smoothly in terms of data collection. Although issues with system leakage and clogging hindered progress for a time, I managed to fix the problems with technical support from Nicoya Lifesciences. It's important to note that each individual experiment required a new sensor, as a reused sensor, even when cleaned according to the proper protocol, exhibited lower sensitivity compared to a new one. The calibration of sensor sensitivity was found to be reliable only with new sensors. Another challenge was that the evanescent wave decay length, a parameter tied to the sensor's property, could not be measured with our instruments, nor could assistance be found to overcome this obstacle. Therefore, this parameter remained unresolved in the results and was treated as a constant factor, considered to have no effect on the findings.

Future work on amyloid-membrane interaction, or any other peptide-membrane interactions, is feasible with the LSPR technique. Utilizing the protocols developed for data

collection and analysis, one should encounter no difficulties in reproducing this study or conducting new research. For example, to delve into further details concerning melatonin's protective effect, one might consider modifying the concentrations of melatonin in the buffer or experimenting with different lipid membrane models.

3.2 Abstract

Alzheimer's disease (AD) is a progressive neurodegenerative disorder characterized by the accumulation of amyloid plaques in the brain. The toxicity of amyloid to neuronal cell surfaces arises from interactions between small intermediate aggregates, namely amyloid oligomers, and the cell membrane. The nature of these interactions changes with age and disease progression. In our previous work, we demonstrated that both membrane composition and nanoscale structure play crucial roles in amyloid-membrane interactions. This understanding introduces the possibility of modifying membrane properties to shield them from amyloid-induced damage. In this study, we employed atomic force microscopy (AFM) and localized surface plasmon resonance (LSPR) to investigate the protective effects of melatonin. We utilized synthetic lipid membranes that mimic the neuronal cellular membrane at various stages of AD and explored their interactions with amyloid-β (Aβ) (1-42) in the presence of melatonin. Our findings reveal that the early diseased membrane model is particularly vulnerable to amyloid binding and subsequent damage. However, melatonin exerts its most potent protective effect on this early-stage membrane. These results suggest that melatonin could act at the membrane level to alleviate amyloid toxicity, offering the most protection during the initial stages of AD.

3.3 Introduction

Alzheimer's disease (AD) is a progressive neurodegenerative disorder that primarily affects the elderly population [7, 10, 135, 136]. Despite extensive research, the molecular mechanisms of AD are not well understood which delays the development of a cure and preventive strategies. Amyloid plaques, a hallmark of AD [10] are found on neuronal cell

surfaces and are composed of misfolded and entangled amyloid-β (Aβ) fibrils [137]. Aβ (1-40) and Aβ (1-42) are the most common fragments which originate from the transmembrane amyloid precursor protein (APP) cleavage [8, 138, 139, 138, 140]. Through process of misfolding and aggregation these monomer fragments result to formation of small soluble amyloid oligomers and large fibrils, all of which interact with cellular membranes inducing cellular damage (amyloid toxicity). Previous clinical, animal and cellular studies have demonstrated that small soluble amyloid oligomers are more toxic to neurons than large fibrils [141, 142].

While specific amyloid receptors are present in neuronal cells, it is known that Aβ can also interacts with cellular membranes non-specifically, inserting into the membrane and leading to membrane damage in the way of defects, pore and ion-channel formation [20, 73, 138, 139, 143], which has been linked to the initiation of pathogenesis in the early stages of AD [144].

In spite of more than hundred years of research, there is currently no cure available for AD [145], and therefore the developments of preventive measures are in much demand and are highly researched. Multiple cellular and animal studies have demonstrated that melatonin can be protective against Aβ neurotoxicity but the molecular mechanisms of this protection are not well understood [45]. Melatonin is a hormone secreted by the pineal gland in the brain and regulates circadian rhythm, seasonality, and has antioxidative and immune response effects [7, 43, 44]. It has been shown that the levels of melatonin decrease with aging and neurodegeneration [50]. Previous studies on melatonin's effect on model membranes have revealed that it is able to fluidize the membrane while enhancing the lipid dynamics and increasing the area per lipid [44, 51, 53]. It counteracts the ordering effect of cholesterol [3, 146] and acts similarly to its biosynthetic precursors tryptophan, serotonin and N-Acetylserotonin (NAS) [103]. With nuclear magnetic resonance (NMR), melatonin was also shown to influence the phase separation in the DPPC/POPC/cholesterol membrane model [52]. In order to understand the mechanisms of melatonin protection against amyloid toxicity, it is important to study the role of melatonin in Aβ-membrane interactions. Due to its ability to alter the surface properties of the membrane, melatonin may exhibit an effect on non-specific interactions between amyloid and cellular membranes, which may protect the membranes from amyloid toxicity.

We and others have previously demonstrated that changes in lipid composition, consequently involving different lipid charges and phases, affect membrane interactions with amyloid peptides [2, 31, 73, 130, 147, 148, 149, 150, 151, 152, 153]. As reported earlier, the changes in the lipid composition of the plasma membrane due to aging have been observed in early-state AD, and such changes are closely related to the early development of AD and affect Aβ toxicity [2, 154]. Due to the high complexity of cellular membranes, model membranes composed of synthetic lipids are widely used to investigate the interaction between Aβ and the membrane [155, 156]. Our previous study has demonstrated that changes in the composition of model lipid membranes, mimicking the changes in neuronal membranes in health and in AD, cause changes in the membrane nanoscale structure (nanodomains) and dramatically alter the damaging effect of Aβ in such model membranes [2]. Therefore, we hypothesized that protecting the membrane with membrane-active molecules, such as melatonin, can reduceAβ toxicity. In this study, complex model lipid systems developed by Drolle *et al.* [2] were employed to model neuronal cell membranes in various states of AD (Table A.1). The interactions between amyloid and the membranes, in the presence or absence of melatonin, were studied using localized localized surface plasmon resonance (LSPR). Complementary atomic force microscopy (AFM) images were also utilized to visualize the membrane surfaces and Aβ-membrane interactions.

3.4 Materials and Methods

In this study, supported lipid membranes were prepared by method of vesicle fusion [157] onto mica and sensor surface for AFM and LSPR, respectively. Once attached to the substrate, individual vesicles or liposomes rupture into a single membrane and then connect to form a continuous membrane that covers the entire substrate surface. Details of preparing the membranes and experimental techniques are discussed in the following sections.

3.4.1 Lipid Membrane

DPPC, POPC, cholesterol, SM, GM1 and melatonin were purchased from Sigma-Aldrich and all chemicals were used without further purification. In this study, three lipid models

that mimic neuronal cell membranes at different disease states of AD were utilized. Composition details are shown in Table A.1. Stock solutions of DPPC, POPC and cholesterol at 10 mg/mL, and SM and GM1 at 1 mg/mL were prepared with chloroform and stored at -20 $°C$. The stock solutions were mixed and dried with a gentle flow of nitrogen and then resuspended into a buffer to produce a homogeneous lipid vesicle solution [36].

	Lipid components in weight ratio (molar ratio)				
Lipid Models	DPPC	POPC	Cholesterol	SM	GM1
Healthy Model (HM)	37 (35.3)	37 (34.1)	10 (18.1)	10 (9.8)	6 (2.7)
Early Diseased Model (EDM)	39 (36.5)	39 (35.2)	10 (17.8)	10 (9.7)	2 (0.9)
Late Diseased Model (LDM)	42 (39.4)	42 (38.0)	10 (17.8)	4 (3.9)	2 (0.9)

Table 3.1: **Lipid Compositions of the Three Model Membranes** mimicking different disease states of neuronal cell membranes in AD: healthy model (HM), early diseased model (EDM), and late diseased model (LDM) membranes. The ratios are shown by weight. Adapted from Drolle *et al.*, 2017 [2].

Melatonin is known to have high solubility in hydrophobic solvents [158], and thus readily partitions into the lipid membranes from water-based solutions, as melatonin has limited solubility in polar solvents. Melatonin stock solution was prepared with ethanol, and it was dried with nitrogen flow and then resuspended in buffer. It was dissolved in buffer at near saturation (400 μM) and the buffer was added to the supported membranes and incubated at least 30 min to allow melatonin to partition into the membrane. Freshly prepared buffer solutions,composed of 20 mM HEPES and 150 mM NaCl (pH=7.4), were used.

The supported lipid bilayer (SLB) on the LSPR sensors was created within the LSPR system, with further details discussed below in the LSPR section. After depositing the membrane on a sensor surface, the LSPR sensor was removed from the LSPR liquid cell and affixed to a microscope slide for AFM imaging. A Teflon ring was positioned around the sensor to retain water during AFM imaging. For AFM imaging of amyloid binding to the membrane, the SLB was formed on mica by vesicle fusion. Excess liquid was then carefully removed using a pipette, followed by rinsing the surface five times with 600 μL

of deionized (DI) water. The liquid cell was subsequently left with approximately 800 μL of water inside for 90 minutes before collecting AFM images.

3.4.2 Aβ Solution Preparation

The Aβ (1-42) peptide was acquired from rPeptide and aliquoted using the hexafluoroisopropanol (HFIP) protocol [159]. A concentration of 1 mg/mL was achieved by adding HFIP to the amyloid vial, which was then sealed and sonicated for 30 seconds to ensure complete dissolution. The vial was subsequently left in a fume hood for incubation for 15 minutes, after which 45 μL aliquots of the Aβ-HFIP solution (0.01 μmol Aβ peptides) were prepared and dried in the fume hood overnight. The aliquots were stored at -20 $^{\circ}C$ for future use.

An appropriate buffer solution, with or without melatonin, was used for all solution preparation. Aβ solution (50 μM) was prepared immediately prior to each injection by adding 200 μL of buffer solution to one amyloid aliquot and then sonicating for 10 minutes. This preparation of Aβ solution ensures the monomeric and oligomeric forms of the peptide when it interacts with the membrane surface.

3.4.3 Atomic Force Microscopy

Atomic force microscopy (AFM) is a scanning probe microscopy technique involving the scanning of a sharp probe over a sample surface to measure topography with nanoscale resolution. AFM can operate in air or liquid environments [2, 160, 161], critical to maintaining physiological conditions for biological studies [20, 36, 162], and for our study of lipid membranes here. For this study, the JPK NanoWizard II AFM system was used with qp-BioAC AFM probes from Bruker to image samples in the intermittent contact mode. The CB1 tip (resonance frequency of 90 kHz) was utilized for unused LSPR sensor imaging and the CB3 tip (resonance frequency of 30 kHz) was used for all other imaging purposes.

All images were processed using Gwyddion [4] software with minimal filtering and correction steps to level the image background and eliminate noise. Surface roughness, along with difference in height of the surface (Δh), were determined by the software.

3.4.4 LSPR Theory and Experiments

LSPR Theory

Localized surface plasmon resonance LSPR sensing is a biosensing technique that exploits the optical properties of metal nanoparticles to measure molecular interactions or bindings, such as DNA and RNA binding [163, 164], antibody-antigen interactions [165, 166, 167, 168], and small-molecule detection [169], etc. In surface plasmon resonance, an oscillation of charge density at the interface of a metal and a dielectric, such as a thin layer of gold or silver in air or water, is excited by incident light at a certain angle, resulting in a propagating wave along the surface [170]. Localized surface plasmon resonance further confines this resonance to a nanoparticle smaller than the wavelength of the incident light, resulting in the collective oscillation of free electrons of the metal nanoparticle, leading to a highly localized and enhanced plasmon wave [64]. The resonance wavelength of LSPR is highly dependent on the local environment of the metal nanoparticle, such that a change in the local refractive index will correspond to a change in the resonance wavelength. This parameter is exploited in LSPR biosensing, where the resonance wavelength is measured, and its shift can be correlated to changes in the local dielectric environment of the metal nanoparticle sensor, including binding events. Figure 3.2A illustrates the experimental set-up of the ?? (??) sensor, while Figure 3.2B depicts the strong absorption peak associated with the LSPR and its shift ($\Delta\lambda$) corresponding to a change in the local dielectric environment of the GNP sensor.

The measured wavelength shifts $\Delta\lambda$ can be translated into changes in the thickness, d, of the adsorbate layers building up on the LSPR sensing surface. The following expression explains the general relationship between these two parameters [171]:

$$\Delta\lambda = m\Delta n(1 - e^{-\frac{2d}{l_d}}) \tag{3.1}$$

where m represents the sensitivity factor of the sensor, Δn denotes the change in refractive index in the vicinity of the sensing surface due to molecular binding and l_d is the evanescent field decay length that defines the sensing distance of the GNP sensor. When no molecules bind to the sensor, the first layer is the bulk buffer solution that has

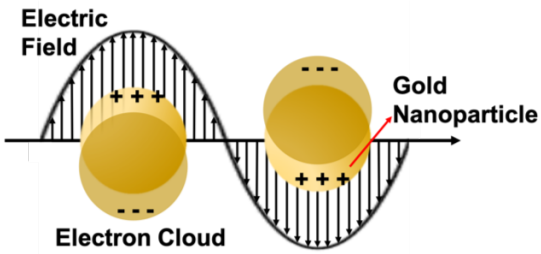


Figure 3.1: **Schematic of the LSPR Induced by Electric Field** The electric field associated with the incident light induces the electron cloud of the gold nanoparticles to oscillate collectively to generate a localized surface plasmon.

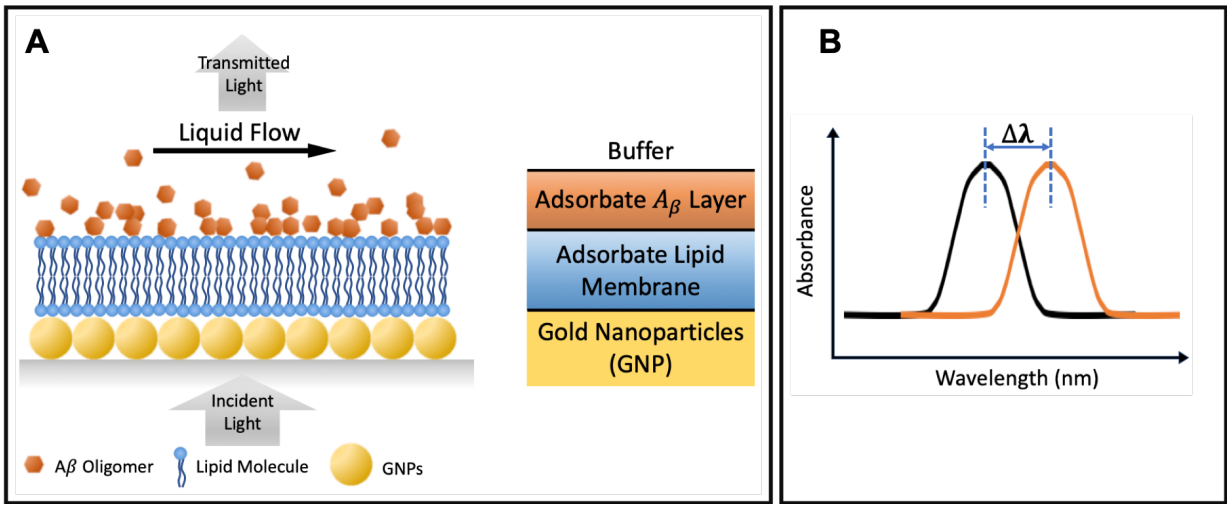


Figure 3.2: **The LSPR Experiment Design and Measurement Principle** (A) Schematic view of an LSPR sensing surface used in the experiment. A lipid membrane assembles onto the GNP sensor. The solution containing Aβ flows over this membrane, leading to the accumulation of oligomers on the surface. Incident light travels through the sensing area, starting from the GNP side, and the transmitted light is then measured on the opposite side. Simplified model demonstrating the adsorbed layers producing LSPR signals for analysis is shown on the right. (B) The initial absorption spectrum of the transmitted light is shown as a black curve. As layers of molecules accumulate on the sensor, the absorption peak of the spectrum shifts, shown as the orange curve. This shift, represented as $\Delta\lambda$, is recorded for analysis.

approximately infinite thickness ($d = \infty$) compared to the sensing distance of the GNPs. Therefore, Equation (3.1) can be simplified into

$$\Delta\lambda = m\Delta n \tag{3.2}$$

In this case, m can be determined as the slope of a calibration curve, where various $\Delta\lambda$ values are measured as a function of refractive indices for sequentially diluted standard solutions.

Equation (3.1) is valid for LSPR responses to a single layer with a uniform thickness (or the effective thickness of a non-uniform layer). In our experiments, this can be applied directly to the membrane formed on the GNPs. Ultimately, a second layer of Aβ peptides will cover the pre-formed membrane. This adsorption on the sensor is illustrated in Figure 3.2 with the membrane being the first layer and the Aβ layer being the second. The LSPR response to the formation of the Aβ layer will be distinct from the formation of the membrane layer, as the membrane layer dampens the response of the nanoparticle sensor to the second binding event. To account for this, Equation (3.1) can be modified by multiplying an additional scaling factor, $e^{-\frac{2d}{l_d}}$ [171]. Therefore, $\Delta\lambda_{A\beta}$ for Aβ binding can be expressed as

$$\Delta\lambda_{A\beta} = m\Delta n_{A\beta}(1 - e^{-\frac{2d_{A\beta}}{l_d}})e^{-\frac{2d_{mem}}{l_d}} \tag{3.3}$$

where $d_{A\beta}$ is the effective thickness of the Aβ layer and d_{mem} is the effective thickness of the membrane. As our goal is to measure the thickness of the membrane and Aβ layers, we can rearrange Equation (3.1) and (3.3) as expressions of d_{mem} and $d_{A\beta}$, respectively:

$$\frac{d_{mem}}{l_d} = -\frac{1}{2}ln(1 - \frac{\Delta\lambda_{mem}}{m\Delta n_{mem}}) \tag{3.4a}$$

$$\frac{d_{A\beta}}{l_d} = -\frac{1}{2}ln(1 - \frac{\Delta\lambda_{A\beta}}{m\Delta n_{A\beta}(1 - \frac{\Delta\lambda_{mem}}{m\Delta n_{mem}})}) \tag{3.4b}$$

$\Delta\lambda_{mem}$ and $\Delta\lambda_{A\beta}$ are the measurable experiment responses; Δn_{mem} and $\Delta n_{A\beta}$ are the differences of the refractive indices of the membrane and Aβ to the bulk buffer solution, respectively.

The refractive index of the buffer solution was taken to be 1.334 [172], the refractive index of the membrane was estimated to be 1.47 [173, 174, 175, 176, 177], and the refractive

index of Aβ was calculated as 1.6 [178]. As discussed with Equation (3.1), m is the sensor's sensitivity factor, which can be determined as the slope of the calibration curve. We used standard glucose solutions with a series of concentration gradients and known refractive indices [179] to generate the calibration curve and obtain m. The parameter l_d, in the commercial LSPR sensor, has a defined range of 20-40 nm. Due to the $> 50\%$ uncertainty of this parameter, it is kept as an unknown constant in the final calculations, expressed as d/l_d, as shown in Equation (3.4) for each layer (membrane, d_{mem} or amyloid, $d_{A\beta}$). Therefore, we define a new parameter T as the thickness profile to represent the quotient:

$$T = \frac{\text{adsorbed layer thickness } (d)}{l_d} \tag{3.5}$$

Overview of the LSPR Experiments

In this study, the OpenSPR and gold nanoparticle sensors from Nicoya Lifesciences were used. Figure 3.2A illustrates the experimental set-up inside the fluidic chamber for the LSPR experiment. A GNP sensor was pressed and sealed onto the fluidic chamber during the experiment. Before conducting the experiment, the fluid chamber was thoroughly cleaned with 80% isopropanol to eliminate any air bubbles in the loop, while maintaining the pump speed at 150 μL/min. Then at a pump speed of 20 μL/min, two consecutive injections of lipid solution were carried out, with a 5-minute interval in between to produce a stable membrane covering the sensing surface through lipid fusion. Following this step, the pump speed was maintained at 20 μL/min to allow for stabilization of the membrane. The amyloid solution was prepared as detailed in Section 2.2 and injected immediately afterward. After the injection of amyloid, the system was allowed to run for another 10 minutes to finish the experiment. A representative LSPR sensorgram is shown in Figure 3.3.

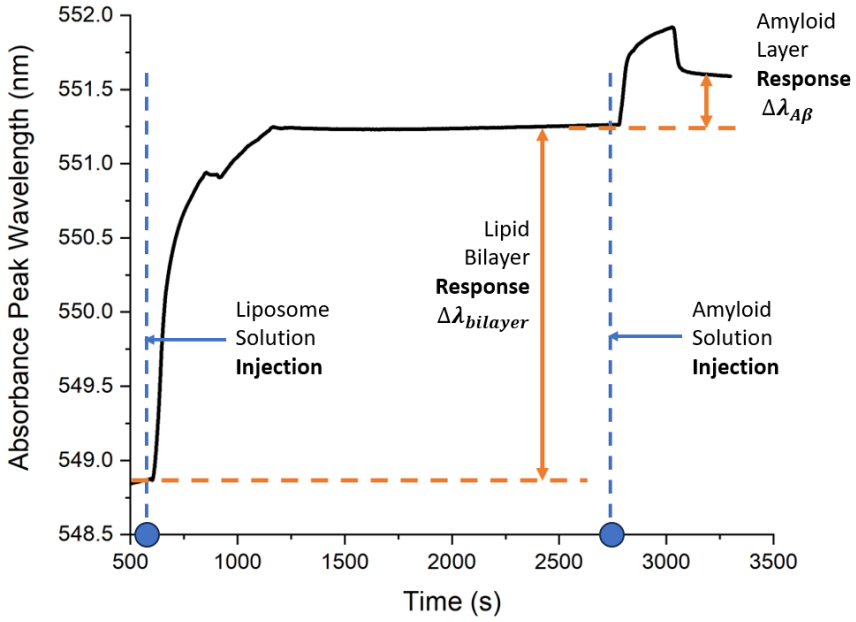


Figure 3.3: **LSPR Sensorgram.** LSPR sensogram shows the change in wavelength of absorbance peak VS time after each injection: first is the liposome solution and formation of lipid bilayer followed by amyloid injection and build up of amyloid layer on the top of the membrane. Each pair of blue dashed line and circle indicates the time point of each solution injection. The two orange arrows indicate the respective sensor responses due to each layer formation. The responses are labeled as $\Delta\lambda_{mem}$ and $\Delta\lambda_{A\beta}$, respectively. The orange dashed lines indicate where the baseline of each injection response is taken.

3.5 Results and Discussion

3.5.1 AFM Imaging

In this study, we employed AFM imaging for two main purposes: first, to verify membrane formation on the LSPR sensor, thereby confirming that the amyloid interactions in LSPR were with the membrane and not the GNPs on the sensor; second, to capture images of the lipid membrane before and after amyloid-membrane interaction for illustration. To demonstrate membrane formation on the LSPR sensor, we compared the image of a new sensor with the image of an membrane-covered sensor. We also imaged pure lipid membrane

on mica for reference.

Figure 3.4 presents AFM images of all surfaces involved in the LSPR experiments, and Table 3.2 shows surface roughness and average height difference (Δh) between the highest and the lowest points in each image. Figure 3.4A displays the surface structure of an LSPR sensor covered by a layer of GNPs. The GNPs are closely packed and entirely covering the glass chip, forming the sensing surface with a large surface roughness of 16.53 nm. The surface is a continuous sheet of GNPs with height difference $\Delta h = 73.06 \pm 12.23$ nm. Figure 3.4B shows the AFM topography image of the healthy model (HM) membrane supported on an atomically flat mica slide. The surface of the HM membrane is smooth, but not completely flat, showing numerous higher and lower surface defects called domains, which originate from phase separation of the various lipids. These domains form due to the nature of the various lipid molecules that constitute our membranes, and which have different chain length and head group sizes. The surface roughness of the HM membrane on mica is 225.95 pm, with $\Delta h = 1.11 \pm 0.12$ nm, which is significantly smoother than the surface of the GNP-covered chip. In comparison to the GNP surface, the membrane is significantly smoother. In the LSPR experiments, a layer of membrane is formed on top of the GNP sensor, as illustrated in Figure 3.2. The AFM image of the HM membrane deposited on GNP is shown in Figure 3.4C. As the GNP structures are much larger in Δh and surface roughness, the fine features of the membrane domains become invisible. Compared to the GNP surface, the roughness of the GNP surface covered by the HM membrane is reduced from 16.53 nm to 573 pm, and the Δh also drops significantly to 2.52 $\pm$ 0.28 nm. This indicates that a continuous stable sheet of lipid membrane has formed over the rough GNP surface, demonstrating that the injection of liposome solution into the LSPR fluidic cell creates a complete coverage of the membrane on the sensor.

To illustrate and confirm the amyloid binding to the membranes, Figure 3.5 shows representative AFM topography images demonstrating amyloid binding to the membrane in the same concentration as in LSPR experiments. The AFM topography images of the early diseased model (EDM) membrane supported on mica were collected before and after adding amyloid to the AFM liquid cell for a bulk concentration of 50 μM, achieving the same amyloid level as in the LSPR experiments. The images with amyloid interacting with the lipid membrane were collected at 60, 90, 120, and 180 minutes after adding amyloid.

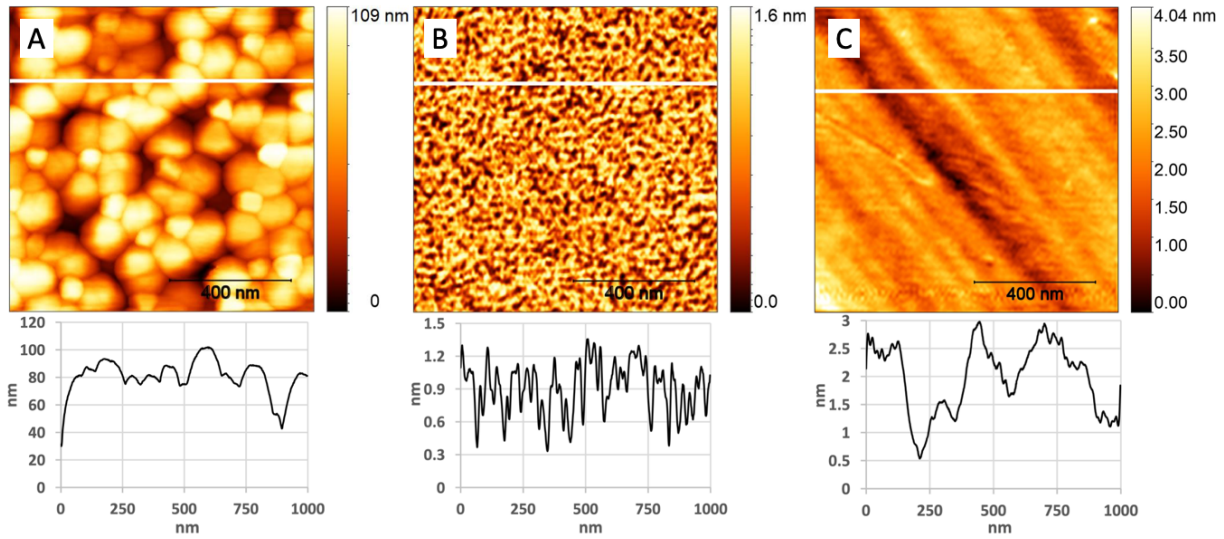


Figure 3.4: **AFM Topography Images** of (A) an LSPR sensor surface covered with GNPs, (B) a supported healthy model (HM) membrane formed on mica, and (C) the HM membrane supported on the GNP covered LSPR sensor. Each image size is 1 μm $\times$ 1 μm. The cross-section plot below each image shows the height profile along the white line on the AFM image.

Figure 3.5 displays the sequential changes caused by amyloid interactions with the EDM membrane over time. Before adding amyloid, as shown in Figure 3.5A, the imaged surface is relatively flat, but with small height variations displayed as brighter or darker regions in the image, indicating the presence of small domains distributed on the surface. The largest height difference of the features is within the 1-2 nanometer range. Figure 3.5B shows the image taken at the same scale after incubating the membrane with amyloid for 60 minutes. The image reveals amyloid-induced surface indentations with a distinct height difference (2-3 nanometers) relative to the surrounding area. Further images focusing on a smaller area covering the apparent damage reveal evidence of amyloid accumulation over time. Figure 3.5C (60 minutes) shows lipid loss, which produces defects (holes) in the membrane near the bottom of the image. The darker (lower) area is not a smooth plane; it has many clusters that stand up to the same height as the surrounding taller region. These clusters start to grow larger and taller over time, suggesting amyloid-lipid complex clustering when amyloid damages the membrane. Simultaneously, amyloid aggregates attached to the edge

	[A] LSPR Sensor	[B] Membrane on Mica	[C] Membrane on Sensor
Roughness	16.53 nm	225.95 pm	573 pm
Δh	73.06 ± 12.23 nm	1.11 ± 0.12 nm	2.52 ± 0.28 nm

Table 3.2: **Roughness and Height Difference (Δh) for the AFM Images Shown in Figure 3.4.** Roughness was calculated by built-in statistical functions in GWYDDION software [4], which is computed from the second central moment of data values. The average Δh is calculated from the difference between the minimum and maximum values of the image, also using the functions from GWYDDION [4].

of the induced domains continue to grow. Figure 3.5D displays an image taken at 180 minutes when the sporadic spots of aggregates finally link together. This set of AFM images clearly demonstrates that amyloid binds to the lipid membrane and induces visible damage to the membrane integrity at a concentration of 50 μM.

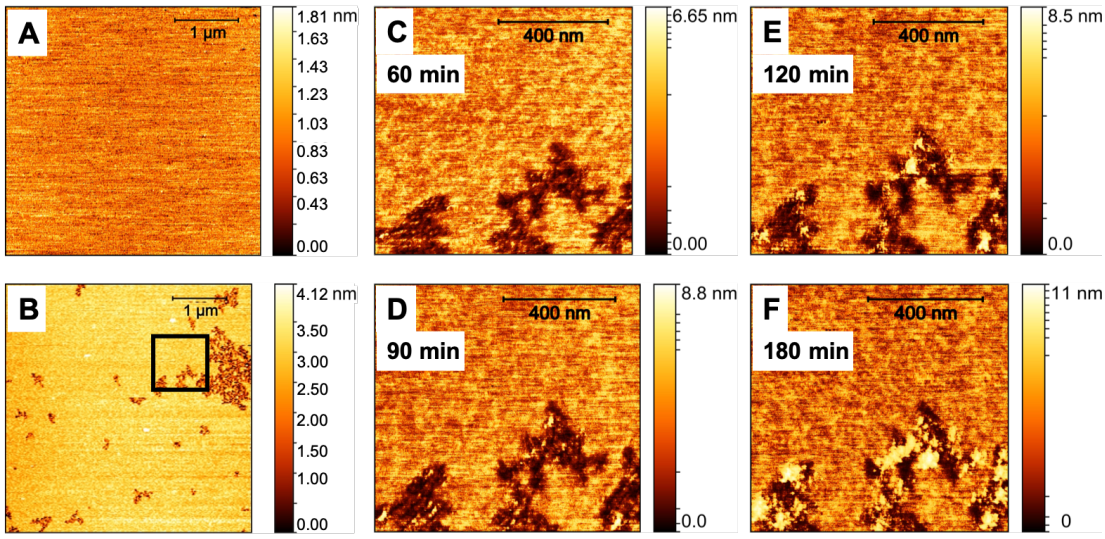


Figure 3.5: **AFM Topography Images of Supported Early Diseased Model (EDM) Membranes on Mica with and without Amyloid.** [A] untreated EDM membrane and [B] treated with 50 μM amyloid for 60 minutes. Images [C] to [F] are enlarged images of the black square area shown in [B] after amyloid treatment of 60 minutes, 90 minutes, 120 minutes and 180 minutes.

3.5.2 LSPR Results

Calibration of the GNP sensor was accomplished with standard glucose solutions at concentrations of 5%, 10%, 15%, 20%, 30%, 40%, 50% to ensure successful recording of the SPR shift ($\Delta\lambda$). The measured response $\Delta\lambda$ was plotted against the refractive index change Δn between the glucose solution and the deionized water ($n = 1.33$). The slope of the trend line for each plot was then extracted and averaged among the five repeats based on Equation 3.2, giving the value of the sensitivity factor. In the end, the sensitivity factor of the GNP sensor was determined to be $m = 107.99 \pm 1.95$. Then m can be substituted into Equations (3.4) to calculate for $\frac{d_{mem}}{l_d}$ and $\frac{d_{A\beta}}{l_d}$, which are represented as T_{mem} and $T_{A\beta}$ according to Equation (3.5), respectively.

As shown in Figure 3.6 and Part 1 of Table 3.3, the thickness of the membrane varies between models, with the thinnest membrane ($T_{mem} = 0.068 \pm 0.010$) found in the healthy

model (HM) and the thickest in the late diseased model (LDM) ($T_{mem} = 0.088 \pm 0.008$). The average membrane thickness for each membrane model is reduced when melatonin is present in the buffer, with the most significant decrease observed in the LDM ($T_{mem} = 0.071 \pm 0.004$). The reduction in membrane thickness caused by the incorporation of melatonin into the HM and the early diseased model (EDM) is insignificant, indicating limited fluidity changes of the membranes induced by melatonin. The substantial reduction in membrane thickness due to melatonin in the LDM suggests that fluidity enhancement is the greatest among all three lipid models.

These varying levels of thickness profile changes might be attributed to the differing effects of melatonin on spacing lipid molecules apart, depending on the lipid species. The average area for lipids with lipid head groups is 64 $\mathring{A}^2$ [180], while the average area of the GM1 head group is approximately 192 $\mathring{A}^2$ [181], triple the size of the PC head groups. Consequently, the effect of melatonin in expanding the distance between the head groups of the PC group lipid molecules is relatively larger compared to GM1. As a result, the lipid tails of DPPC and POPC exhibit more flexibility due to melatonin incorporation, causing the entire membrane to reduce its thickness. The LDM, which contains the highest proportion of DPPC and POPC among all three lipid models, experiences the most significant reduction in membrane thickness.

Figure 3.7 displays the distribution of thickness profile T of the amyloid layer on the top of three lipid models, with the corresponding values provided in Part 2 of Table 3.3. For the control groups of all membrane models, the thickest amyloid layer build-up is observed in the EDM membrane ($T_{A\beta} = 0.014 \pm 0.001$), followed by the HM membrane ($T_{A\beta} = 0.008 \pm 0.0005$), while the LDM membrane exhibits the thinnest amyloid layer formation ($T_{A\beta} = 0.004 \pm 0.0005$). The presence of melatonin in the buffer decreases the thickness of the amyloid layer on both the HM and EDM membranes, with the most significant effect ($p = 0.003$) on the EDM resulting in approximately a 40% reduction in amyloid layer thickness ($T_{A\beta} = 0.008 \pm 0.0009$). For the HM membrane, a decrease of amyloid layer thickness was observed, yet not significant. In contrast, the addition of melatonin substantially increases the amyloid layer thickness on the LDM membrane ($p = 0.008$) resulting in approximately a 40% thickness change ($T_{A\beta} = 0.006 \pm 0.0004$). These observations demonstrate that the presence of melatonin reduces the binding of amyloid

Lipid Models	HM	EDM	LDM
Part 1. Thickness Profile T_{mem} - Lipid Membrane			
Control	0.068 ± 0.010	0.080 ± 0.006	0.088 ± 0.008
W. Melatonin	0.076 ± 0.012	0.080 ± 0.008	0.071 ± 0.004
p-value	0.602	0.987	0.056
Part 2. Thickness Profile $T_{A\beta}$ - Adsorbed Amyloid Layer			
Control	0.008 ± 0.0005	0.014 ± 0.001	0.004 ± 0.0005
W. Melatonin	0.007 ± 0.001	0.008 ± 0.0009	0.006 ± 0.0004
p-value	0.772	* 0.003	* 0.008
Part 3. $T_{A\beta}/T_{mem}$			
Control	0.172 ± 0.042	0.181 ± 0.0220	0.046 ± 0.004
W. Melatonin	0.090 ± 0.013	0.100 ± 0.007	0.084 ± 0.006
p-value	0.1299	* 0.0036	* 0.00002

* p-value < 0.05

Table 3.3: **The Thicknesses Profiles of Lipid Membrane Models (T_{mem}) and Adsorbed Amyloid Layers ($T_{A\beta}$) with and without Melatonin.** This table shows the thicknesses of each layer calculated from LSPR response using Equation (3.4) for each membrane model. The thickness values are divided by the evanescent field decay length l_d, denoted as a dimensionless parameter T as the thickness profile [see Equation (3.5)], and the table is divided into three parts. Part 1 and Part 2 show T of the membrane (T_{mem}) and adsorbed amyloid ($T_{A\beta}$) layer, respectively. Part 3 shows the ratio of amyloid layer thickness to the membrane thickness $T_{A\beta}/T_{mem}$. The table includes the thickness or ratio results of the control group (without melatonin) and the melatonin group (with 400 μM melatonin).

to the HM and EDM membranes. However, for the LDM membrane, the opposite effect is observed, with melatonin increasing the adsorbed layer thickness.

Before delving into the details of the results, it is crucial to note that amyloid interacts with membranes in multiple ways, including attaching or inserting into the membranes and behaving like a surface surfactant that disrupts the lipid layer and uptakes some lipid molecules [139]. The size of Aβ oligomers, ranging from 2 to 6 nm, is comparable to the

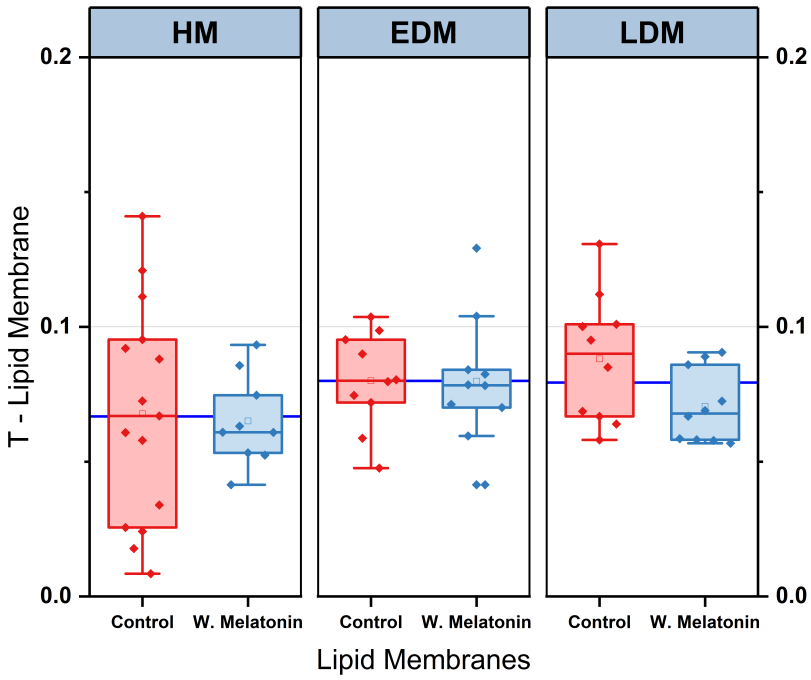


Figure 3.6: **Lipid Membrane Thickness Profiles** (T_{mem}) of HM, EDM, and LDM membranes (from left to right). The vertical axis is unitless because the membrane thickness and l_d are both in nanometer units. The red bars show the control group while the blue bars show the experimental group treated with 400 μM melatonin.

lipid membrane thickness [182, 183]. However, because of various types of Aβ-membrane interactions, the amyloid layer on the membrane is not continuous or uniform, thus the thickness profile T that we are discussing is indeed dependent on the effective thickness of the bound amyloid.

The results indicate that amyloid interacts more strongly with the EDM membrane than with HM or LDM membranes. This suggest thatneuronal membrane at early stages of AD may be more suseptible to amyloid damage. As membranes progress to the late diseased phase, the degree of amyloid insertion or membrane adsorption is reduced, resulting in the thinnest amyloid layer on the LDM membrane. From this perspective, the amyloid-

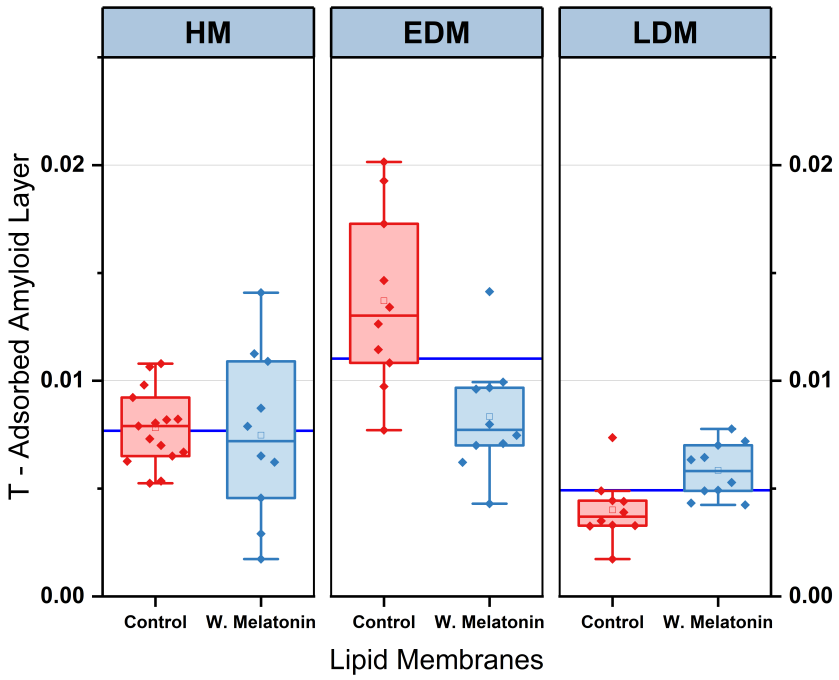


Figure 3.7: **Adsorbed Amyloid Layer Thickness Profiles** ($T_{A\beta}$) on HM, EDM, and LDM membranes (from left to right). The vertical axis is unitless because the membrane thickness and l_d are both in nanometer units. The red bars show the control group while blue bars show the experimental group treated with 400 μM melatonin.

membrane interaction depends on the diseased state of the cellular membrane, with the EDM being most susceptible to damage, followed by the HM and LDM. This finding aligns with an AFM study previously reported by Drolle *et al.* [2].

Furthermore, our results indicate that melatonin protect the EDM membrane more efficiently than the HM and LDM membranes. This indicates that the presence of melatonin in the EDM membranes significantly alters the surface structure of the membrane, thereby reduces the affinity of Aβ to the surface, protecting this membrane most effectively. Melatonin potentially acts as a mediator between the lipid head groups, diminishing the roughness of the membrane. Figure 3.7 and Table 2 Part 3 demonstrate that the presence

of melatonin leads to a decrease in the amyloid layer thickness on EDM membranes, an increase in thickness on LDM membranes, and relatively constant thickness on HM membranes. These more convergent amyloid layer thicknesses suggest that melatonin tends to induce similar surface properties in neuronal membranes with different diseased states. This effect of melatonin is likely due to the interaction of melatonin with the membrane lipids and changing the membrane properties. The fluidizing properties of melatonin, which eliminate the structural differences among all models, as discussed earlier [44, 51, 53], could be one of the reasons. Notably, the fluidizing effect is most prominent in the EDM model.

Figure 3.8 and Table 3.3 part 3 display the results of the amyloid thickness divided by the membrane thickness, which is equivalent to dividing the amyloid response by the membrane response. In LSPR experiments, one GNP sensor was only used once for data collection; however, the sensitivity factor of each sensor would differ slightly. This quotient eliminates the small uncertainty of the results introduced by the varying sensor sensitivities. Figure 3.8 confirms that the relative distribution of amyloid layer thicknesses remains consistent across all lipid models, as depicted in Figure 3.7. Among the three models, the EDM membrane is most likely to be damaged by amyloid, while melatonin contributes to the most significant reduction in amyloid layer build-up. Conversely, the presence of melatonin leads to increased amyloid layer formation on LDM membranes, although the amount of amyloid binding is lowest in the absence of melatonin. In the case of HM membranes, the difference between the control group and the melatonin group is not statistically significant ($p = 0.1299$). Combining these results with the previously discussed findings on T_{mem} and $T_{A\beta}$, it becomes evident that the difference in amyloid layer build-up due to melatonin's effect is the most significant for both diseased models, while its effect on HM is negligible. Melatonin protects the EDM membrane from amyloid binding but promotes the amyloid accumulation on the LDM membrane.

3.6 Conclusion

We studied interaction of Aβ (1-42) with model membranes mimicking neuronal membranes in healthy (HM), early diseased (EDM) and late diseased (LDM) states and determined the

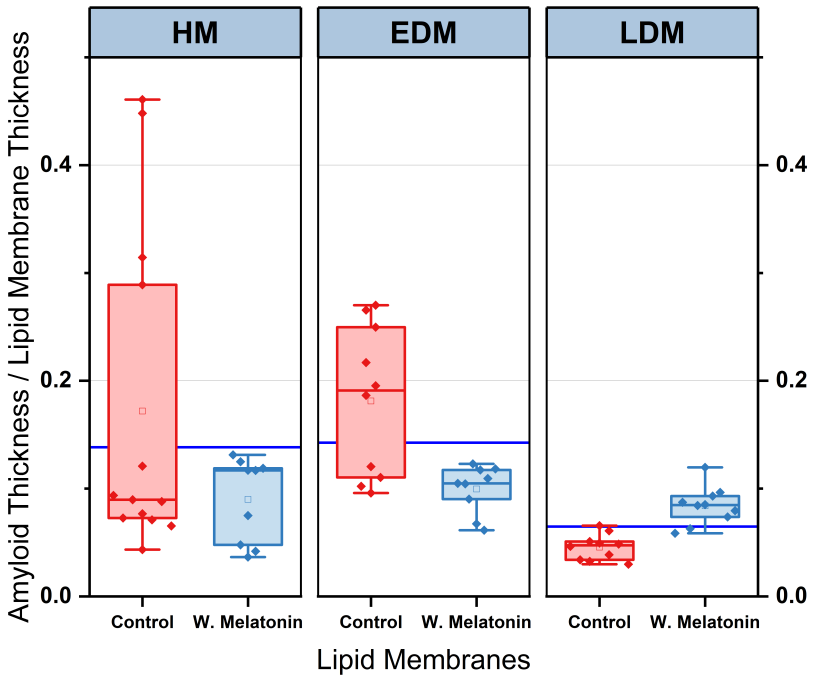


Figure 3.8: $T_{mem}/T_{A\beta}$ **of HM, EDM, and LDM membranes** (from left to right). Red bars show the control group, and blue bars show the experimental group treated with 400 μM melatonin.

effect of melatonin on these non-specific interactions utilizing AFM and LSPR. The study demonstrated that amyloid interactions with membrane models depend on the disease states of the models, with the EDM membrane being affected the most significantly. It also revealed that melatonin inhibits amyloid-membrane interactions of the three lipid models, but this protective effect was the most pronounced in the EDM membranes. Interestingly, melatonin has an opposite effect on the LDM, slightly promoting amyloid-membrane interaction in the LDM. The results suggest that melatonin may inhibit amyloid toxicity in the early stages of AD, but this effect diminishes in the late stages as the disease advances.

Chapter 4

Melatonin Affects Membrane Permeability Changes Caused by Amyloid-Membrane Interaction: A Black Lipid Membrane Study

4.1 Overview

4.1.1 Summary of the Work

Building upon knowledge from the LSPR Chapter 3 where amyloid was shown to interact with model lipid membranes by accumulating layers and increasing the effective thickness, the effect of melatonin in reducing lipid bilayer thickness and preventing amyloid buildup was also noted. While LSPR could only observe the build-up of amyloid layers on the membrane surface, details on amyloid damage behaviours were not fully revealed.

For the work reported in this chapter, I used the BLM technique to examine the amyloid-membrane interaction more closely. The focus of this study was two parts: 1. To identify the various forms of damage that amyloid species do on the lipid membrane,

and 2. To classify how melatonin influences each type of amyloid-induced damage.

The experimental design consisted of three groups: 1. a control group without melatonin, 2. a group with 50μM melatonin, and 3. a group with 100μM melatonin. The expectation was that distinct ion current signals would be discernible among these three groups. A simple neuronal model composed of DPPC, POPC, and cholesterol served as the lipid system, chosen for its suitability in forming a complete lipid membrane on the BLM instrument and its prior characterization in NMR studies discussed in Chapter 2.

From this study, I learned that melatonin's presence introduce greater fluctuations in current measurements, increases membrane conductance and ion permeability, and decreases rupture likelihood, all indicative of its ability to fluidize the membrane. Melatonin-enriched membranes exhibits stable pore formation, maintaining integrity despite amyloid damage. My findings reveal that melatonin does not significantly affect the overall quantity of amyloid interaction events, but alters their nature, reducing insertions from small oligomers while promoting stable pore/channel formation from larger aggregates. Moreover, melatonin appears to extend membrane lifespan under amyloid interaction and minimize rupture risk.

4.1.2 Contributions

This work was fully developed and designed by me. My colleagues Carina Filice and Yue Xu offered instrument training and provided insights on data analysis. The undergraduate student, Gexu Liu, assisted with initial data collection and preliminary data analysis. I independently accomplished the major data collection and statistical analysis, as well as the writing of this chapter.

4.1.3 Challenges and Future Directions

The experimental process and subsequent data analysis presented several inevitable challenges. Firstly, the success of forming a membrane was not guaranteed in each individual experiment. Numerous attempts at crafting the lipid membrane were often necessary, and

the experiment would be stopped if success was not achieved within five tries. Secondly, the introduction of the amyloid solution into the bath required precise and gentle handling; any abrupt movement or vigorous liquid flow could lead to membrane rupture. A third challenge arose from the study's original design, which included melatonin buffer with concentration of 400 μM (saturated). Unfortunately, all attempts with this concentration produced extremely noisy signals, leading to the group's abandonment. This problem could have stemmed from the melatonin interacting too actively with the membrane, causing fluctuations. Alternatively, the melatonin might have excessively fluidized the membrane, resulting in inherent instability. Either situation could produce substantial noise in the current recordings, rendering the amyloid interaction undetectable. Lastly, data analysis was labor-intensive in order to count and distinguish different amyloid-membrane interaction events. Extracting these occurrences individually proved to be a time-consuming task, adding to the complexity of the study.

The experimental protocol for BLM is well-defined. Before selecting the lipid membrane model for use in BLM, it is necessary to check the stability of the assembled membranes. If the membrane is challenging to paint onto the hole, or if it cannot endure the length of an experiment, alternative solutions must be explored. This could be achieved either by modifying the membrane composition or changing the solvent of the lipid solutions. For future research involving melatonin, it would be advisable to keep the concentration in the bath unsaturated to prevent noisy signals. One potential direction for a follow-up study could involve varying the amyloid concentration in the bath, allowing researchers to understand how amyloid concentration might influence the type of damage to the lipid membrane.

4.2 Introduction

Alzheimer's disease (AD) is a multifactorial progressive neurodegenerative disorder affecting neuron cells in the brain, ultimately leading to cell degeneration and death [8, 145]. Common symptoms of AD include progressive cognitive impairment and memory loss through aging. It is characterized by the accumulation of extracellular amyloid-β (Aβ) plaques, intracellular neurofibrillary tangles, and chronic inflammation, which collectively contribute to synaptic disfunction and neuronal death [11, 184]. A prominent hypothesis regarding AD's pathogenesis is the Amyloid Hypothesis, which posits that the neurodegeneration observed in AD is primarily triggered by the abnormal accumulation of Aβ peptides in the brain [10, 185]. Numerous clinical and cellular studies have been done in order to find prevention or cures to AD by targeting the amyloid species [45]. Aβ peptides were shown to be able to interact with the lipid membranes non-specifically, resulting in the formation of pores and ion-channels upon the peptides' integration into the membrane, or alternatively, they can induce the removal of lipid molecules from the surface of the membrane[186, 187]. The intricate nature of amyloid-membrane interaction has given rise to various models to articulate the resultant membrane damage. These models span a spectrum of phenomena, ranging from random membrane disruption to the formation of stable, barrel-structured ion channels [188]. Building on these models, all types of interactions play a significant role in shaping the results observed in the presented study. They are carefully analyzed and evaluated to deepen our understanding of the membrane damage instigated by amyloid toxicity, providing a comprehensive perspective on this complex biological phenomenon.

As the amyloid toxicity to the membrane is achieved via structural damage, alternating the properties of membrane may have potential benefits in reducing the toxic effect. The lipid membrane, an essential component of all human cells, functions as both a crucial barrier and a communication interface between the cell and its surrounding environment [189]. Comprising a bilayer structure, the membrane consists of lipid molecules with hydrophilic headgroups oriented outward and hydrophobic tailgroups embedded within the bilayer. The preservation of this membrane's integrity is vital for the proper functioning of the cell, and any disruption in its structure can have serious consequences, including

cell death [23]. This insight into the membrane's complex structure highlights its essential role in cellular health and provides a basis for exploring therapeutic approaches that focus on maintaining membrane stability, especially in response to the toxic effects of amyloid species.

Melatonin is a small hormone molecule that easily partitions into the head group region of lipid membranes [146]. Despite the instances of melatonin's protective role against AD symptoms [49, 190] as well as amyloid toxicity [47, 48], the molecular mechanisms underlying this property remains unclear. In the present study, we propose a mechanism through which melatonin may guard against amyloid's toxicity to lipid membranes. This mechanism involves melatonin's ability to modify the physical properties of the bilayer, thereby inhibiting amyloid damage resulting from non-specific interaction. Previous research on melatonin's interaction with dipalmitoyl phospholipid and models incorporating such lipids has demonstrated a fluidizing effect on the lipid membrane. Specifically, melatonin has been shown to enhance membrane dynamics and expand the area of lipids [3, 51, 146].

It has been shown that melatonin alters the membrane physical properties by fluidizing the membrane or altering phase separation in model membranes, with the effect is more complex in multi-component membrane as compared to single component membrane [53, 52]. These properties of membrane are important to consider in studying Aβ-membrane interactions. In the current study, we explored the effect of melatonin partition into DPPC/POPC/cholesterol and its interaction with Aβ (1-42).

In order to investigate the changes in membrane permeability resulting from amyloid-membrane interaction and melatonin's effect towards it, we employed the BLM experimental technique. The BLM method is a well-established approach for studying membrane dynamics, owing to its ability to mimic biological membranes closely [191]. BLM structure has been extensively used for its electrical properties and has been widely applied in biosensing field, including protein-membrane interaction and ion channel measurements. The BLM is not only capable of acting as a media to immobilize proteins of interest, but also can be used as a study object when its composition changes. Drolle *et al.* reported a BLM study carried out on a complex neuronal membrane models mimicking different AD disease states, and found the average current induced by amyloid-membrane interaction was higher in the diseased models compared to the healthy model (HM) [2]. Further,

Lee *et al.* reported that Aβ (1-42) was able to form ion channels on membranes formed with brain total lipid extracts, and the ion channel behaviour differed from the synthetic model membranes composed with DOPS and POPE [192]. In this study, I specifically utilized BLMs to simulate the conditions of cellular membranes under the influence of both melatonin and amyloid. This approach allowed me to monitor and measure the alterations in the permeability of these simulated membranes. The results of my investigation have the potential to offer significant insights into the role of melatonin in mitigating the neurotoxic effects of amyloid, thereby contributing to our understanding of AD, where amyloid-induced neurotoxicity is a major factor.

4.3 Materials and Method

4.3.1 Lipid Membrane and Amyloid

The chemicals used in this study, including DPPC, POPC, cholesterol, and melatonin, were purchased from Sigma-Aldrich and were utilized as received without any further purification. Stock solutions of DPPC, POPC, and cholesterol were prepared at a concentration of 10 mg/mL using chloroform and were stored at -20 $^{\circ}C$. The model lipid was prepared at a molar ratio of DPPC:POPC:cholesterol = 3:3:2. The stock solutions were mixed, dried under a gentle flow of nitrogen, and subsequently resuspended in a mixture of N-decane and butylalcohol (ratio 50:1) to achieve a final lipid concentration of 10 mg/mL.

For all BLM experiments, a buffer containing 150 mM KCl and 20 mM HEPES was used. Melatonin solutions at concentrations of 50 μM and 100 μM were prepared by dissolving melatonin film in the buffer and sonicating for 30 minutes. The melatonin film was obtained by evaporating a melatonin-ethanol stock solution. After sonication, the melatonin buffers were filtered and stored in the fridge.

The Aβ (1-42) peptide was purchased from rPeptide and aliquoted following the HFIP protocol [159]. Before use, the Aβ aliquot was thawed and resuspended in the buffer, either with or without melatonin, following 10 minutes of sonication. The prepared amyloid solution was then directly added to the BLM system to achieve a final concentration of 5

μM in the bath.

4.3.2 Black Lipid Membrane

BLMs are useful in characterizing the electrical properties of lipid membranes due to the high sensitivity to changes on their conductivity, dielectric constant or surface charges [74, 191, 193]. BLM originally describes an invisibly thin, stable and electrically isolated lipid membrane that is formed in aqueous environment. This layer of lipid membrane appears grey-dark in monochromatic light due to the destructive interference of the reflected light from the water/lipid and lipid/water interfaces. As shown in Figure 4.1, the membrane serves as an insulating barrier between two electrolyte solutions, and the membrane integrity can be monitored through electrical measurements. Therefore, the BLM technique enables the investigation of membrane permeability by tracking ion transport across the membrane. By applying a voltage bias across the membrane and monitoring the resulting current, one can gain insight into the transport of charged particles through the membrane.

In BLM experiments conducted for the current study, both sides of the Teflon barrier are filled with 1 mL of buffer solution to ensure equal liquid height. A voltage bias of 50 mV is then applied to the bath via two electrodes inserted on each side of the barrier. The vertical lipid membrane spreading across the hole on Teflon barrier is created by directly applying the organic solution of the lipid mixture to the hole with a pipette tip. Painting the lipid-containing organic solvent onto the hole results in a thin film with a colorful reflection observable through a microscope. This color gradually fades, giving way to a dark spot in the center, until a single layer lipid membrane is formed in the center.

Figure 4.2 shows a representative BLM trial. Upon successful formation of the lipid membrane at 50 mV, the system is allowed to run for 15 minutes to stabilize the membrane. Then, the amyloid solution is injected into the bath on one side of the Teflon barrier to achieve a final concentration of 5 μM. Recordings from this point are then utilized for data analysis. The system is subsequently left to incubate for 15 minutes with the amyloid at 50 mV. After incubation, the applied bias is increased to 90 mV for an additional 15 minutes. The voltages are then sequentially adjusted to 100 mV, 110 mV, and 120 mV,

with a recording duration of 5 minutes at each voltage level. Details of the analysis on the current signal are discussed in Section .

The study involved three groups: a control group with no melatonin in the buffer, and two experimental groups with 50 μM and 100 μM melatonin dissolved in the buffer. Each group underwent at least 20 individual experiments.

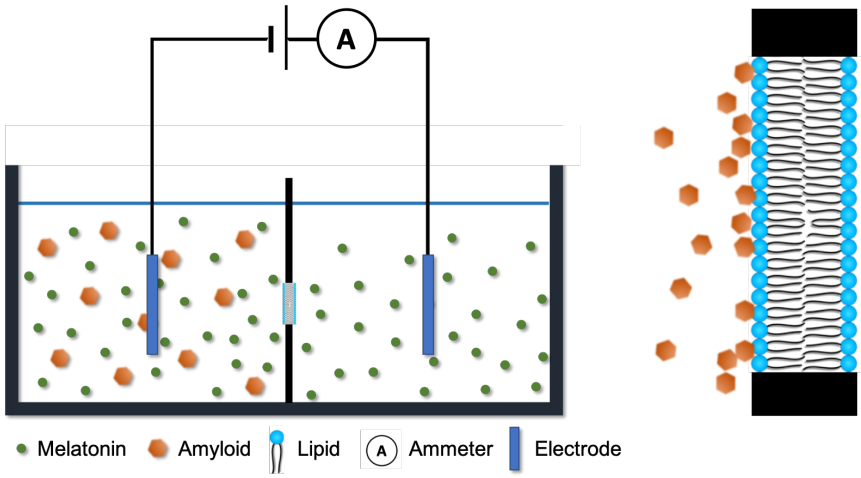


Figure 4.1: **An Illustration of the BLM Experiment Setup**. The same amount of solution was added to both side of the Teflon barrier. A pair of electrodes, connected to a voltage bias, was placed inside the solution on each side of the barrier. Amyloid was injected on only one side of the barrier and interact with the lipid membrane that spreads across the central hole on the Teflon barrier. A closer view of this interaction is shown on the right of the figure. The ammeter records the current throughout an experiment.

4.3.3 BLM Signal Category

Figure 4.3 illustrates the complex interaction between Aβ oligomers/aggregates and the lipid membrane, outlining a progressive sequence of events leading to membrane disruption. Initially, individual Aβ oligomers penetrate the tail region of the membrane, followed by small aggregates that accumulate on the surface, creating indentations. As the aggregates grow, they disrupt the membrane's continuity, forming either stable ion channels or less

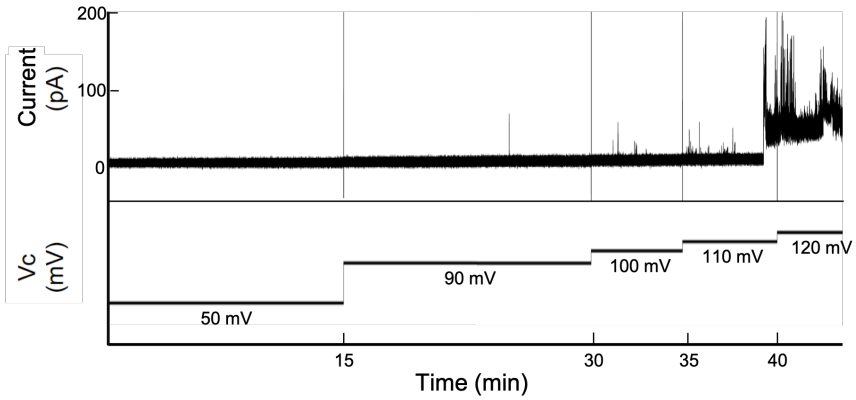


Figure 4.2: **Representative BLM Trial Plot.** The recorded current and the applied voltage are plotted versus time (min). Amyloid was introduced to the bath at 50 mV, incubated for 15 minutes, and then measured for 15 minutes at 90 mV. This was followed by measurements at incremented voltages of 100, 110, and 120 mV, each for 5 minutes. There are multiple types of signals included in this example, and the detailed explanations are provided in the BLM Signal Category section.

stable pores. This leads to advanced damage characterized by increased lipid loss, culminating in hole formation and, ultimately, membrane rupture. Given the various potential pathways for amyloid-membrane interaction, multiple signal patterns may appear during a BLM trial. Consequently, these signals need to be categorized according to their structural characteristics, which represent distinct types of amyloid-membrane interaction. We classified the amyloid event signals observed in the BLM recordings according to the models proposed by Saigo *et al.*, including step signals, multilevel signals, erratic signals, and spike signals [188]. We introduced one more type as instability signals where the overlapping of multiple signals occurs. The subsequent list and figures provide a detailed description of these signal models, which served as a guide throughout our data analysis process.

Spike signal As shown in Figure 4.4, spike events are short-lived, pronounced peaks on the positive current side of a trial, lasting shorter than 10 milliseconds. Simultaneous positive and negative signals are classified as noise instead of spikes. The origin of a spike signal may arise from either the membrane insertion of individual oligomers or membrane

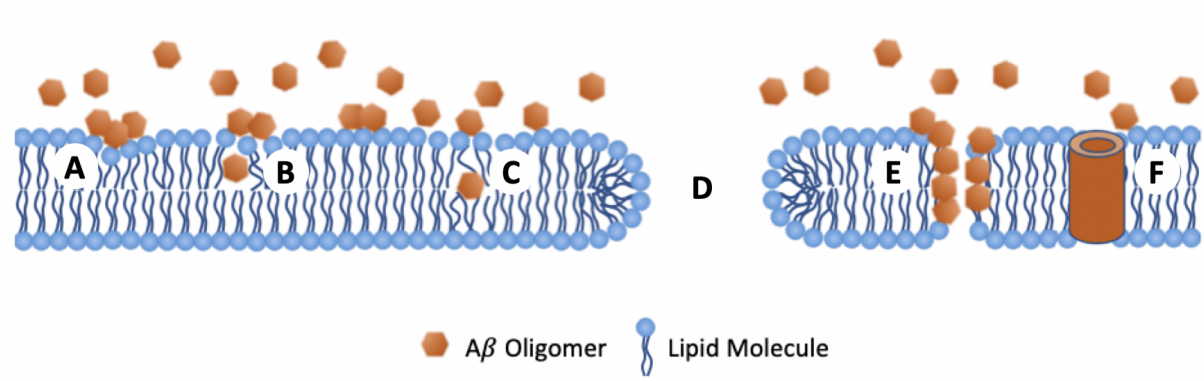


Figure 4.3: **Schematic of the Interaction between Aβ Oligomers/Aggregates and the Lipid membrane**: Individual oligomers can penetrate into the tail region of the membrane (C), while small aggregates may accumulate on the membrane surface (A), creating indentations (B). As the aggregates grow to larger sizes, they can disrupt membrane continuity, forming either stable ion channels with cylindrical structure (F)) or less stable pores (E). This process can lead to increased lipid loss, contributing to further damage. Over time, this can result in hole formation (D) and, ultimately, membrane rupture.

indentation caused by larger amyloid aggregates. Such interactions manifest as rapid fluctuations on the membrane. Following these interactions, amyloid oligomers or aggregates may either remain affixed to the lipid membrane or reintegrate into the buffer solution. Importantly, these spikes do not signify structural membrane damage and are therefore not factored into average current calculations for an experimental trial. When counting spikes, clusters of adjacent peaks, whether of similar or varied height, are considered a single event as long as the duration does not exceed three seconds.

Instability signal When multiple amyloid-membrane interactions, specifically the insertion and indentation events described in the previous section, occur simultaneously, they can generate concurrent or overlapping spike events. As illustrated in Figure 4.5, these simultaneous occurrences can be challenging to distinguish and characterize. Therefore, those accumulated events are classified as instabilities. Another key feature of instability is observable baseline fluctuations during a trial. The presence of instabilities signifies persistent amyloid interaction with the membrane surface, increasing the probability of re-

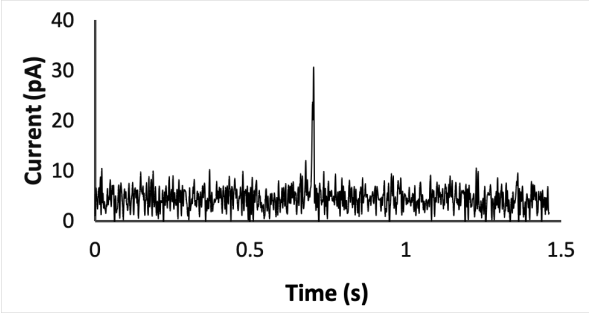


Figure 4.4: **A Sample Spike Signal.** The spike signal occurs at time (t) = 0.7 s and lasts for approximately 6 ms, with a peak current at 30 pA.

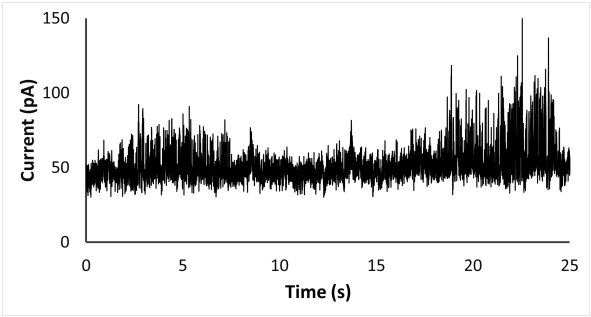


Figure 4.5: **Sample Instability Signals.** Signals between time (t) = 0 s to 8 s and between 17 s to 25 s are the major instabilities where numerous spike signals overlap. The signal between these two major instabilities has an unstable baseline.

sultant structural damage. Hence, instabilities often persist for extended periods or recur multiple times without clear start or end points, possibly spanning the entire trial. When counting for instabilities, the presence of at least one instability event in a trial is denoted by "1", while an absence of instabilities is represented by "0".

Step signal When there is a sharp, distinct elevation from the baseline in the current, it manifests as a step structure in the signal, typically persisting for more than 10 seconds. This suggests the formation of a stable, circular pore, as a consequence of amyloid self-aggregation (see Figure 4.3). Occasionally, the step can persist throughout the entire trace without returning to the baseline, indicating a stable ion-channel formation. In contrast, the step signal may return to the original baseline in some instances, indicating closure of the ion channel, most likely due to pore clogging from further amyloid aggregation. When multiple pores or channels are present, their closures might not occur simultaneously. The signal may exhibit a partial decline, reaching an intermediary plateau positioned between the step signal and the original baseline. In terms of event quantification, these step structures are individually calculated for separate average currents. It is important to note that other events may occur concurrently within a step, and these are also accounted for as separate events in the event count. Figure 4.6 shows a representative step signal that

has multiple other events including spikes and instabilities. The step appears at t = 3 s, where the current elevates from close to 0 pA to approximately 80 pA. At t = 12 s, the signal recedes to around 50 pA without entirely reverting to the original baseline. Hence, this particular step signal signifies the formation of multiple pores and channels at t = 3 s and a partial closure of the channels at t = 12 s.

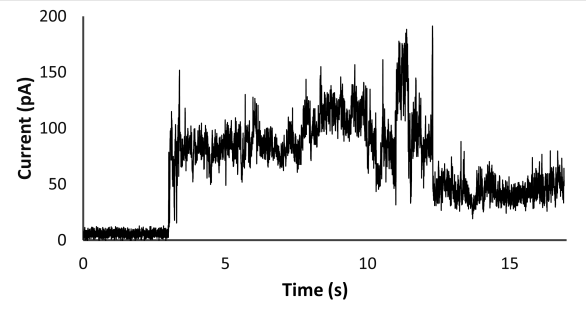


Figure 4.6: **A Sample Step Signal.** Current elevates at t = 3 s. Then the current reduces at t = 12 s to a new baseline which is higher than the original baseline before the step occurs.

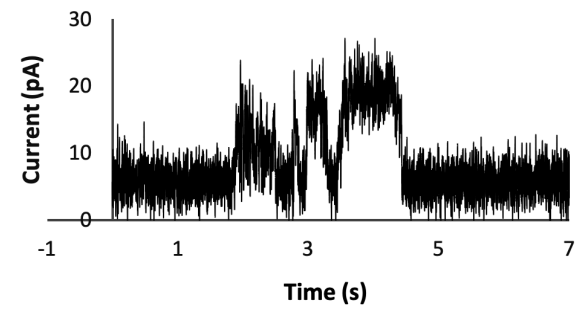


Figure 4.7: **Sample Multilevel Signals.** There are three consecutive multilevel signals that occur, during t = 2 s to 2.8 s, 2.8 s to 3.5 s and 3.5 s to 4.5 s.

Multilevel signal Multilevel signals are shown in Figure 4.7. They have the same sharp edge structure as the step signals but they are shorter than 10 seconds. These signals can either be isolated incidents or occur as part of a closely connected sequence. This pattern suggests that the amyloid peptide has successfully combined with the lipid, but not in sufficient quantities to form channels with a stable structure. An illustration of this structure is present in Figure 4.3, where multiple amyloid aggregates attach to the tail region of the lipids and create a transmembrane pore. These pores or amyloid-lipid clusters are highly dynamic, with the ability to actively modify their structure. Consequently, ions in the buffer can only travel through the pore when the structure is compatible, creating a temporary current above the baseline until the pore undergoes another fluctuation. Each multilevel event is individually counted, but they are not differentiated when calculating the average current for each voltage level.

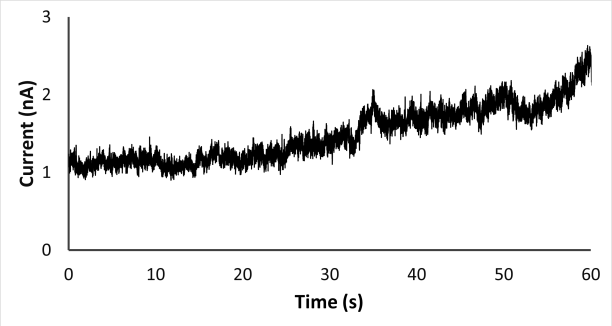


Figure 4.8: **A Sample Erratic Signal.** The current is over 1 nA and keep increasing without a stable baseline.

Erratic signal Figure 4.8 shows the BLM trial of an erratic signal. These signals do not have a clear baseline. Their strength fluctuates unpredictably, displaying a non-uniform shape, and the signal structures undergo varying changes over time. Such erratic behavior is often associated with significant lipid loss, as illustrated in Figure 4.3, where membrane discontinuity appears on a previously continuous membrane structure. Usually the currents associated with the erratic signals are in nanoampere range and would continue to increase from the first occurrence of the signal. In very rare cases the erratic signals would vanish and the current reduces to picroampere range and regain a stable baseline. However, most frequently, these instances indicate membrane disintegration and are followed by a complete membrane rupture. With an increase in voltage, the probability of such signal occurrences also amplifies. Once the erratic signal appears, it will be counted as one event.

4.3.4 Data Analysis

Amyloid-membrane interaction were not observed in all experiments conducted. The initial step in data analysis involves distinguishing between the trials with and without events, and analyzing them separately. The number of experiments with amyloid-membrane interaction events and those without such events are determined for further analysis. The event count and activity duration analysis are exclusively applied to the experiments with amyloid-membrane interaction events. On the other hand, the voltage-current curve analysis is

performed on all experiments in the control group, the group with 50 μM melatonin and the group with 100 μM melatonin.

Evaluating Trial Activity

In our study, amyloid solution was injected in the bath on one side of the Teflon barrier, resulting in a final concentration of 5 μM in the bath, contributing to a concentration gradient across the barrier. Driven by the concentration gradient, the amyloid molecules then moved toward the painted membrane. If any types of event appears in the BLM trial, it implies that a substantial quantity of amyloid has come into contact with the membrane. Consequently, any subsequent measurements can be assumed to involve a membrane that has interacted with amyloid. However, there are instances where no signs of events are evident throughout the entire trial. This could occur because the amyloid has not adequately contacted the membrane, or because the event signals are too weak to distinguish from the baseline noise. In either of these cases, such trials are classified as inactive. In contrast, trials that exhibit at least one event are considered as active. The presence or absence of events in each trial can be readily determined through direct observation of the recorded trials. Trials without and with events are counted separately for each group either without melatonin or with 50 μM or 100 μM melatonin. These counts are then compared to assess amyloid activity within each group.

Event Count on Active Trials

An event count analysis was conducted on the identified active trials within each group for a more detailed investigation. The observed activities in each experimental trial were differentiated and classified according to the event category mentioned in the previous section. Subsequently, each event type was summarized for their total times of occurrence within each group. This allowed for a thorough comparative analysis, providing an insightful overview of event distribution and frequency.

Voltage-current Curve Analysis

The ClampFit software was utilized to calculate the average current of the trials. During an experiment, K^+ ions in the buffer can travel across the membrane through the defects and result in current change. For inactive trials, an average current was computed for each voltage level over the recorded time span (50 mV, 90 mV, 100 mV, 110 mV and 120 mV). The average current of each voltage was then plotted on an I-V graph, and a linear linear fit was created to determine the slope. The conductance of each trial could be determined using the equation $G = I/V$, where G is the slope of the linear fit.

For active trials, there could be multiple average currents within each voltage level. As mentioned earlier, step and erratic signals were considered separately and accounted for in their own average current calculation. All other events were regarded as part of the membrane activity. Therefore, I-V curves focusing on measuring the membrane permeability were generated using the average current data that exclude the step and erratic signals. These curves aimed to represent the conductance of the membrane rather than the amyloid pores or channels.

Activity Duration Analysis

As well as determining the count of events, which reflects the frequency of amyloid activities on the membrane, the duration of these events is important as it provides insight into the strength of the amyloid-membrane interaction. Longer events indicate a more persistent interaction, suggesting a higher level of damage inflicted by the amyloid on the membrane. Therefore, the duration of the events serves as an indicator of the extent to which the amyloid exerts its harmful effects on the membrane.

However, it is important to note that each type of event behaves differently. Spikes and multilevel events occur sporadically, instabilities vary in duration extensively, and steps and erratics are often integrated with other events and can last until the end of the trial in many cases. This variation in behaviour makes it challenging to count the separate event periods accurately.

As a result, the period of active membrane damage caused by amyloid interaction

should be considered from the first occurrence of any events, excluding spikes, until the last occurrence of any of those events. By focusing on the overall duration of amyloid activity, a more comprehensive understanding of the impact on the membrane can be achieved.

Finally, the durations of amyloid activity for each experiment of all three groups are plotted on the same graph and compared to assess the level of amyloid activity under each melatonin condition. This comparison allows for the evaluation of the impact of melatonin on amyloid-membrane interaction.

4.4 Results and Discussion

4.4.1 Evaluating Trial Activity

Table 4.1 presents the count of trials gathered for this study. The objective of the data collection was to achieve 20 repetitions per group, while maintaining the same active group count across all groups. Trials demonstrating prominent events are classified as active, whereas those devoid of event behaviours are considered inactive.

Of the 24 trials conducted in the control group without the presence of melatonin, 9 trials were found to be active, accounting for an activity of 37.5%. In contrast, the two melatonin-inclusive groups exhibited a comparable level of activity in their respective trials, with 45% of the 20 repetitions being active. Concurrently, the count of incomplete trials, i.e., those instances where the membrane ruptured during data collection due to amyloid interaction, was also counted and shown in the brackets in Table 4.1. The control group has 3 instances of incomplete repetitions out of all 9 active trials, whereas the groups incorporating melatonin included fewer incomplete repetitions. Specifically, all trials in the 50 μM Melatonin group were complete, while only one trial in the 100 μM Melatonin group was incomplete.

These findings suggest that membranes with melatonin exhibited increased amyloid activity, with the concentration of melatonin not influencing the count of amyloid-active trials. However, upon the observation of amyloid activity, melatonin-containing membranes

Groups	Total Trials	Active Trials	Inactive Trials	$\frac{ActiveTrials}{TotalTrials}$
Control	24	9 (3)	11	37.5%
With 50 μM Melatonin	20	9 (0)	11	45%
With 100 μM Melatonin	20	9 (1)	11	45%

Table 4.1: **Active/Inactive Trial Count.** Active trials with events and inactive trials without events were counted and the percentages of the active trials are included in the last column. The number of incomplete trials due to membrane rupture are shown in the brackets in the active trials column.

demonstrated a more extended lifespan compared to those without melatonin. A membrane incorporating melatonin was able to endure the entire duration of data collection, while the control group exhibited less stability.

Prior research has demonstrated that melatonin is capable to fluidize the lipid membrane by penetrating the lipid head group region. This fluidization property of melatonin may provide an explanation for the observed increased amyloid activity in the melatonin groups. Due to the enhanced fluidity of the membrane, it experiences greater fluctuations within the Teflon barrier hole, thereby increasing the likelihood of amyloid contact and interaction. On the other hand, despite the higher activity levels in the melatonin group, their active trials demonstrated a longer lifespan, suggesting that melatonin potentially protected the membrane from disintegration due to amyloid damage.

4.4.2 Event Count

Upon the determination of active trials in each group, an examination of the behaviour of individual trials can provide more insight on the nature of amyloid damages on the membrane in each instance. Deture *et al.* [7] previously introduced the primary event categories as spikes, steps, multilevels, and erratics. For this specific study, we supplemented the existing event types with an additional category, instabilities.

	Control	With 50 μM Melatonin	With 100 μM Melatonin
Total Trials	6	9	8
Total Events	55	83	110
Event Frequency	9.17	10.33	13.75
Spikes	44	21	37
Instabilities	8	15	18
Steps	1	31	35
Multilevels	2	9	12
Erratics	0	7	8

Table 4.2: **Event Count for Complete Active Trials.** Trials analyzed are all the complete active trials of each group. Event frequency is calculated as total events divided by total trials.

The number of all events from the active trials are listed in Table 4.2. Six active trials from the control group were contrasted with nine trials containing 50 μM melatonin and eight trials with 100 μM melatonin. We divided the event count over total trial count to calculate the frequency of the events. The control group exhibited an average of 9.17 events/trial, while the melatonin groups displayed 10.33 and 13.75 events per trial for 50 μM and 100 μM melatonin, respectively. Evidently, the presence of melatonin increased the average event count per trial, with the higher concentration leading to a more obviously enhanced event frequency.

Figure 4.9 summarizes the frequency of each event in each group. The control trials did not display any erratic signal; rather, they were dominated by spike events (80%), followed by instability events (15%). The rest of the events are composed of 1% steps, and 4% multilevel signals. Both melatonin groups exhibited similar event frequencies for instabilities, multilevels, and erratics. The primary difference lies in spike events. The group with 50 μM melatonin had 25% spike events and 37% steps, whereas the group with 100 μM melatonin had 37% spikes and 32% steps.The frequency of step signals was notably lower in the control group at a mere 1%, compared to 37% in the group with 50

μM melatonin and 32% in the group with 100 μM melatonin.

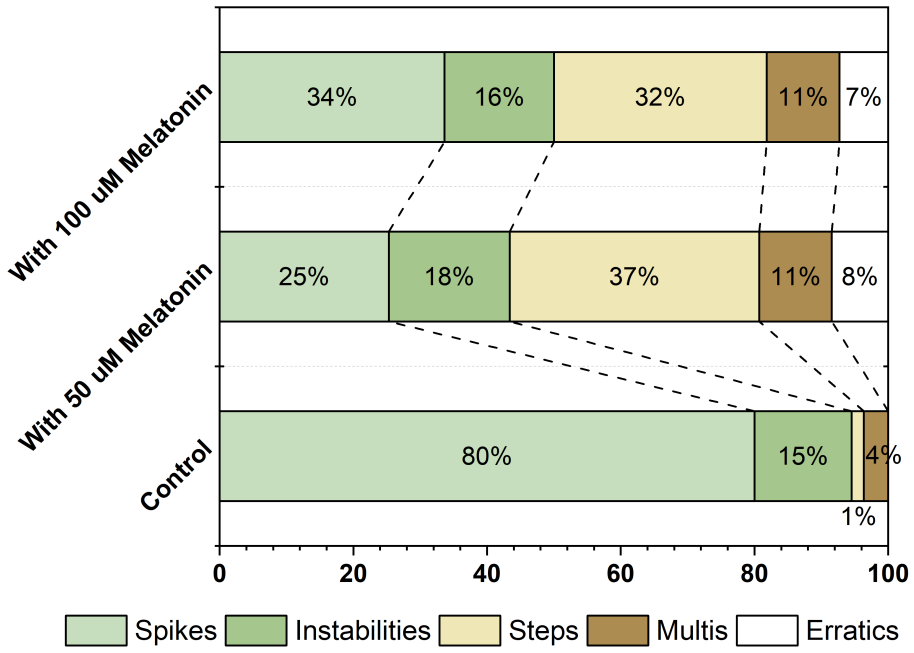


Figure 4.9: **Event Distributions** for the control, with 50 μM melatonin and with 100 μM melatonin groups.

Spike signals occur when amyloid molecules contact the membrane, causing abrupt fluctuations. The higher frequency of spike signals in the control group suggests that the membrane engages with amyloid without succumbing to the formation of pores or channels. The similar frequency of instability events across all three groups implies that the persistent amyloid-membrane interaction preceding any substantive damage is consistent, which does not depend on the presence of melatonin.

The frequency of step events is markedly higher in the melatonin groups, indicating that interaction between amyloid and the melatonin-enriched membrane are more likely to precipitate the formation of channels or pores, thereby facilitating a stable ion current flux. Moreover, the multilevel signal frequency in the melatonin groups was approximately

three times higher than that in the control group, suggesting a higher incidence of pore or channel formation in the melatonin group, with some demonstrating active opening and closing behavior. This also agrees with the spike events behaviour discussed in the previous paragraph.

Another interesting observation is the absence of erratic signals in the control group, while the 50 μM melatonin group displayed 8% and the 100 μM melatonin group showed 7%. When this finding is combined with the active trial count results, it can be inferred that melatonin is capable of maintaining the lipid membrane's integrity even under severe membrane damage, whereas in the control group devoid of melatonin, the membrane would be likely to rupture.

4.4.3 Voltage-current Curve Analysis

Figures 4.10 to 4.12 include I-V plots of the inactive trials of the three experimental groups. The linear regression analysis was applied to each plot to generate a linear fit and find it's slope, which represent the conductance for each trial according to the definition equation $G = I/V$. Only the linear fits with coefficient of determination (R^2) above 90% are considered as reliable results.

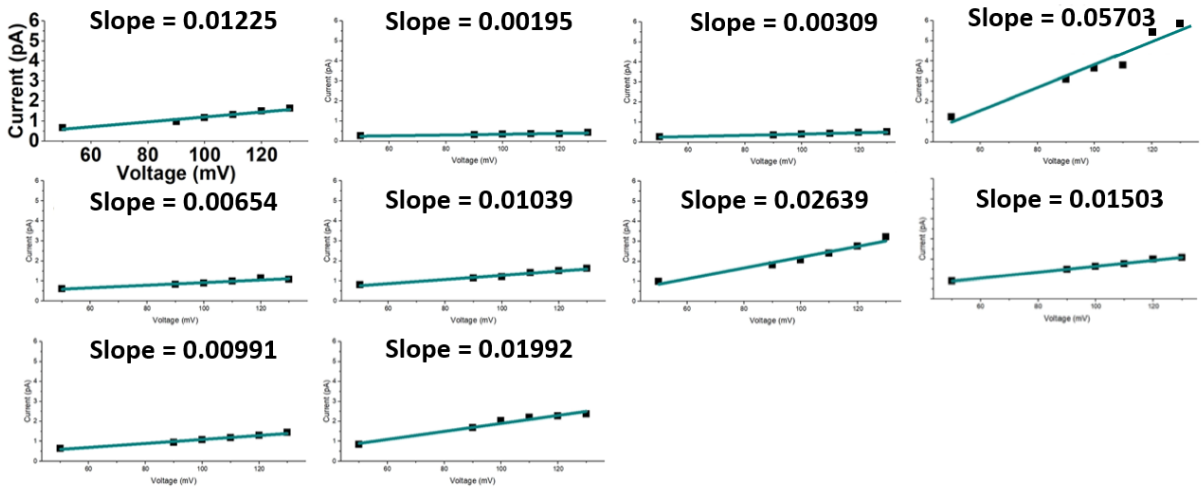


Figure 4.10: **I-V Curves of the Inactive Trials in the Control Group.** The voltages are 50 mV, 90 mV, 100 mV, 110 mV and 120 mV. Linear fit for each plot is shown in blue, and the slope is labeled in each plot.

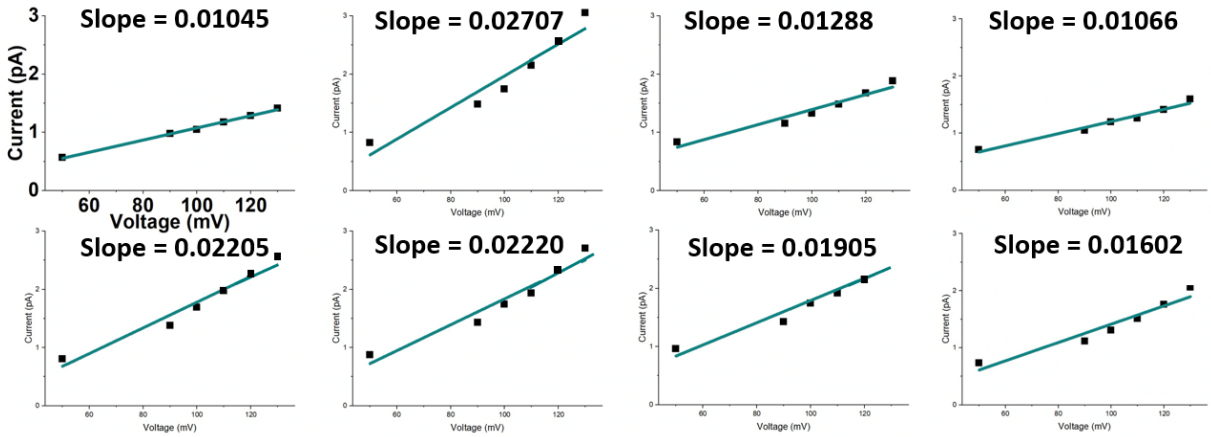


Figure 4.11: **I-V Curves of the Inactive Trials in the Group with 50 μM Melatonin.** The voltages are 50 mV, 90 mV, 100 mV, 110 mV and 120 mV. Linear fit for each plot is shown in blue, and the slope is labeled in each plot.

For the active trials, average current for each voltage level of the trial is taken when excluding step and erratic events because those represents the amyloid pore or channel

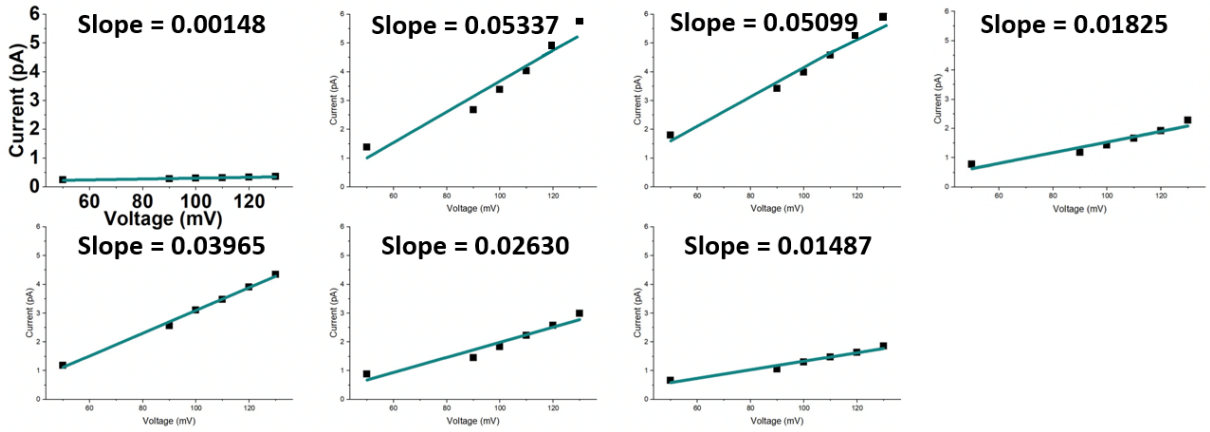


Figure 4.12: **I-V Curves of the Inactive Trials in the Group with 100 μM Melatonin.** The voltages are 50 mV, 90 mV, 100 mV, 110 mV and 120 mV. Linear fit for each plot is shown in blue, and the slope is labeled in each plot.

behaviours instead of the membrane itself. A separate analysis is done on the step and erratics signals and is discussed in the next paragraph. Figures 4.13 to 4.15 include the I-V plots on the active trials of the three groups. Fitting lines are generated with linear regression and only the curves with $R^2 > 90\%$ are used as final results.

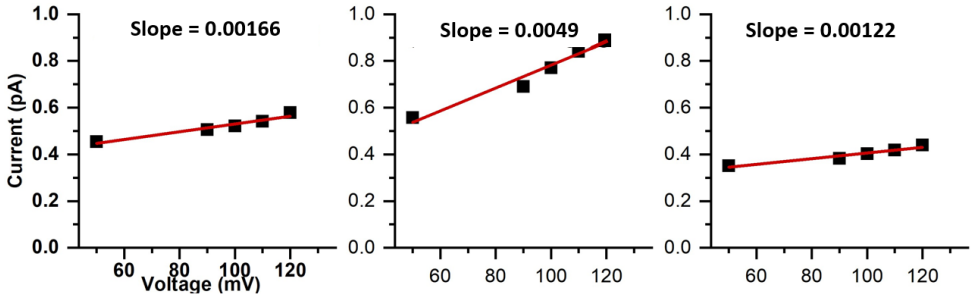


Figure 4.13: **I-V Curves of the Active Trials in the Control Group.** The voltages are 50 mV, 90 mV, 100 mV, 110 mV and 120 mV. Linear fit for each plot is shown in red, and the slope is labeled in each plot.

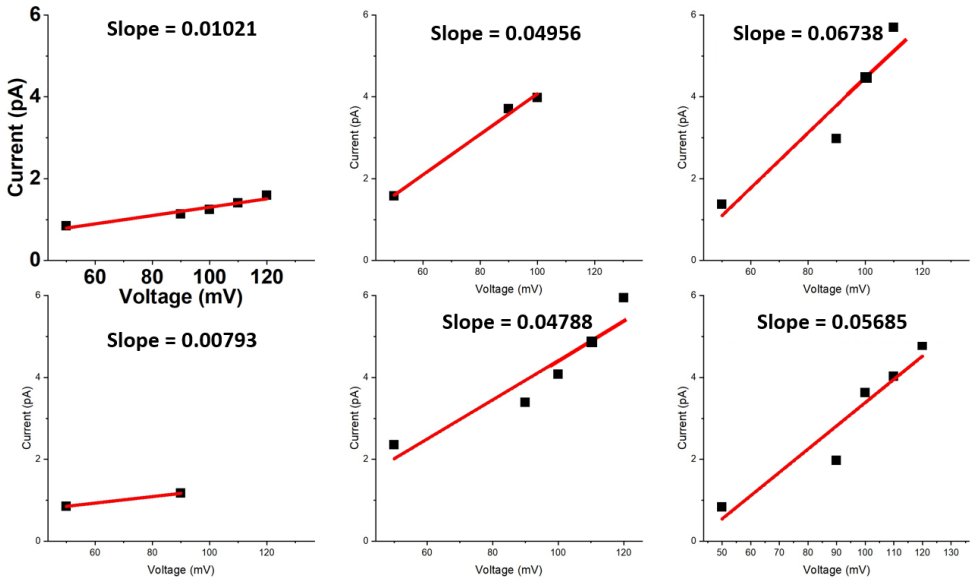


Figure 4.14: **I-V Curves of the Active Trials in the Group with 50 μM Melatonin.** The voltages are 50 mV, 90 mV, 100 mV, 110 mV and 120 mV. Linear fit for each plot is shown in red, and the slope is labeled in each plot.

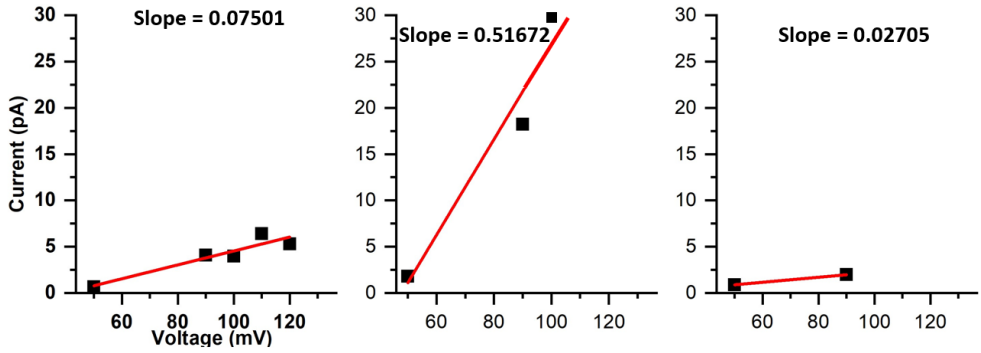


Figure 4.15: **I-V Curves of the Active Trials in the Group with 100 μM Melatonin.** The voltages are 50 mV, 90 mV, 100 mV, 110 mV and 120 mV. Linear fit for each plot is shown in red, and the slope is labeled in each plot.

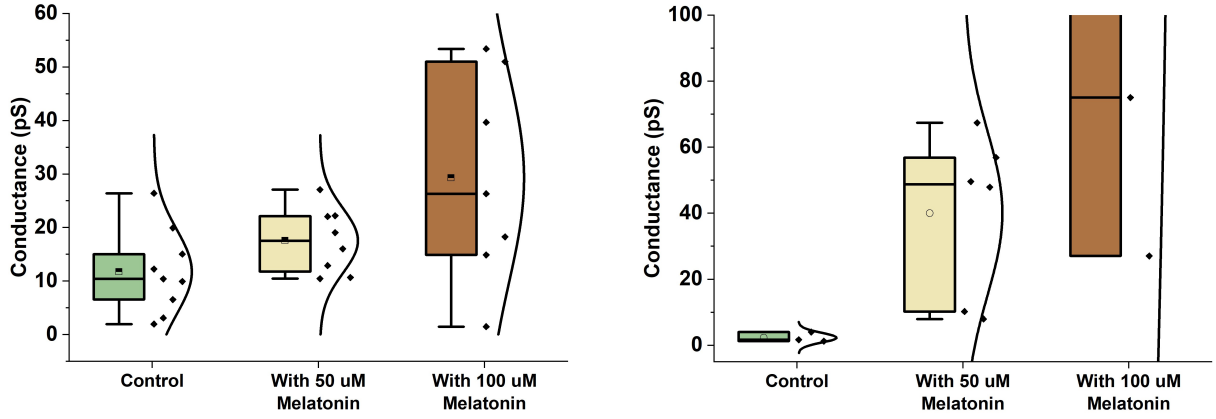
Figure 4.16 and Table 4.3 summarize the membrane conductance values for the inactive trials and the active trials according to their slopes. For the inactive trials, the conductance

for the control group is 11.72 ± 2.62 pS; that for the group with 50 μM melatonin is 17.55 ± 2.14 pS; and that for the group with 100 μM melatonin is 29.27 ± 7.35 pS. The presence of melatonin in the lipid membrane and the bath increased the average conductance for inactive trials. In other words melatonin appears to increase the membrane permeability towards potassium and chloride ions when amyloid is present, without any interaction, in the system. 50 μM melatonin does not shown significant effect on the conductance change from the control group because the p-value between these two groups are $0.11 > 0.05$. As well, the difference between two melatonin groups is not significant with a p-value equal to $0.12 > 0.05$, yet higher melatonin concentration does show a higher average conductance of the membrane in Figure 4.16a. The most well-pronounced increase in the membrane conductance appears between the control group and the group with 100 μM melatonin, with p-value equal to $0.02 < 0.05$. For this reason, one could tell that melatonin has a moderate capability in increasing the membrane permeability when amyloid is present in the bath, and the effect is more obvious with more concentrated melatonin. However, this set of analysis for inactive trials are for the experiments without observable events; whether this means no amyloid interaction with the membrane or very weak amyloid interaction, with events embedded in noise is undetermined. Therefore, we need to look into the active trials for more information on the degree of amyloid interaction and the level of damage to the membrane.

Groups	**Inactive Trials**	**Active Trials**
Control	11.72 ± 2.62	2.29 ± 0.86
With 50 μM Melatonin	17.55 ± 2.14	39.97 ± 10.17
With 100 μM Melatonin	29.27 ± 7.35	206.26 ± 155.85

Table 4.3: **Mean Values of the Conductance of the Inactive and Active Trials.** The values are represented as average ± standard error.

For the active trials, the conductance for control group is 2.29 ± 0.86 pS; that for the group with 50 μM melatonin is 39.97 ± 10.17 pS; and that for the group with 100 μM



(a) Inactive trials

(b) Active trials

Figure 4.16: **Inactive and Active Trial Conductances.** The unit of conductance is 10^{-12} S (pS). The distribution of the data are shown in box plots with the mean value represented by a half filled square. The violin curve associated with each box plot shows the data point density. Each data point is shown as a black diamond.

melatonin is 206.26 ± 155.85 pS. Though the conductance in the 100 μM melatonin group appears to be greater than that of the control and 50 μM melatonin groups, the large standard error of the 100 μM melatonin group leads to a p-value greater than 0.05 when comparing with the other groups, resulting in an insignificant difference. The conductance difference between the control group and the group with 50 μM melatonin has a p-value equal to $0.039 < 0.05$, indicating that the melatonin-containing membrane has an increased permeability to buffer ions when the membrane is interacting with amyloid.

Now let's look at the inactive and active trials within each individual group. For the control group, the average conductance value for the active trials appears to be lower than that of the inactive trials, but the difference is not significant (p-value $= 0.073 > 0.05$). The melatonin groups show an increased membrane average conductance and a larger variance for the active trials. For the group with 50 μM melatonin, the active conductance is significantly higher than the inactive conductance (p-value $= 0.029 < 0.05$). For the group with 100 μM melatonin, the active conductance is larger than the inactive conductance but the difference is not significant (p-value $= 0.096 > 0.05$) due to the large standard error

for the active trials. Once again the large standard error lead to insufficient comparison, therefore the effect of melatonin concentration to membrane permeability was not well determined. However, it indicates that higher melatonin concentration would destabilize the membrane and this effect is more obvious when the membrane has active amyloid interaction.

4.4.4 Activity Duration

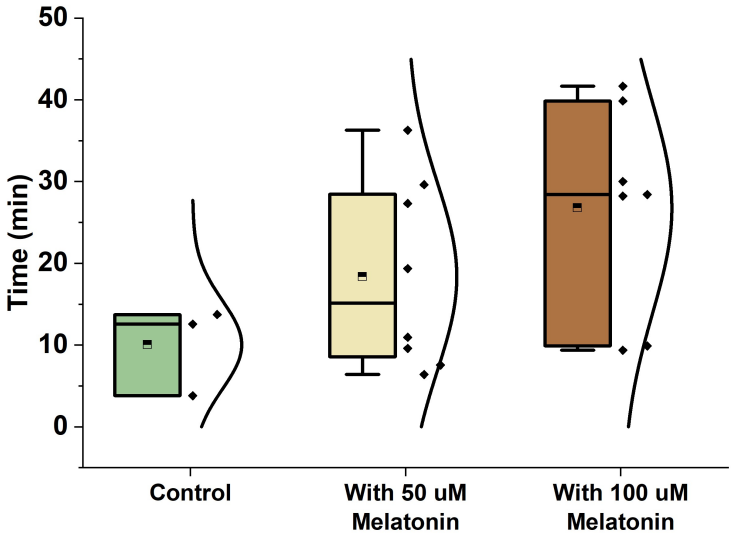


Figure 4.17: **Amyloid Activity Duration.** The distribution of the data were shown in box plots with the mean value represented by a half filled square. The violin curve associated with each box plot shows the data point density. Each data point is shown as a black diamond.

The activity durations for the active trials of the three models are summarized into Figure 4.17. The duration of amyloid interaction with the membrane has an increasing trend from no melatonin to higher concentration of melatonin. For the control group, amyloid activity lasts 10.03 $\pm$ 3.14 minutes; for the group with 50 μM melatonin, amyloid activity lasts 18.38 $\pm$ 4.06 minutes; and for the group with 100 μM melatonin, amyloid activity lasts 26.77 $\pm$ 4.87 minutes. Although any pair of the groups does not have a

significant difference in the duration of amyloid interaction, there is a trend that longer activities happens with increasing melatonin concentration. This indicates that in the group with more concentrated melatonin, amyloid tends to interact with the membrane earlier and at lower applied voltage in the recorded period. This finding is in agreement with the active trials determination analysis, where membranes with melatonin exhibited increased amyloid activity.

4.5 Conclusion

In this study, we explored amyloid interaction with lipid membranes prepared without melatonin, as well as with 50 μM and 100 μM concentrations of melatonin, utilizing the BLM technique. BLM successfully captured complex amyloid-membrane interactions by measuring event-specific current signals. Melatonin's presence induced more uncertainty in current measurements, suggesting its ability to fluidize the membrane and produce more fluctuations. Along with promoting more active amyloid trials and elevating the average membrane conductance and ion permeability, melatonin also decreased the likelihood of membrane rupture. While melatonin-enriched membranes initially show the formation of small pores, melatonin overall enhances the membrane's resistance to destructive amyloid damage, thereby maintaining membrane integrity. Our findings suggest that melatonin minimally impacts the overall amount of amyloid interaction events, but alters their nature, leading to fewer insertion or attaching onto the membrane surface from small oligomers but more stable pore/channel formation from lager aggregates. Importantly, melatonin appears to prolong membrane lifespan under amyloid interaction and decrease the risk of complete rupture. Future research should delve into the molecular dynamics of melatonin's interaction with the membrane and its effects at varied concentrations.

Chapter 5

Thesis Conclusions

This thesis delved into the effects of melatonin on model membrane systems that mimic neural cell membranes in the human brain. I selected a simple model (SPM) composed of DPPC, POPC, and cholesterol for both NMR and BLM investigations. The NMR study, detailed in Chapter 2, studied the phase behaviour of the lipid membrane when exposed to different melatonin concentrations. In Chapter 4, the BLM research evaluated various kinds of membrane damage resulting from the interaction between amyloid and membrane, and how melatonin influences these damages. The LSPR study in Chapter 3 employed a more intricate neuronal membrane model made up of DPPC, POPC, cholesterol, SM, and GM1. This model mimics various disease states, and the study shed light on how melatonin impacts the accumulation of amyloid layers on these model membranes. Below are the detailed conclusions for each investigation.

5.1 Melatonin's Effect in Simple Model Membrane Phase Behaviour

Using ^{2}H NMR, I investigated the impact of melatonin on the phase behaviour of DPPC, POPC, and cholesterol lipid membranes. My results suggest that melatonin can change phase separation in these mixtures by primarily incorporating into the disordered phase,

amplifying its level of disorder. The effect of melatonin was more prominent in POPC-d_{31} than DPPC-d_{62} mixtures, hinting at its preferential interaction with unsaturated lipids like POPC. This work sheds light on melatonin's antioxidative mechanisms and the significance of membrane domains in amyloid toxicity. The findings are pivotal for further studies on melatonin's membrane-level protective roles against Aβ.

5.2 Melatonin Affects Binding of Amyloid to the Model Membranes

Utilizing AFM and LSPR, the study was conducted to investigate amyloid interactions with model membranes mimicking the neuronal structure in various Alzheimer's disease stages, as well as the role of melatonin, an antioxidative hormone. The findings indicate that amyloid interactions with these membranes are disease-state-dependent, with the early diseased model (EDM) being particularly vulnerable. Furthermore, melatonin demonstrated a protective effect, notably inhibiting amyloid interactions within the EDM, suggesting its potential role in countering Alzheimer's progression in the early stages. However, as the disease progresses, this beneficial impact of melatonin appears to diminish, emphasizing the need for more comprehensive research into its molecular mechanisms and effects on membrane properties.

5.3 Melatonin's Effect on Amyloid Induced Membrane Damage to Simple Model Membrane

Using the BLM technique, I studied amyloid interactions with lipid membranes in the presence and absence of melatonin (50 μM and 100 μM). BLM revealed complex ion current patterns which correlates with varies suggested pathways of amyloid-membrane interactions, including insertion, accumulation, and pore formation. Melatonin increased membrane permeability, suggesting it fluidizes membranes. While increasing membrane current activity and ion permeability, melatonin reduced the probability of membrane rupture due

to amyloid damage over time. Melatonin's presence altered membrane physcial properties, leading to fewer attachments from small oligomers but more stable channels from larger aggregates. Importantly, melatonin enhanced membrane durability and longer resistance to amyloid induced damage. Further studies should probe melatonin's molecular effects on membranes at varying concentrations.

5.4 Conclusion

In conclusion, melatonin modifies physical properties of lipid membranes, which, in turn, alters the amyloid-membrane interactions, the amount of amyloid binding to the membrane, and also influences the types of damage inflicted on the membrane due to amyloid binding. Melatonin reduces the thickness of buildup layer of amyloids on the membrane, and its effects vary depending on the state of the lipid model membrane, most effectively in the early diseased model. Additionally, melatonin modulates the type of damage that amyloids inflict on simple lipid model membranes. Importantly, the presence of melatonin prolongs the membrane's lifespan, even in the face of amyloid-induced damage. These findings illuminate melatonin's protective effects on membranes via non-specific membrane incorporation, providing insights into its capability to prevent membrane rupture due to amyloid toxicity and to reduce amyloid binding and accumulation. These findings indicate the potential of melatonin to benefit AD patients, most importantly at the early stages of AD, and may eventually guide the development of therapeutic approaches for early prevention of this disease

5.5 Future Works

Future research, stemming from the foundations laid out in this thesis, can branch out in various directions. A paramount area of investigation is the impact of melatonin on lipid phase behaviour in increasingly intricate models, with NMR as a potential investigative tool. Particularly, the interactions between amyloid and lipid membranes can be probed more deeply. Utilizing solid-state ^{2}H NMR, as outlined in this thesis, offers an approach

to study the structural characteristics of the lipid membrane. Meanwhile, when exploring interactions between the amyloid and membrane, liquid-state NMR is typically more appropriate. In 2016, Korshavn *et al.* [194] employed ^{1}H-NMR to probe the aggregation of amyloid in the context of large unilamellar vesicle (LUV)s with single lipid component. Subsequent research could elevate the complexity of these vesicles. Future research should start with the simple model from this thesis and then progress to the 5-component neuronal cell models.

Furthermore, results from both LSPR and BLM studies have affirmed that combining these methods can offer a comprehensive insight into the interactions between amyloid and the membrane, as well as melatonin's protective role against membrane damage. As such, these paired techniques can be employed in future research on various lipid models, cellular membrane extracts, or different amyloid species, such as Aβ(1-40). By broadening the scope to include diverse lipid membrane compositions and multiple amyloid species, the protective properties of melatonin against amyloid-membrane damage could be more thoroughly understood.

In addition to the general interactions between amyloid and lipid membranes, it's crucial to recognize the role of Aβ oligomer receptors in the toxicity that amyloid oligomers impart on lipid membranes [195]. The LSPR technique, already widely applied in studying ligand-receptor binding by immobilizing receptors on the lipid membrane and introducing the ligand solution, can be uniquely leveraged. Future research could employ LSPR to scrutinize binding kinetics and seek potential inhibitors. Concurrently, BLM could serve as an adjunct method, helping determine the nature of membrane damage resulting from amyloid-receptor interactions.

In summary, this thesis paves the way for diversified future explorations into the lipid phase behaviour and amyloid interactions, with NMR techniques offering invaluable insights. With the successful integration of LSPR and BLM methodologies, researchers have a well-established frameword for uncovering melatonin's protective capacities against amyloid-induced membrane damage. As we delve deeper into the roles of Aβ oligomer receptors and expand on current models, we're moving closer to discovering potential therapeutic approaches for Alzheimer's disease.

Letter of Copyright Permission

Copyright Letter for Figure 1.4

ELSEVIER LICENSE
TERMS AND CONDITIONS

Nov 21, 2023

This Agreement between Dr. Nanqin Mei ("You") and Elsevier ("Elsevier") consists of your license details and the terms and conditions provided by Elsevier and Copyright Clearance Center.

License Number	5673510006882
License date	Nov 21, 2023
Licensed Content Publisher	Elsevier
Licensed Content Publication	Biochimica et Biophysica Acta (BBA) - Biomembranes
Licensed Content Title	Effect of melatonin and cholesterol on the structure of DOPC and DPPC membranes
Licensed Content Author	E. Drolle,N. Kučerka,M.I. Hoopes,Y. Choi,J. Katsaras,M. Karttunen,Z. Leonenko
Licensed Content Date	Sep 1, 2013
Licensed Content Volume	1828
Licensed Content Issue	9
Licensed Content Pages	8
Start Page	2247
End Page	2254

Type of Use	reuse in a thesis/dissertation
Portion	figures/tables/illustrations
Number of figures/tables/illustrations	1
Format	electronic
Are you the author of this Elsevier article?	No
Will you be translating?	No
Title of new work	The Role of Melatonin in Amyloid Interactions with the Model Neuronal Membranes
Institution name	University of Waterloo
Expected presentation date	Nov 2023
Portions	Figure 7
Requestor Location	Dr. Nanqin Mei 200 University Avenue West Waterloo, ON N2L 3G1 Canada Attn: Dr. Nanqin Mei
Publisher Tax ID	GB 494 6272 12
Total	0.00 CAD

Copyright Letter for Figure 1.10

ELSEVIER LICENSE
TERMS AND CONDITIONS

Nov 21, 2023

This Agreement between Dr. Nanqin Mei ("You") and Elsevier ("Elsevier") consists of your license details and the terms and conditions provided by Elsevier and Copyright Clearance Center.

License Number	5673510378022
License date	Nov 21, 2023
Licensed Content Publisher	Elsevier
Licensed Content Publication	Current Opinion in Colloid & Interface Science
Licensed Content Title	Black lipid membranes
Licensed Content Author	Mathias Winterhalter
Licensed Content Date	Jul 1, 2000
Licensed Content Volume	5
Licensed Content Issue	3-4
Licensed Content Pages Start	6
Page	250
End Page	255
Type of Use	reuse in a thesis/dissertation

Portion	figures/tables/illustrations
Number of figures/tables/illustrations	1
Format	electronic
Are you the author of this Elsevier article?	No
Will you be translating?	No
Title of new work	The Role of Melatonin in Amyloid Interactions with the Model Neuronal Membranes
Institution name	University of Waterloo
Expected presentation date	Nov 2023
Portions	Figure 1
Requestor Location	Dr. Nanqin Mei 200 University Avenue West Waterloo, ON N2L 3G1 Canada Attn: Dr. Nanqin Mei
Publisher Tax ID	GB 494 6272 12
Total	0.00 CAD

References

[1] Justyna B Startek, Brett Boonen, Karel Talavera, and Victor Meseguer. Trp channels as sensors of chemically-induced changes in cell membrane mechanical properties. *International Journal of Molecular Sciences*, 20(2):371, 2019.

[2] Elizabeth Drolle, Alexander Negoda, Keely Hammond, Evgeny Pavlov, and Zoya Leonenko. Changes in lipid membranes may trigger amyloid toxicity in Alzheimer's disease. *PloS One*, 12(8):e0182194, 2017.

[3] Youngjik Choi, Simon J. Attwood, Matthew I. Hoopes, Elizabeth Drolle, Mikko Karttunen, and Zoya Leonenko. Melatonin directly interacts with cholesterol and alleviates cholesterol effects in dipalmitoylphosphatidylcholine monolayers. *Soft Matter*, 10(1):206–213, 2014.

[4] David Nečas and Petr Klapetek. Gwyddion: an open-source software for SPM data analysis. *Central European Journal of Physics*, 10:181–188, 2012.

[5] Ghulam M Ashraf, Sandesh Chibber, Syed K Zaidi, Shams Tabrez, Ausaf Ahmad, Shazi Shakil, Gohar Mushtaq, Saleh S Baeesa, Mohammad A Kamal, et al. Recent updates on the association between Alzheimer's disease and vascular dementia. *Medicinal Chemistry*, 12(3):226–237, 2016.

[6] Christopher A Lane, John Hardy, and Jonathan M Schott. Alzheimer's disease. *European Journal of Neurology*, 25(1):59–70, 2018.

[7] Michael A DeTure and Dennis W Dickson. The neuropathological diagnosis of Alzheimer's disease. *Molecular Neurodegeneration*, 14(1):1–18, 2019.

[8] Vanessa J. De-Paula, Marcia Radanovic, Breno S. Diniz, and Orestes V. Forlenza. *Alzheimer's Disease*, pages 329–352. Springer Netherlands, Dordrecht, 2012.

[9] Rainulf A Stelzma, H Norman Schnitzlein, and F Reed Murllagh. An English I'ranslation of Alzheimer's 1907 Paper,"ijber eine eigenartige Erlranliung der Hirnrinde". *Clinical Anatomy*, 8:429–431, 1995.

[10] John A Hardy and Gerald A Higgins. Alzheimer's disease: The amyloid cascade hypothesis. *Science*, 256(5054):184–185, 1992.

[11] Dennis J Selkoe. Alzheimer's disease: Genes, proteins, and therapy. *Physiological Reviews*, 2001.

[12] Ganesh M Shankar, Shaomin Li, Tapan H Mehta, Amaya Garcia-Munoz, Nina E Shepardson, Imelda Smith, Francesca M Brett, Michael A Farrell, Michael J Rowan, Cynthia A Lemere, et al. Amyloid-β protein dimers isolated directly from Alzheimer's brains impair synaptic plasticity and memory. *Nature Medicine*, 14(8):837–842, 2008.

[13] Peter Niraj Nirmalraj, Jonathan List, Shayon Battacharya, Geoffrey Howe, Liang Xu, Damien Thompson, and Michael Mayer. Complete aggregation pathway of amyloid β (1-40) and (1-42) resolved on an atomically clean interface. *Science Advances*, 6(15):eaaz6014, 2020.

[14] Iryna Benilova, Eric Karran, and Bart De Strooper. The toxic Aβ oligomer and Alzheimer's disease: An emperor in need of clothes. *Nature Neuroscience*, 15(3):349–357, 2012.

[15] Sara M Butterfield and Hilal A Lashuel. Amyloidogenic protein–membrane interactions: Mechanistic insight from model systems. *Angewandte Chemie International Edition*, 49(33):5628–5654, 2010.

[16] D Allan Butterfield and Debra Boyd-Kimball. Amyloid β-Peptide (1-42) contributes to the oxidative stress and neurodegeneration found in Alzheimer disease brain. *Brain Pathology*, 14(4):426–432, 2004.

[17] Clemence Cheignon, M Tomas, D Bonnefont-Rousselot, Peter Faller, Christelle Hureau, and Fabrice Collin. Oxidative stress and the amyloid beta peptide in Alzheimer's disease. *Redox Biology*, 14:450–464, 2018.

[18] David C Bode, Mark D Baker, and John H Viles. Ion channel formation by amyloid-β42 oligomers but not amyloid-β40 in cellular membranes. *Journal of Biological Chemistry*, 292(4):1404–1413, 2017.

[19] Michele FM Sciacca, Samuel A Kotler, Jeffrey R Brender, Jennifer Chen, Dong-kuk Lee, and Ayyalusamy Ramamoorthy. Two-step mechanism of membrane disruption by aβ through membrane fragmentation and pore formation. *Biophysical Journal*, 103(4):702–710, 2012.

[20] David C Bode, Mark Freeley, Jon Nield, Matteo Palma, and John H Viles. Amyloid-β oligomers have a profound detergent-like effect on lipid membrane bilayers, imaged by atomic force and electron microscopy. *Journal of Biological Chemistry*, 294(19):7566–7572, 2019.

[21] Kai Simons and Julio L Sampaio. Membrane organization and lipid rafts. *Cold Spring Harbor Perspectives in Biology*, 3(10):a004697, 2011.

[22] Gerrit Van Meer, Dennis R Voelker, and Gerald W Feigenson. Membrane lipids: Where they are and how they behave. *Nature Reviews: Molecular Cell Biology*, 9(2):112–124, 2008.

[23] Kai Simons and Elina Ikonen. Functional rafts in cell membranes. *Nature*, 387(6633):569–572, 1997.

[24] Elizabeth Drolle, Norbert Kučerka, Matthew I. Hoopes, Youngjik Choi, John Katsaras, Mikko Karttunen, and Zoya Leonenko. Effect of melatonin and cholesterol on the structure of DOPC and DPPC membranes. *Biochimica et Biophysica Acta (BBA) - Biomembranes*, 1828(9):2247–2254, 2013.

[25] Junji Egawa, Matthew L Pearn, Brian P Lemkuil, Piyush M Patel, and Brian P Head. Membrane lipid rafts and neurobiology: Age-related changes in membrane

lipids and loss of neuronal function. *The Journal of Physiology*, 594(16):4565–4579, 2016.

[26] Urule Igbavboa, Nicolai A Avdulov, Friedhelm Schroeder, and W Gibson Wood. Increasing age alters transbilayer fluidity and cholesterol asymmetry in synaptic plasma membranes of mice. *Journal of Neurochemistry*, 66(4):1717–1725, 1996.

[27] Shlomo Yehuda, Sharon Rabinovitz, Ralph L Carasso, and David I Mostofsky. The role of polyunsaturated fatty acids in restoring the aging neuronal membrane. *Neurobiology of Aging*, 23(5):843–853, 2002.

[28] D Allan Butterfield, Jennifer Drake, Chava Pocernich, and Alessandra Castegna. Evidence of oxidative damage in Alzheimer's disease brain: Central role for amyloid β-peptide. *Trends in Molecular Medicine*, 7(12):548–554, 2001.

[29] Ilaria Liguori, Gennaro Russo, Francesco Curcio, Giulia Bulli, Luisa Aran, David Della-Morte, Gaetano Gargiulo, Gianluca Testa, Francesco Cacciatore, Domenico Bonaduce, and Pasquale Abete. Oxidative stress, aging, and diseases. *Clinical Interventions in Aging*, pages 757–772, 2018.

[30] Jo V Rushworth and Nigel M Hooper. Lipid rafts: Linking Alzheimer's amyloid-β production, aggregation, and toxicity at neuronal membranes. *International Journal of Alzheimer's Disease*, 2011, 2011.

[31] Mehdi Azouz, Christophe Cullin, Sophie Lecomte, and Michel Lafleur. Membrane domain modulation of Aβ 1–42 oligomer interactions with supported lipid bilayers: An atomic force microscopy investigation. *Nanoscale*, 11(43):20857–20867, 2019.

[32] Takeshi Kawarabayashi, Mikio Shoji, Linda H Younkin, Lin Wen-Lang, Dennis W Dickson, Tetsuro Murakami, Etsuro Matsubara, Koji Abe, Karen Hsiao Ashe, and Steven G Younkin. Dimeric amyloid β protein rapidly accumulates in lipid rafts followed by apolipoprotein E and phosphorylated tau accumulation in the Tg2576 mouse model of Alzheimer's disease. *Journal of Neuroscience*, 24(15):3801–3809, 2004.

[33] Ritchie Williamson, Alessia Usardi, Diane P Hanger, and Brian H Anderton. Membrane-bound β-amyloid oligomers are recruited into lipid rafts by a fyn-dependent mechanism. *The FASEB Journal*, 22(5):1552–1559, 2008.

[34] Alain Bolaño Alvarez, Benjamín Caruso, Pablo EA Rodríguez, Steffen B Petersen, and Gerardo D Fidelio. Aβ-amyloid fibrils are self-triggered by the interfacial lipid environment and low peptide content. *Langmuir*, 36(28):8056–8065, 2020.

[35] Kyle J Korshavn, Cristina Satriano, Yuxi Lin, Rongchun Zhang, Mark Dulchavsky, Anirban Bhunia, Magdalena I Ivanova, Young-Ho Lee, Carmelo La Rosa, Mi Hee Lim, and Ayyalusamy Ramamoorthy. Reduced lipid bilayer thickness regulates the aggregation and cytotoxicity of amyloid-β. *Journal of Biological Chemistry*, 292(11):4638–4650, 2017.

[36] Francis Hane, Elizabeth Drolle, Ravi Gaikwad, Erin Faught, and Zoya Leonenko. Amyloid-β aggregation on model lipid membranes: An atomic force microscopy study. *Journal of Alzheimer's Disease*, 26(3):485–494, 2011.

[37] Alessandra Luchini and Giuseppe Vitiello. Mimicking the mammalian plasma membrane: An overview of lipid membrane models for biophysical studies. *Biomimetics*, 6(1):3, 2020.

[38] Zheng Niu, Zhengfeng Zhang, Weijing Zhao, and Jun Yang. Interactions between amyloid β peptide and lipid membranes. *Biochimica et Biophysica Acta (BBA) - Biomembranes*, 1860(9):1663–1669, 2018.

[39] Laura Picas, Pierre-Emmanuel Milhiet, and Jordi Hernández-Borrell. Atomic force microscopy: A versatile tool to probe the physical and chemical properties of supported membranes at the nanoscale. *Chemistry and Physics of Lipids*, 165(8):845–860, 2012.

[40] James H Davis. The description of membrane lipid conformation, order and dynamics by 2H-NMR. *Biochimica et Biophysica Acta (BBA) - Biomembranes*, 737(1):117–171, 1983.

[41] Tone Bengtsen, Viktor L Holm, Lisbeth Ravnkilde Kjølbye, Søren R Midtgaard, Nicolai Tidemand Johansen, Giulio Tesei, Sandro Bottaro, Birgit Schiøtt, Lise Arleth, and Kresten Lindorff-Larsen. Structure and dynamics of a nanodisc by integrating nmr, saxs and sans experiments with molecular dynamics simulations. *Elife*, 9:e56518, 2020.

[42] Yuri Gerelli, Lionel Porcar, and Giovanna Fragneto. Lipid rearrangement in DSPC/DMPC bilayers: A neutron reflectometry study. *Langmuir*, 28(45):15922–15928, 2012.

[43] Bruno Claustrat, Jocelyne Brun, and Guy Chazot. The basic physiology and pathophysiology of melatonin. *Sleep Medicine Reviews*, 9(1):11–24, 2005.

[44] Md Farhad Hossain, Ni Wang, Ruijun Chen, Siwen Li, Jaydeep Roy, Md Giash Uddin, Zhong Li, Lee Wei Lim, and You-Qiang Song. Exploring the multifunctional role of melatonin in regulating autophagy and sleep to mitigate Alzheimer's disease neuropathology. *Ageing Research Reviews*, 67:101304, 2021.

[45] Jaydeep Roy, Kan Yin Wong, Luca Aquili, Md Sahab Uddin, Boon Chin Heng, George Lim Tipoe, Kah Hui Wong, Man Lung Fung, and Lee Wei Lim. Role of melatonin in Alzheimer's disease: From preclinical studies to novel melatonin-based therapies. *Frontiers in Neuroendocrinology*, 65:100986, 2022.

[46] Li Lin, Qiong-Xia Huang, Shu-Sheng Yang, Jiang Chu, Jian-Zhi Wang, and Qing Tian. Melatonin in Alzheimer's disease. *International Journal of Molecular Sciences*, 14(7):14575–14593, 2013.

[47] Mayuri Shukla, Piyarat Govitrapong, Parichart Boontem, Russel J Reiter, and Jutamaad Satayavivad. Mechanisms of melatonin in alleviating Alzheimer's disease. *Current Neuropharmacology*, 15(7):1010–1031, 2017.

[48] Yu-Hang Gong, Nan Hua, Xuan Zang, Tao Huang, and Ling He. Melatonin ameliorates Aβ1-42-induced Alzheimer's cognitive deficits in mouse model. *Journal of Pharmacy and Pharmacology*, 70(1):70–80, 2018.

[49] Daniel P Cardinali, Daniel E Vigo, Natividad Olivar, María F Vidal, Analía M Furio, and Luis I Brusco. Therapeutic application of melatonin in mild cognitive impairment. *American Journal of Neurodegenerative Disease*, 1(3):280, 2012.

[50] Dun Xian Tan, Bing Xu, Xinjia Zhou, and Russel J Reiter. Pineal calcification, melatonin production, aging, associated health consequences and rejuvenation of the pineal gland. *Molecules*, 23(2):301, 2018.

[51] Tomáš Kondela, Ermuhammad Dushanov, Maria Vorobyeva, Kahramon Mamatkulov, Elizabeth Drolle, Dmytro Soloviov, Pavol Hrubovčák, Kholmirzo Kholmurodov, Grigory Arzumanyan, Zoya Leonenko, et al. Investigating the competitive effects of cholesterol and melatonin in model lipid membranes. *Biochimica et Biophysica Acta (BBA) - Biomembranes*, 1863(9):183651, 2021.

[52] Nanqin Mei, Morgan Robinson, James H Davis, and Zoya Leonenko. Melatonin alters fluid phase coexistence in POPC/DPPC/cholesterol membranes. *Biophysical Journal*, 119(12):2391–2402, 2020.

[53] Feride Severcan, Ipek Sahin, and Nadide Kazancı. Melatonin strongly interacts with zwitterionic model membranes—evidence from Fourier transform infrared spectroscopy and differential scanning calorimetry. *Biochimica et Biophysica Acta (BBA) - Biomembranes*, 1668(2):215–222, 2005.

[54] Arthur G Palmer III. Nmr characterization of the dynamics of biomacromolecules. *Chemical Reviews*, 104(8):3623–3640, 2004.

[55] Edward M Purcell, Henry Cutler Torrey, and Robert V Pound. Resonance absorption by nuclear magnetic moments in a solid. *Physical Review*, 69(1-2):37, 1946.

[56] Charles P Slichter. *Principles of magnetic resonance*, volume 1. Springer Science & Business Media, 2013.

[57] Malcolm H Levitt. *Spin dynamics: Basics of nuclear magnetic resonance*. John Wiley & Sons, 2013.

[58] Gerald W Stockton, Kenneth G Johnson, Keith W Butler, AP Tulloch, Yvan Boulanger, Ian CP Smith, James H Davis, and Myer Bloom. Deuterium nmr study of lipid organisation in acholeplasma laidlawii membranes. *Nature*, 269(5625):267–268, 1977.

[59] James H Davis and Kenneth R Jeffrey. The temperature dependence of chain disorder in potassium palmitate-water. A deuterium NMR study. *Chemistry and Physics of Lipids*, 20(2):87–104, 1977.

[60] Atul Singh Minhas and Ruth Oliver. Magnetic resonance imaging basics. *Electrical Properties of Tissues: Quantitative Magnetic Resonance Mapping*, pages 47–82, 2022.

[61] James Keeler. *Understanding NMR spectroscopy*. John Wiley & Sons, 2010.

[62] Peter J Hore. *Nuclear magnetic resonance*. Oxford University Press, USA, 2015.

[63] Kathryn M Mayer and Jason H Hafner. Localized surface plasmon resonance sensors. *Chemical Reviews*, 111(6):3828–3857, 2011.

[64] Katherine A Willets and Richard P Van Duyne. Localized surface plasmon resonance spectroscopy and sensing. *Annual Review of Physical Chemistry*, 58:267–297, 2007.

[65] Briliant Adhi Prabowo, Agnes Purwidyantri, and Kou-Chen Liu. Surface plasmon resonance optical sensor: A review on light source technology. *Biosensors*, 8(3):80, 2018.

[66] Amanda J Haes, Christy L Haynes, Adam D McFarland, George C Schatz, Richard P Van Duyne, and Shengli Zou. Plasmonic materials for surface-enhanced sensing and spectroscopy. *MRS Bulletin*, 30(5):368–375, 2005.

[67] Eleonora Petryayeva and Ulrich J Krull. Localized surface plasmon resonance: Nanostructures, bioassays and biosensing—A review. *Analytica Chimica Acta*, 706(1):8–24, 2011.

[68] Gerd Binnig, Calvin F Quate, and Ch Gerber. Atomic force microscope. *Physical Review Letters*, 56(9):930, 1986.

[69] F Moreno-Herrero, J Colchero, J Gomez-Herrero, and AM Baro. Atomic force microscopy contact, tapping, and jumping modes for imaging biological samples in liquids. *Physical Review E*, 69(3):031915, 2004.

[70] Nader Jalili and Karthik Laxminarayana. A review of atomic force microscopy imaging systems: Application to molecular metrology and biological sciences. *Mechatronics*, 14(8):907–945, 2004.

[71] Andreas Stylianou, Stylianos-Vasileios Kontomaris, Colin Grant, Eleni Alexandratou, et al. Atomic force microscopy on biological materials related to pathological conditions. *Scanning*, 2019, 2019.

[72] David Alsteens, Heykel Trabelsi, Patrice Soumillion, and Yves F Dufrêne. Multiparametric atomic force microscopy imaging of single bacteriophages extruding from living bacteria. *Nature Communications*, 4(1):2926, 2013.

[73] Elizabeth Drolle, Francis Hane, Brenda Lee, and Zoya Leonenko. Atomic force microscopy to study molecular mechanisms of amyloid fibril formation and toxicity in Alzheimer's disease. *Drug Metabolism Reviews*, 46(2):207–223, 2014.

[74] Paul Mueller, Donald O Rudin, H Ti Tien, and William C Wescott. Reconstitution of cell membrane structure in vitro and its transformation into an excitable system. *Nature*, 194(4832):979–980, 1962.

[75] Imke Wiedemann, Roland Benz, and Hans-Georg Sahl. Lipid II-mediated pore formation by the peptide antibiotic nisin: A black lipid membrane study. *Journal of Bacteriology*, 186(10):3259–3261, 2004.

[76] Amani Alghalayini, Alvaro Garcia, Thomas Berry, and Charles G Cranfield. The use of tethered bilayer lipid membranes to identify the mechanisms of antimicrobial peptide interactions with lipid bilayers. *Antibiotics*, 8(1):12, 2019.

[77] Günther Boheim. Statistical analysis of alamethicin channels in black lipid membranes. *The Journal of Membrane Biology*, 19(1):277–303, 1974.

[78] Evgeny Pavlov, Eleonora Zakharian, Christopher Bladen, Catherine TM Diao, Chelsey Grimbly, Rosetta N Reusch, and Robert J French. A large, voltage-dependent channel, isolated from mitochondria by water-free chloroform extraction. *Biophysical Journal*, 88(4):2614–2625, 2005.

[79] S Sonnino and A Prinetti. Membrane domains and the "lipid raft" concept. *Current Medicinal Chemistry*, 20(1):4–21, 2013.

[80] James H Davis, Jesse James Clair, and Janos Juhasz. Phase equilibria in DOPC/DPPC-d62/cholesterol mixtures. *Biophysical Journal*, 96(2):521–539, 2009.

[81] Frederick A Heberle, Robin S Petruzielo, Jianjun Pan, Paul Drazba, Norbert Kucerka, Robert F Standaert, Gerald W Feigenson, and John Katsaras. Bilayer thickness mismatch controls domain size in model membranes. *Journal of the American Chemical Society*, 135(18):6853–6859, 2013.

[82] Sarah L Veatch and Sarah L Keller. Separation of liquid phases in giant vesicles of ternary mixtures of phospholipids and cholesterol. *Biophysical Journal*, 85(5):3074–3083, 2003.

[83] ZV Leonenko, E Finot, H Ma, TES Dahms, and DT Cramb. Investigation of temperature-induced phase transitions in dopc and dppc phospholipid bilayers using temperature-controlled scanning force microscopy. *Biophysical Journal*, 86(6):3783–3793, 2004.

[84] Margus R Vist and James H Davis. Phase equilibria of cholesterol/dipalmitoylphosphatidylcholine mixtures: Deuterium nuclear magnetic resonance and differential scanning calorimetry. *Biochemistry*, 29(2):451–464, 1990.

[85] Anders Aufderhorst-Roberts, Udayan Chandra, and Simon D Connell. Three-phase coexistence in lipid membranes. *Biophysical Journal*, 112(2):313–324, 2017.

[86] Jonathan D Nickels, Sneha Chatterjee, Christopher B Stanley, Shuo Qian, Xiaolin Cheng, Dean AA Myles, Robert F Standaert, James G Elkins, and John Katsaras. The in vivo structure of biological membranes and evidence for lipid domains. *PLoS Biology*, 15(5):e2002214, 2017.

[87] Virginia Martín, Noemí Fabelo, Gabriel Santpere, Berta Puig, Raquel Marín, Isidre Ferrer, and Mario Díaz. Lipid alterations in lipid rafts from Alzheimer's disease human brain cortex. *Journal of Alzheimer's Disease*, 19(2):489–502, 2010.

[88] Robin B Chan, Tiago G Oliveira, Etty P Cortes, Lawrence S Honig, Karen E Duff, Scott A Small, Markus R Wenk, Guanghou Shui, and Gilbert Di Paolo. Comparative lipidomic analysis of mouse and human brain with Alzheimer disease. *Journal of Biological Chemistry*, 287(4):2678–2688, 2012.

[89] Fernando J. Sepulveda, Jorge Parodi, Robert W. Peoples, Carlos Opazo, and Luis G. Aguayo. Synaptotoxicity of Alzheimer beta amyloid can be explained by its membrane perforating property. *PLoS One*, 5(7):1–9, 2010.

[90] Gintaras Valincius, Frank Heinrich, Rima Budvytyte, David J Vanderah, Duncan J McGillivray, Yuri Sokolov, James E Hall, and Mathias Lösche. Soluble amyloid β-oligomers affect dielectric membrane properties by bilayer insertion and domain formation: Implications for cell toxicity. *Biophysical Journal*, 95(10):4845–4861, 2008.

[91] Mariagioia Zampagni, Elisa Evangelisti, Roberta Cascella, Gianfranco Liguri, Matteo Becatti, Anna Pensalfini, Daniela Uberti, Giovanna Cenini, Maurizio Memo, Silvia Bagnoli, Benedetta Nacmias, Sandro Sorbi, and Cristina Cecchi. Lipid rafts are primary mediators of amyloid oxidative attack on plasma membrane. *Journal of Molecular Medicine*, 88(6):597–608, 2010.

[92] Cristina Cecchi and Massimo Stefani. The amyloid-cell membrane system. The interplay between the biophysical features of oligomers/fibrils and cell membrane defines amyloid toxicity. *Biophysical Chemistry*, 182:30–43, 2013.

[93] Alexandra M Nicholson and Adriana Ferreira. Increased membrane cholesterol might render mature hippocampal neurons more susceptible to beta-amyloid-induced calpain activation and tau toxicity. *Journal of Neuroscience*, 29(14):4640–51, 2009.

[94] Regina Brigelius-Flohé and Maret G Traber. Vitamin E: Function and metabolism. *The FASEB Journal*, 13(10):1145–1155, 1999.

[95] Dun-Xian Tan, Lucien C Manchester, Lilan Qin, and Russel J Reiter. Melatonin: A mitochondrial targeting molecule involving mitochondrial protection and dynamics. *International Journal of Molecular Sciences*, 17(12):2124, 2016.

[96] Zheng Feng and Jun-Tian Zhang. Protective effect of melatonin on beta-amyloid-induced apoptosis in rat astroglioma C6 cells and its mechanism. *Free Radical Biology and Medicine*, 37(11):1790–1801, 2004.

[97] M a Pappolla, M Sos, R a Omar, R J Bick, D L Hickson-Bick, R J Reiter, S Efthimiopoulos, and N K Robakis. Melatonin prevents death of neuroblastoma cells exposed to the Alzheimer amyloid peptide. *Journal of Neuroscience*, 17(5):1683–1690, 1997.

[98] Tahir Ali and Myeong Ok Kim. Melatonin ameliorates amyloid beta-induced memory deficits, tau hyperphosphorylation and neurodegeneration via PI3/Akt/GSk3β pathway in the mouse hippocampus. *Journal of Pineal Research*, 59(1):47–59, 2015.

[99] James M. Olcese, Chuanhai Cao, Takashi Mori, Malgorzata B. Mamcarz, Anne Maxwell, Melissa J. Runfeldt, Li Wang, Chi Zhang, Xiaoyang Lin, Guixin Zhang, and Gary W. Arendash. Protection against cognitive deficits and markers of neurodegeneration by long-term oral administration of melatonin in a transgenic model of Alzheimer disease. *Journal of Pineal Research*, 47(1):82–96, 2009.

[100] Miguel Pappolla, Marcia Simovich, Tara Bryant-Thomas, YauJan Chyan, Burkhard Poeggeler, Margarita Dubocovich, Roger Bick, George Perry, Felix Cruz-Sanchez, and Mark Smith. The neuroprotective activities of melatonin against the Alzheimer beta-protein are not mediated by melatonin membrane receptors. *Journal of Pineal Research*, 32(3):135–142, 2002.

[101] Joaquín J García, Laura López-Pingarrón, Priscilla Almeida-Souza, Alejandro Tres, Pilar Escudero, Francisco A García-Gil, Dun-Xian Tan, Russel J Reiter, Jose M Ramírez, and Milagros Bernal-Pérez. Protective effects of melatonin in reducing oxidative stress and in preserving the fluidity of biological membranes: A review. *Journal of Pineal Research*, 56(3):225–237, 2014.

[102] Vânia R De Lima, Miguel SB Caro, Maximiliano L Munford, Bernard Desbat, Erick Dufourc, André A Pasa, and Tânia B Creczynski-Pasa. Influence of melatonin on the order of phosphatidylcholine-based membranes. *Journal of Pineal Research*, 49(2):169–175, 2010.

[103] Morgan Robinson, Stephen Turnbull, Brenda Yasie Lee, and Zoya Leonenko. The effects of melatonin, serotonin, tryptophan and NAS on the biophysical properties of DPPC monolayers. *Biochimica et Biophysica Acta (BBA) - Biomembranes*, page 183363, 2020.

[104] Hannah Dies, Bonnie Cheung, Jennifer Tang, and Maikel C. Rheinstädter. The organization of melatonin in lipid membranes. *Biochimica et Biophysica Acta (BBA) - Biomembranes*, 1848(4):1032–1040, 2015.

[105] Dima Bolmatov, William T McClintic, Graham Taylor, Christopher B Stanley, Changwoo Do, C Patrick Collier, Zoya Leonenko, Maxim O Lavrentovich, and John Katsaras. Deciphering melatonin-stabilized phase separation in phospholipid bilayers. *Langmuir*, 35(37):12236–12245, 2019.

[106] James H Davis. Deuterium magnetic resonance study of the gel and liquid crystalline phases of dipalmitoyl phosphatidylcholine. *Biophysical Journal*, 27(3):339–358, 1979.

[107] L. C. M. van Gorkom, J. M. Hook, M. B. Logan, J. V. Hanna, and R. E. Wasylishen. Solid-state lead-207 NMR of lead(II) nitrate: Localized heating effects at high magic angle spinning speeds. *Magnetic Resonance in Chemistry*, 33:791–795, 2013.

[108] P. A. Beckmann and C. Dybowski. A thermometer for nonspinning solid-state nmr spectroscopy. *Journal of Magnetic Resonance*, 146:379–380, 2000.

[109] James H Davis, KR Jeffrey, M Bloom, MI Valic, and TP Higgs. Quadrupolar echo deuteron magnetic resonance spectroscopy in ordered hydrocarbon chains. *Chemical Physics Letters*, 42(2):390–394, 1976.

[110] Wei Zhao, David E Moilanen, Emily E Fenn, and Michael D Fayer. Water at the surfaces of aligned phospholipid multibilayer model membranes probed with ultrafast

vibrational spectroscopy. *Journal of the American Chemical Society*, 130(42):13927–13937, 2008.

[111] M. Bloom, J. H. Davis, and M. I. Valic. Spectral distortion effects due to finite pulse widths in deuterium nuclear magnetic resonance spectroscopy. *Canadian Journal of Physics*, 58:1510–1517, 1980.

[112] A. Keyvanloo, M. Shaghaghi, J. J. Zuckermann, and J. L. Thewalt. The phase behavior and organization of sphingomyelin/cholesterol membranes: A deuterium NMR study. *Biophysical Journal*, 114:1344–1356, 2018.

[113] Miranda L Schmidt, Latifa Ziani, Michelle Boudreau, and James H Davis. Phase equilibria in DOPC/DPPC: Conversion from gel to subgel in two component mixtures. *The Journal of Chemical Physics*, 131(17):175103, 2009.

[114] Derek Marsh. *Handbook of lipid bilayers*. CRC press, 2013.

[115] A Tardieu, Vittorio Luzzati, and FC Reman. Structure and polymorphism of the hydrocarbon chains of lipids: A study of lecithin-water phases. *Journal of Molecular Biology*, 75(4):711–733, 1973.

[116] James H Davis and Miranda L Schmidt. *Cholesterol in Model Membranes*, page 325–364. Walter de Gruyter GmbH, 2019.

[117] J. Zhao, J. Wu, H. Shao, F. Kong, N. Jain, Gunt, and G. Feigenson. Phase studies of model biomembranes: Macroscopic coexistence of Lα + Lβb, with light-induced coexistence of Lα + Lo phases. *Biochimica et Biophysica Acta (BBA) - Biomembranes*, 1768:2777–2786, 2007.

[118] T. M. Konlyakhina, S. L. Goh, J. Amazon, F. A. Heberle, J. Wu, and G. W. Feigenson. Control of a nanoscopic-to-macroscopic transition: Modulated phases in four-component DSPC/DOPC/POPC/Chol giant unilamellar vesicles. *Biophysical Journal*, 101:L08–L20, 2011.

[119] S. L. Goh, J. J. Amazon, and G. W. Feigenson. Toward a better raft model: Modulated phases in the four-component bilayer, DSPC/DOPC/POPC/CHOL. *Biophysical Journal*, 104:853–862, 2013.

[120] F. A. Heberle, R. S. Petruzielo, J. Pan, P. Drazba, N. Kucerka, R. F. Standaert, G. W. Feignson, and J. Katsaras. Bilayer thickness mismatch controls domain size in model membranes. *Journal of the American Chemical Society*, 135:6853–6859, 2013.

[121] Norbert Kučerka, Mu-Ping Nieh, and John Katsaras. Fluid phase lipid areas and bilayer thicknesses of commonly used phosphatidylcholines as a function of temperature. *Biochimica et Biophysica Acta (BBA) - Biomembranes*, 1808(11):2761–2771, 2011.

[122] David Bongiorno, Leopoldo Ceraulo, Mirella Ferrugia, Felice Filizzola, Angela Ruggirello, and Vincenzo Turco Liveri. Localization and interactions of melatonin in dry cholesterol/lecithin mixed reversed micelles used as cell membrane models. *Journal of Pineal Research*, 38(4):292–298, 2005.

[123] Dun-Xian Tan, Lucien C Manchester, Emilio Sanchez-Barcelo, Maria D Mediavilla, and Russel J Reiter. Significance of high levels of endogenous melatonin in mammalian cerebrospinal fluid and in the central nervous system. *Current Neuropharmacology*, 8(3):162–167, 2010.

[124] Joaquín J. García, Russel J. Reiter, Juan M. Guerrero, Germaine Escames, Byung P. Yu, Chang S. Oh, and Antonio Muñoz-Hoyos. Melatonin prevents changes in microsomal membrane fluidity during induced lipid peroxidation. *FEBS Letters*, 1997.

[125] MA Pappolla, Y-J Chyan, B Poeggeler, B Frangione, G Wilson, J Ghiso, and RJ Reiter. An assessment of the antioxidant and the antiamyloidogenic properties of melatonin: Implications for Alzheimer's disease. *Journal of Neural Transmission*, 107(2):203–231, 2000.

[126] Fernando Antunes, L. Ross C. Barclay, Keith U. Ingold, Mary King, James Q. Norris, J. C. Scaiano, and Fengde Xi. On the antioxidant activity of melatonin. *Free Radical Biology and Medicine*, 1999.

[127] A Choucair, M Chakrapani, B Chakravarthy, J Katsaras, and LJ Johnston. Preferential accumulation of Aβ (1-42) on gel phase domains of lipid bilayers: An AFM and fluorescence study. *Biochimica et Biophysica Acta (BBA) - Biomembranes*, 1768(1):146–154, 2007.

[128] C M Yip, E a Elton, a a Darabie, M R Morrison, and J McLaurin. Cholesterol, a modulator of membrane-associated A beta- fibrillogenesis and neurotoxicity. *Journal of Molecular Biology*, 311(4):723–734, 2001.

[129] Andrey Y Abramov, Maksim Ionov, Evgeny Pavlov, and Michael R Duchen. Membrane cholesterol content plays a key role in the neurotoxicity of β-amyloid: Implications for Alzheimer's disease. *Aging Cell*, 10(4):595–603, 2011.

[130] Elizabeth Drolle, Ravi M Gaikwad, and Zoya Leonenko. Nanoscale electrostatic domains in cholesterol-laden lipid membranes create a target for amyloid binding. *Biophysical Journal*, 103(4):L27–L29, 2012.

[131] Alexandra M. Nicholson, D. Nicole Riherd Methner, and Adriana Ferreira. Membrane cholesterol modulates β-amyloid-dependent Tau cleavage by inducing changes in the membrane content and localization of N-methyl-D-aspartic acid receptors. *Journal of Biological Chemistry*, 286(2):976–986, 2011.

[132] Nelson Arispe and Michael Doh. Plasma membrane cholesterol controls the cytotoxicity of Alzheimer's disease AbetaP (1-40) and (1-42) peptides. *The FASEB Journal*, 16(12):1526–1536, 2002.

[133] Cristina Cecchi, Daniela Nichino, Mariagioia Zampagni, Caterina Bernacchioni, Elisa Evangelisti, Anna Pensalfini, Gianfranco Liguri, Alessandra Gliozzi, Massimo Stefani, and Annalisa Relini. A protective role for lipid raft cholesterol against amyloid-induced membrane damage in human neuroblastoma cells. *Biochimica et Biophysica Acta (BBA) - Biomembranes*, 1788(10):2204–16, 2009.

[134] Elizabeth Drolle. Biophysical studies of lipid membranes and their interactions with amyloid peptides. 2015.

[135] Zaven S Khachaturian. Diagnosis of Alzheimer's disease. *Archives of Neurology*, 42(11):1097–1105, 1985.

[136] Fuyuki Kametani and Masato Hasegawa. Reconsideration of amyloid hypothesis and tau hypothesis in Alzheimer's disease. *Frontiers in Neuroscience*, 12:25, 2018.

[137] George G Glenner and Caine W Wong. Alzheimer's disease: Initial report of the purification and characterization of a novel cerebrovascular amyloid protein. *Biochemical and Biophysical Research Communications*, 120(3):885–890, 1984.

[138] Mun'delanji Vestergaard, Tsutomu Hamada, and Masahiro Takagi. Using model membranes for the study of amyloid beta: Lipid interactions and neurotoxicity. *Biotechnology and Bioengineering*, 99(4):753–763, 2008.

[139] Kenji Sasahara, Kenichi Morigaki, and Kyoko Shinya. Effects of membrane interaction and aggregation of amyloid β-peptide on lipid mobility and membrane domain structure. *Physical Chemistry Chemical Physics*, 15(23):8929–8939, 2013.

[140] Nancy Maurya and Nupur Rani Agarwal. Neuro-pathological Implications of β-Amyloid Protein: An Update. *Proceedings of the Nature Research Society*, 2:02006, 2018.

[141] Robert M Koffie, Melanie Meyer-Luehmann, Tadafumi Hashimoto, Kenneth W Adams, Matthew L Mielke, Monica Garcia-Alloza, Kristina D Micheva, Stephen J Smith, M Leo Kim, Virginia M Lee, et al. Oligomeric amyloid β associates with postsynaptic densities and correlates with excitatory synapse loss near senile plaques. *Proceedings of the National Academy of Sciences*, 106(10):4012–4017, 2009.

[142] Benedikt Beckert, Amparo Acker-Palmer, and Walter Volknandt. Aβ42 oligomers impair the bioenergetic activity in hippocampal synaptosomes derived from app-ko mice. *Biological Chemistry*, 399(5):453–465, 2018.

[143] David Siniscalco, Grégory Francius, Mounir Tarek, Semiha Kevser Bali, Olivier Laprévote, Catherine Malaplate, Thierry Oster, Lynn Pauron, and Fabienne Quilès. Molecular insights for Alzheimer's disease: An unexplored storyline on the nanoscale

impact of nascent Aβ1–42 toward the lipid membrane. *ACS Applied Materials & Interfaces*, 15(14):17507–17517, 2023.

[144] Erik S Musiek and David M Holtzman. Three dimensions of the amyloid hypothesis: Time, space and'wingmen'. *Nature Neuroscience*, 18(6):800–806, 2015.

[145] Zeinab Breijyeh and Rafik Karaman. Comprehensive review on Alzheimer's disease: Causes and treatment. *Molecules*, 25(24):5789, 2020.

[146] Elizabeth Drolle, Norbert Kučerka, Youngjik Choi, John Katsaras, and Zoya Leonenko. Melatonin counteracts cholesterol's effects on lipid membrane structure. *Biophysical Journal*, 104(2):182a, 2013.

[147] M Ewald, S Henry, É Lambert, C Feuillie, C Bobo, C Cullin, S Lecomte, and M Molinari. High speed atomic force microscopy to investigate the interactions between toxic Aβ 1-42 peptides and model membranes in real time: Impact of the membrane composition. *Nanoscale*, 11(15):7229–7238, 2019.

[148] Thomas L Williams, Benjamin RG Johnson, Brigita Urbanc, A Toby A Jenkins, Simon DA Connell, and Louise C Serpell. Aβ42 oligomers, but not fibrils, simultaneously bind to and cause damage to ganglioside-containing lipid membranes. *Biochemical Journal*, 439(1):67–77, 2011.

[149] Claudio Canale, Reinier Oropesa-Nuñez, Alberto Diaspro, and Silvia Dante. Amyloid and membrane complexity: The toxic interplay revealed by AFM. In *Seminars in Cell & Developmental Biology*, volume 73, pages 82–94. Elsevier, 2018.

[150] John H Viles. Imaging amyloid-β membrane interactions: Ion-channel pores and lipid-bilayer permeability in Alzheimer's disease. *Angewandte Chemie*, page e202215785, 2023.

[151] Kathleen A Burke, Elizabeth A Yates, and Justin Legleiter. Biophysical insights into how surfaces, including lipid membranes, modulate protein aggregation related to neurodegeneration. *Frontiers in Neurology*, 4:17, 2013.

[152] Siddhartha Banerjee, Mohtadin Hashemi, Karen Zagorski, and Yuri L Lyubchenko. Cholesterol in membranes facilitates aggregation of amyloid β protein at physiologically relevant concentrations. *ACS Chemical Neuroscience*, 12(3):506–516, 2021.

[153] Jack Robinson, Nirod Kumar Sarangi, and Tia E Keyes. Role of phosphatidylserine in amyloid-beta oligomerization at asymmetric phospholipid bilayers. *Physical Chemistry Chemical Physics*, 25(11):7648–7661, 2023.

[154] Yu-Chia Kao, Pei-Chuan Ho, Yuan-Kun Tu, I-Ming Jou, and Kuen-Jer Tsai. Lipids and Alzheimer's disease. *International Journal of Molecular Sciences*, 21(4):1505, 2020.

[155] Pradeep K Srivastava. *Elementary biophysics: An introduction*. Alpha Science Int'l Ltd., 2005.

[156] Stéphanie Andrade, Joana Angélica Loureiro, and Maria Carmo Pereira. The role of amyloid β-biomembrane interactions in the pathogenesis of Alzheimer's disease: Insights from liposomes as membrane models. *ChemPhysChem*, 22(15):1547–1565, 2021.

[157] ZV Leonenko, A Carnini, and DT Cramb. Supported planar bilayer formation by vesicle fusion: The interaction of phospholipid vesicles with surfaces and the effect of gramicidin on bilayer properties using atomic force microscopy. *Biochimica et Biophysica Acta (BBA) - Biomembranes*, 1509(1-2):131–147, 2000.

[158] CS Shida, AM dL Castrucci, and MT Lamy-Freund. High melatonin solubility in aqueous medium. *Journal of Pineal Research*, 16(4):198–201, 1994.

[159] Sanjai Kumar Pachahara, Nitin Chaudhary, Chilukuri Subbalakshmi, and Ramakrishnan Nagaraj. Hexafluoroisopropanol induces self-assembly of β-amyloid peptides into highly ordered nanostructures. *Journal of Peptide Science*, 18(4):233–241, 2012.

[160] Brenda Yasie Lee, Simon James Attwood, Stephen Turnbull, and Zoya Leonenko. Effect of varying concentrations of docosahexaenoic acid on amyloid beta (1–42) aggregation: An atomic force microscopy study. *Molecules*, 23(12):3089, 2018.

[161] Elizabeth Drolle, WFD Bennett, K Hammond, Edward Lyman, Mikko Karttunen, and Zoya Leonenko. Molecular dynamics simulations and kelvin probe force microscopy to study of cholesterol-induced electrostatic nanodomains in complex lipid mixtures. *Soft Matter*, 13(2):355–362, 2017.

[162] Karim El Kirat, Sandrine Morandat, and Yves F Dufrêne. Nanoscale analysis of supported lipid bilayers using atomic force microscopy. *Biochimica et Biophysica Acta (BBA) - Biomembranes*, 1798(4):750–765, 2010.

[163] Attila Bonyár. Label-free nucleic acid biosensing using nanomaterial-based localized surface plasmon resonance imaging: A review. *ACS Applied Nano Materials*, 3(9):8506–8521, 2020.

[164] Andrea Miti, Sophie Thamm, Philipp Müller, Andrea Csáki, Wolfgang Fritzsche, and Giampaolo Zuccheri. A mirna biosensor based on localized surface plasmon resonance enhanced by surface-bound hybridization chain reaction. *Biosensors and Bioelectronics*, 167:112465, 2020.

[165] Fatemeh Yaghubi, Mehdi Zeinoddini, Ali Reza Saeedinia, Azadeh Azizi, and Afshin Samimi Nemati. Design of localized surface plasmon resonance (LSPR) biosensor for immunodiagnostic of E. coli O157: H7 using gold nanoparticles conjugated to the chicken antibody. *Plasmonics*, 15(5):1481–1487, 2020.

[166] Rayssa Helena Arruda Pereira, Wanderson Juvêncio Keijok, Adilson Ribeiro Prado, Jairo Pinto de Oliveira, and Marco Cesar Cunegundes Guimarães. Rapid and sensitive detection of ochratoxin a using antibody-conjugated gold nanoparticles based on localized surface plasmon resonance. *Toxicon*, 199:139–144, 2021.

[167] Mir Hadi Jazayeri, Tayebe Aghaie, Reza Nedaeinia, Mostafa Manian, and Hamid Nickho. Rapid noninvasive detection of bladder cancer using survivin antibody-conjugated gold nanoparticles (GNPs) based on localized surface plasmon resonance (LSPR). *Cancer Immunology, Immunotherapy*, 69(9):1833–1840, 2020.

[168] Luigi Zeni, Chiara Perri, Nunzio Cennamo, Francesco Arcadio, Girolamo D'Agostino, Mario Salmona, Marten Beeg, and Marco Gobbi. A portable optical-fibre-based

surface plasmon resonance biosensor for the detection of therapeutic antibodies in human serum. *Scientific Reports*, 10(1):1–9, 2020.

[169] Seongjae Jo, Wonseok Lee, Joohyung Park, Woong Kim, Woochang Kim, Gyudo Lee, Heon-Jeong Lee, Junghwa Hong, and Jinsung Park. Localized surface plasmon resonance aptasensor for the highly sensitive direct detection of cortisol in human saliva. *Sensors and Actuators B: Chemical*, 304:127424, 2020.

[170] Jiřı Homola, Sinclair S Yee, and Günter Gauglitz. Surface plasmon resonance sensors. *Sensors and Actuators B: Chemical*, 54(1-2):3–15, 1999.

[171] Linda S Jung, Charles T Campbell, Timothy M Chinowsky, Mimi N Mar, and Sinclair S Yee. Quantitative interpretation of the response of surface plasmon resonance sensors to adsorbed films. *Langmuir*, 14(19):5636–5648, 1998.

[172] Shon Schmidt, Jonas Flueckiger, WenXuan Wu, Samantha M Grist, Sahba Talebi Fard, Valentina Donzella, Pakapreud Khumwan, Emily R Thompson, Qian Wang, Pavel Kulik, et al. Improving the performance of silicon photonic rings, disks, and bragg gratings for use in label-free biosensing. In *Biosensing and Nanomedicine VII*, volume 9166, page 91660M. International Society for Optics and Photonics, 2014.

[173] Malin Ardhammar, Per Lincoln, and Bengt Nordén. Invisible liposomes: Refractive index matching with sucrose enables flow dichroism assessment of peptide orientation in lipid vesicle membrane. *Proceedings of the National Academy of Sciences*, 99(24):15313–15317, 2002.

[174] Michael C Howland, Alan W Szmodis, Babak Sanii, and Atul N Parikh. Characterization of physical properties of supported phospholipid membranes using imaging ellipsometry at optical wavelengths. *Biophysical Journal*, 92(4):1306–1317, 2007.

[175] Zdzislaw Salamon and Gordon Tollin. Optical anisotropy in lipid bilayer membranes: Coupled plasmon-waveguide resonance measurements of molecular orientation, polarizability, and shape. *Biophysical Journal*, 80(3):1557–1567, 2001.

[176] Alireza Mashaghi, Marcus Swann, Jonathan Popplewell, Marcus Textor, and Erik Reimhult. Optical anisotropy of supported lipid structures probed by waveguide spectroscopy and its application to study of supported lipid bilayer formation kinetics. *Analytical Chemistry*, 80(10):3666–3676, 2008.

[177] Petteri Parkkila, Mohamed Elderdfi, Alex Bunker, and Tapani Viitala. Biophysical characterization of supported lipid bilayers using parallel dual-wavelength surface plasmon resonance and quartz crystal microbalance measurements. *Langmuir*, 34(27):8081–8091, 2018.

[178] Huaying Zhao, Patrick H Brown, and Peter Schuck. On the distribution of protein refractive index increments. *Biophysical Journal*, 100(9):2309–2317, 2011.

[179] Chan-Yuan Tan and Yao-Xiong Huang. Dependence of refractive index on concentration and temperature in electrolyte solution, polar solution, nonpolar solution, and protein solution. *Journal of Chemical & Engineering Data*, 60(10):2827–2833, 2015.

[180] Allison Dickey and Roland Faller. Examining the contributions of lipid shape and headgroup charge on bilayer behavior. *Biophysical Journal*, 95(6):2636–2646, 2008.

[181] Ronak Y Patel and Petety V Balaji. Characterization of the conformational and orientational dynamics of ganglioside gm1 in a dipalmitoylphosphatidylcholine bilayer by molecular dynamics simulations. *Biochimica et Biophysica Acta (BBA) - Biomembranes*, 1768(6):1628–1640, 2007.

[182] Kiryl Zhaliazka and Dmitry Kurouski. Nanoscale characterization of parallel and antiparallel β-sheet amyloid beta 1–42 aggregates. *ACS Chemical Neuroscience*, 13(19):2813–2820, 2022.

[183] Bradley Moores, Elizabeth Drolle, Simon J Attwood, Janet Simons, and Zoya Leonenko. Effect of surfaces on amyloid fibril formation. *PLoS One*, 6(10):e25954, 2011.

[184] Michael P Murphy and Harry LeVine. Alzheimer's disease and the amyloid-beta peptide. *Journal of Alzheimer's Disease*, 2(2):75–80, 2000.

[185] John Hardy and David Allsop. Amyloid deposition as the central event in the aetiology of Alzheimer's disease. *Trends in Pharmacological Sciences*, 12:383–388, 1991.

[186] Miguel A Pappolla, Melisa Sos, Rawhi A Omar, Roger J Bick, Diane LM Hickson-Bick, Russel J Reiter, Spiros Efthimiopoulos, and Nickolaos K Robakis. Melatonin prevents death of neuroblastoma cells exposed to the Alzheimer amyloid peptide. *Journal of Neuroscience*, 17(5):1683–1690, 1997.

[187] Russel J Reiter. Oxidative damage in the central nervous system: Protection by melatonin. *Progress in Neurobiology*, 56(3):359–384, 1998.

[188] Naoki Saigo, Kayano Izumi, and Ryuji Kawano. Electrophysiological analysis of antimicrobial peptides in diverse species. *Acs Omega*, 4(8):13124–13130, 2019.

[189] S Jonathan Singer and Garth L Nicolson. The fluid mosaic model of the structure of cell membranes: Cell membranes are viewed as two-dimensional solutions of oriented globular proteins and lipids. *Science*, 175(4023):720–731, 1972.

[190] Rixt F Riemersma-van Der Lek, Dick F Swaab, Jos Twisk, Elly M Hol, Witte JG Hoogendijk, and Eus JW Van Someren. Effect of bright light and melatonin on cognitive and noncognitive function in elderly residents of group care facilities: A randomized controlled trial. *Jama*, 299(22):2642–2655, 2008.

[191] Mathias Winterhalter. Black lipid membranes. *Current Opinion in Colloid & Interface Science*, 5(3-4):250–255, 2000.

[192] Joon Lee, Young Hun Kim, Fernando T. Arce, Alan L Gillman, Hyunbum Jang, Bruce L Kagan, Ruth Nussinov, Jerry Yang, and Ratnesh Lal. Amyloid β ion channels in a membrane comprising brain total lipid extracts. *ACS Chemical Neuroscience*, 8(6):1348–1357, 2017.

[193] Olaf S Andersen and Roger E Koeppe. Bilayer thickness and membrane protein function: An energetic perspective. *Annual Review of Biophysics and Biomolecular Structure*, 36:107–130, 2007.

[194] Kyle J Korshavn, Anirban Bhunia, Mi Hee Lim, and Ayyalusamy Ramamoorthy. Amyloid-β adopts a conserved, partially folded structure upon binding to zwitterionic lipid bilayers prior to amyloid formation. *Chemical Communications*, 52(5):882–885, 2016.

[195] Barbara Mroczko, Magdalena Groblewska, Ala Litman-Zawadzka, Johannes Kornhuber, and Piotr Lewczuk. Cellular receptors of amyloid β oligomers (AβOs) in Alzheimer's disease. *International Journal of Molecular Sciences*, 19(7):1884, 2018.

[196] Rana Ashkar, Hassina Bilheux, Heliosa Bordallo, Robert Briber, David JE Callaway, Xiaolin Cheng, X-Q Chu, Joseph E Curtis, Mark Dadmun, Paul Fenimore, et al. Neutron scattering in the biological sciences: Progress and prospects. *Acta Crystallographica Section D: Structural Biology*, 74(12):1129–1168, 2018.

[197] Varley F Sears. Neutron scattering lengths and cross sections. *Neutron News*, 3(3):26–37, 1992.

[198] Minoru Nakano, Masakazu Fukuda, Takayuki Kudo, Hitoshi Endo, and Tetsurou Handa. Determination of interbilayer and transbilayer lipid transfers by time-resolved small-angle neutron scattering. *Physical Review Letters*, 98(23):238101, 2007.

[199] Jianjun Pan, Frederick A Heberle, Robin S Petruzielo, and John Katsaras. Using small-angle neutron scattering to detect nanoscopic lipid domains. *Chemistry and Physics of Lipids*, 170:19–32, 2013.

[200] Jonathan D Nickels, Xiaolin Cheng, Barmak Mostofian, Christopher Stanley, Benjamin Lindner, Frederick A Heberle, Stefania Perticaroli, Mikhail Feygenson, Takeshi Egami, Robert F Standaert, et al. Mechanical properties of nanoscopic lipid domains. *Journal of the American Chemical Society*, 137(50):15772–15780, 2015.

[201] Jonathan D Nickels, Sneha Chatterjee, Christopher B Stanley, Shuo Qian, Xiaolin Cheng, Dean AA Myles, Robert F Standaert, James G Elkins, and John Katsaras. The in vivo structure of biological membranes and evidence for lipid domains. *PLoS Biology*, 15(5):e2002214, 2017.

[202] Martin Karplus and Gregory A Petsko. Molecular dynamics simulations in biology. *Nature*, 347(6294):631–639, 1990.

[203] Richard M Venable, Frank LH Brown, and Richard W Pastor. Mechanical properties of lipid bilayers from molecular dynamics simulation. *Chemistry and Physics of Lipids*, 192:60–74, 2015.

[204] Xiaohong Zhuang, Judah R Makover, Wonpil Im, and Jeffery B Klauda. A systematic molecular dynamics simulation study of temperature dependent bilayer structural properties. *Biochimica et Biophysica Acta (BBA) - Biomembranes*, 1838(10):2520–2529, 2014.

[205] Ganesh Shahane, Wei Ding, Michail Palaiokostas, and Mario Orsi. Physical properties of model biological lipid bilayers: Insights from all-atom molecular dynamics simulations. *Journal of Molecular Modeling*, 25:1–13, 2019.

[206] Jacob J Kinnun, Haden L Scott, Dima Bolmatov, C Patrick Collier, Timothy R Charlton, and John Katsaras. Biophysical studies of lipid nanodomains using different physical characterization techniques. *Biophysical Journal*, 2023.

[207] Giovanna Fragneto-Cusani. Neutron reflectivity at the solid/liquid interface: Examples of applications in biophysics. *Journal of Physics: Condensed Matter*, 13(21):4973, 2001.

[208] Alessandra Luchini, Samantha Micciulla, Giacomo Corucci, Krishna Chaithanya Batchu, Andreas Santamaria, Valerie Laux, Tamim Darwish, Robert A Russell, Michel Thepaut, Isabelle Bally, et al. Lipid bilayer degradation induced by sars-cov-2 spike protein as revealed by neutron reflectometry. *Scientific Reports*, 11(1):14867, 2021.

[209] Silvia Dante, Thomas Hauß, Roland Steitz, Claudio Canale, and Norbert A Dencher. Nanoscale structural and mechanical effects of beta-amyloid (1–42) on polymer cushioned membranes: A combined study by neutron reflectometry and AFM Force Spectroscopy. *Biochimica et Biophysica Acta (BBA) - Biomembranes*, 1808(11):2646–2655, 2011.

[210] Toshio Ando. High-speed atomic force microscopy. *Current opinion in chemical biology*, 51:105–112, 2019.

[211] Ignacio Casuso, Jonathan Khao, Mohamed Chami, Perrine Paul-Gilloteaux, Mohamed Husain, Jean-Pierre Duneau, Henning Stahlberg, James N Sturgis, and Simon Scheuring. Characterization of the motion of membrane proteins using high-speed atomic force microscopy. *Nature Nanotechnology*, 7(8):525–529, 2012.

APPENDICES

Appendix A

Neutron Scattering and Molecular Dynamics to Study Complex Lipid Model Membranes

A.1 Overview

This project comprises two studies conducted in collaboration with two research groups: the John Katsaras Group at Oak Ridge National Laboratory and the Maikel C. Rheinstädter Group at McMaster University. The objective of this project is to explore lipid dynamics and membrane domain formations in complex neuronal model membranes that mimic both the healthy and early diseased states of Alzheimer's disease.

For the neutron scattering study, the design was formulated in collaboration with Dr. Morgan Robinson (who was a PhD student at the time) from our home lab and Dr. John Katsaras. Dr. Katsaras' Postdoc Fellow, Dr. Dmitry Bolmatov, trained M. Robinson in the experimental methods, and M. Robinson proceeded with data collection. While I led the experimental design, I could not participate in the data collection due to visa issues. M. Robinson achieved preliminary data analysis, and both he and I will continue to refine the analysis.

For the molecular dynamics simulation study, it was conceived in collaboration with Dr. Maikel C. Rheinstädter and his student Dr. Sebastian Himbert (a PhD student at that time). The same lipid membrane systems used in the neutron scattering study were employed here. I utilized CHARMM-GUI to design the model, while S. Himbert executed the simulation using Gromacs. Data collection has been completed, and data analysis is currently underway. Preliminary results, analyzed by S. Himbert, are available and presented in the subsequent sections.

A.2 Introduction to Neutron Scattering

Neutron scattering is a powerful experimental technique employed in the study of a vast range of materials, spanning from liquids to solids [196]. When neutrons are directed at a material, they scatter off nuclei and unpaired electrons, producing a scattering pattern that provides crucial information about the atomic and molecular structures, as well as the dynamics within the material [197].

Among the various techniques of neutron scattering, Small Angle Neutron Scattering (SANS) is particularly significant. SANS investigates structures at the nanoscale, typically ranging from 5 to 100 nanometers [199]. This method is especially suited to studying large molecular structures, inhomogeneities, and aggregates in various biological materials. By analyzing the scattering patterns at small angles, researchers can extract a wealth of information about size, shape, and orientation of these nanostructures. The non-destructive nature of neutrons and their deep penetration into matter makes SANS an invaluable tool in the world of nanoscale science and research. For example, Drolle *et al.* used SANS to successfully study the bilayer thickness change induced by cholesterol and melatonin of the pure DPPC or DOPC unilamellar vesicles in 2013 [24].

In the realm of neutron scattering, particularly when studying lipid domain structures in liposome solutions composed with more than one lipid species, scattering length density (SLD) and contrast matching play pivotal roles [197]. The SLD is a measure of how neutrons are scattered by a particular volume of a material. For liposomes, which are essentially lipid bilayer vesicles encapsulating a water-based core, the SLD provides crucial

information about the distribution and arrangement of the lipid molecules in the bilayer. Different components of the liposome, such as the lipid head groups, tails, and the aqueous core, have distinct SLDs. As a result, they would appear as different contrast against the background solvent. Contrast matching is employed to make the sample "invisible" to neutron scattering by matching the scattering length density (SLD) of the component to that of the surrounding solvent [198, 196].

When studying liposome solutions, this principle is often applied to make the entire liposome match the SLD of the background solvent, which could be a mixture of water and D_2O [199]. At high temperatures, where lipids are in a fully mixed state, the liposome can be matched in contrast to the solvent, essentially making it invisible in the SANS measurement. This is achieved by adjusting the ratio of deuterated lipids versus the non-deuterated lipids, as well as adjusting the ratio of H_2O to D_2O, making the SLDs of the liposomes to match that of the solvent. However, as the solution is cooled, different lipid species undergo phase transitions at different temperatures. As a result, lipid domains, representing regions of different lipid phases, begin to form within the liposome. Given that these domains have distinct SLDs from the rest of the liposome and the solvent, the previously achieved contrast matching condition is disrupted.

The emergence of these lipid domains that no longer match the surrounding solvent in terms of SLD leads to an increase in scattering intensity. This change is manifested as a peak in the SANS spectrum, indicating the formation of structures (domains) within the liposomes. The position, width, and intensity of this peak can provide valuable insights into the size, shape, and distribution of these lipid domains [199].

Using the unique contrast matching technique, Nickles *et al.* successfully identified the formation of $\approx$ 13 nm domains within a unilamellar vesicle system, with vesicle diameter of 60 nm. This system was designed to mimic the mammalian plasma membrane using a lipid model composed of POPC, DSPC, and cholesterol [200]. Apart from the model lipid systems, SANS can also be applied to study cell membranes in vivo [201]. The same research group managed to measure the domain structure on B. subtilis cell membrane by carefully adjusting contrast conditions, as well they managed to measure the hydrophobic thickness of the cell membrane.

These applications of SANS on biological membranes studies provide well-developed approaches in measuring the phase behaviour of unilamellar system. My collaborative research with Dr. Morgan Robinson was designed using the well-established contrast matching method to investigate the phase separation that results in domain formation on the complex neuronal cell membrane models: HM and EDM. The experiments were conducted in collaboration with the John Katsaras group at Oak Ridge National Laboratory located in USA. Details on experiment set up and outcomes will be discussed later.

A.3 Introduction to Molecular Dynamics

In conjunction with the SANS technique to study the membrane phase behaviour of the complex models, molecular dynamic (MD) simulation was utilized to provide details on the composition of the membrane domains.

MD simulations have emerged as indispensable tools in the detailed exploration of a myriad of biological systems at the molecular level, one of the most notable being lipid membranes. MD simulates the physical movements of atoms and molecules in a system over time, abiding by the laws of classical mechanics. By using force fields – mathematical functions that describe the interactions and energy between atoms – the simulations provide a temporal evolution of the system, offering insights into molecular trajectories, structural shifts, and dynamic interactions [202].

In the application for lipid membrane studies, MD simulations have been utilized to investigate lipid bilayer organization, dynamics, and function [203]. By varying temperature and lipid composition in simulations, researchers can explore phase transitions, domain formations, and the emergence of ordered and disordered phases in lipid bilayer membranes [204]. MD can also provide details about membrane thickness, area per lipid [161], and the lateral pressure of lipid molecules [205], which are vital parameters defining membrane fluidity.

A.4 Experiments

Both the NS and the MD simulation experiments used the same lipid model membranes that mimic the healthy (HM) and the early diseased (EDM) state of AD as shown in Table A.1 [2]. Two temperatures: 22 °C and 54 °C were involved in these studies.

	Lipid components (weight ratio)				
Lipid Models	DPPC	POPC	Cholesterol	SM	GM1
Healthy Model (HM)	37	37	10	10	6
Early Diseased Model (EDM)	39	39	10	10	2

Table A.1: **Lipid Compositions of the Lipid Model Membranes** mimicking different disease states of neuronal cell membranes in AD: HM, and EDM membranes. The ratios are shown by weight. Adapted from Drolle *et al.*, 2017 [2].

A.4.1 Neutron Scattering

** This section is fully rewritten from the experiment details provided by M. Robinson. **

Lipids were combined in chloroform according to the ratios specified in Table A.1. The chloroform was allowed to evaporate under dry nitrogen for 2 hours and was subsequently placed in a vacuum chamber overnight to eliminate any remaining chloroform, resulting in a dry lipid film. This film was then rehydrated in a D_2O/H_2O mixture at an approximate ratio of 61:39, ensuring the vesicle's contrast matched the background.

Neutron beam data, both transmitted and scattered, were collected for each sample condition and controls using the EQ-SANS Diffractometer at the Spallation Neutron Source (SNS) in the Oak Ridge National Laboratory. Data for the Porasil B calibration standard and background banjo cells (cuvettes) for calibration were also collected. Low Q data was obtained using detector settings at 8m 8A in pure D_2O for both membrane models. High Q data were captured with detector settings at 2.5m 2.5A in approximately 60.5% and 61.8% D_2O for EDM and HM, respectively.

A.4.2 Molecular Dynamics Simulation

Lipid membrane models, as detailed in Table A.1, were employed to create models using CHARMM-GUI. In each lipid model, DPG1 substituted for GM1, and DPSM replaced SM during the simulation model construction. Each leaflet of the bilayer incorporated 1,000 lipid molecules. The simulations were executed using Gromacs.

A.5 Preliminary Results

** The preliminary results of MD simulation were provided by S. Himbert. **

The NS data require further processing to accurately display the results. What follows are representative preliminary results from the MD simulation. Since the analysis is not yet complete, only the results on simulations for HM and EDM membranes at 54 °C are shown here.

Figures A.1 and A.2 show the rendering results for the healthy and the early diseased model membranes, respectively. Figures A.3 and A.4 show the side view of the membrane renderings.

Figure A.5 include the density profiles of the two model membranes. For both of the HM and EDM membranes, the difference in membrane thickness between DPG1 and other lipids is ≈1.5 nm.

Figures A.6 and A.7 show the thickness maps of upper and lower leaflets for both HM and EDM membranes. This thickness profile was interpolated using the griddata function. The height profile was averaged over 1 microsecond. The HM membrane shows larger and more frequent thickness variations of both leaflet, while the EDM membrane shows a flatter surface with only few thicker areas.

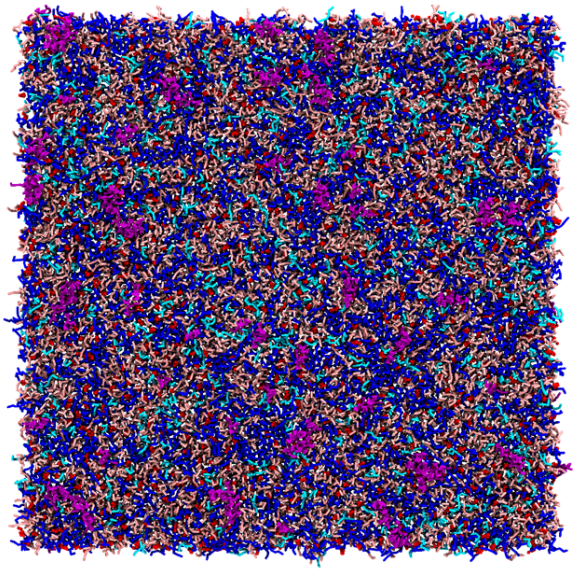


Figure A.1: Rendering of the HM membrane that gives lateral arrangements of lipid molecules.

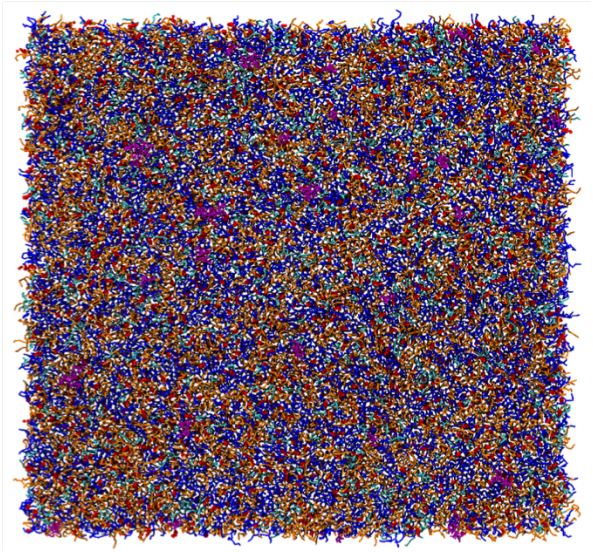


Figure A.2: Rendering of the EDM membrane that gives lateral arrangements of lipid molecules.

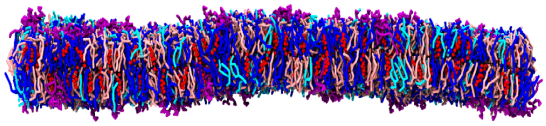


Figure A.3: A side view on the rendering of the HM membrane.

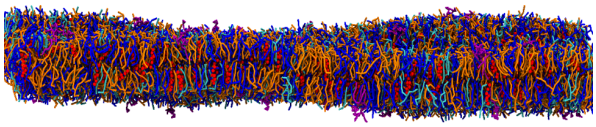


Figure A.4: A side view on the rendering of the EDM membrane.

A.6 Next Steps

Data analysis for the NS experiment needs to continue, as does the MD simulation for both HM and EDM membranes at 22 ∘C. We expect that the outcomes will provide insights into membrane phase separation/domain formation as the temperature decreases for both lipid model membranes, as evidenced by the NS data. Additionally, the MD data should reveal information about the composition of the domain structure and the organization of

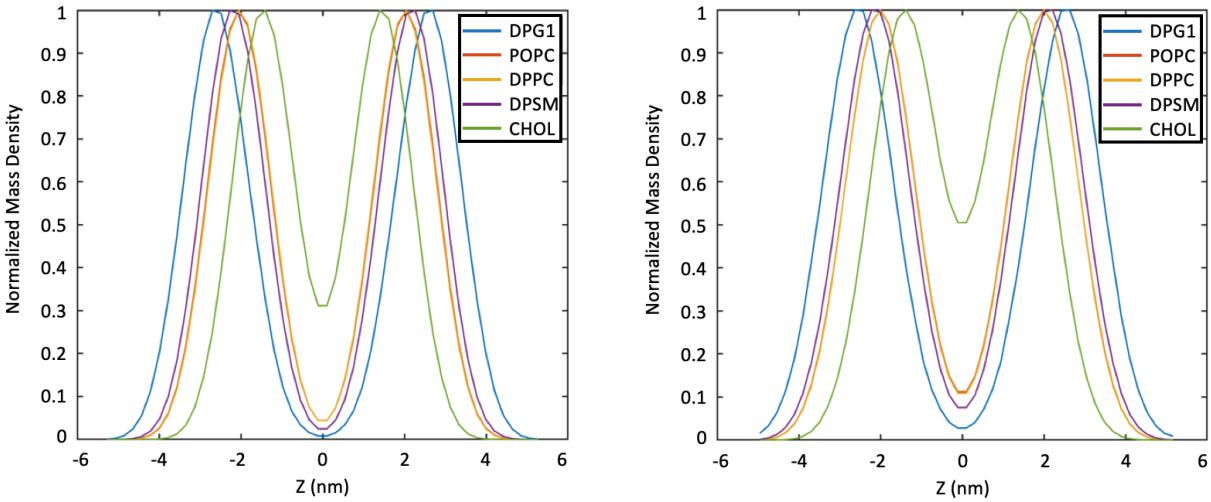


Figure A.5: An illustration of the normalized mass density profile for the each composite lipid for (Left) HM, and (Right) EDM. The symmetric peaks indicate the location of the PO_4 groups (DPPC, POPC and DPSM) as well as the GM_1 bead from DPG1. The location of the peaks can be considered to be a measure of the lipid dependent membrane thickness.

lipids within the membrane system.

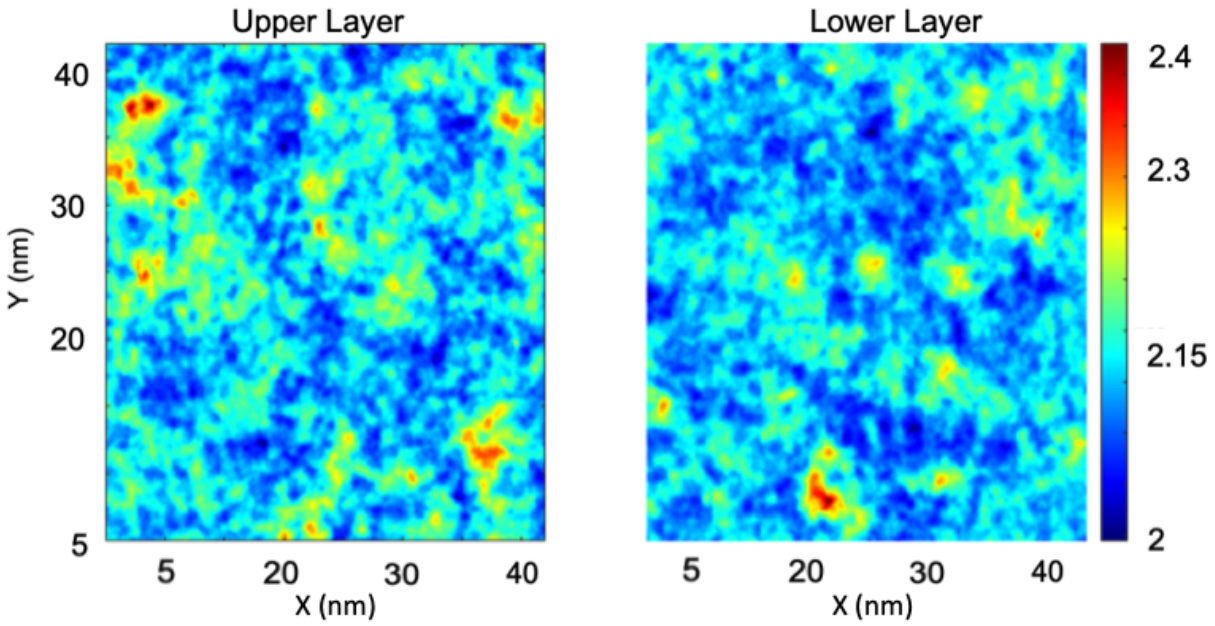


Figure A.6: Thickness maps for the membrane patch of HM. The upper and lower leaflet were separated at each time-step. The highest and lowest point was determined for each lipid and the membrane thickness at every point was calculated by subtracting both values.

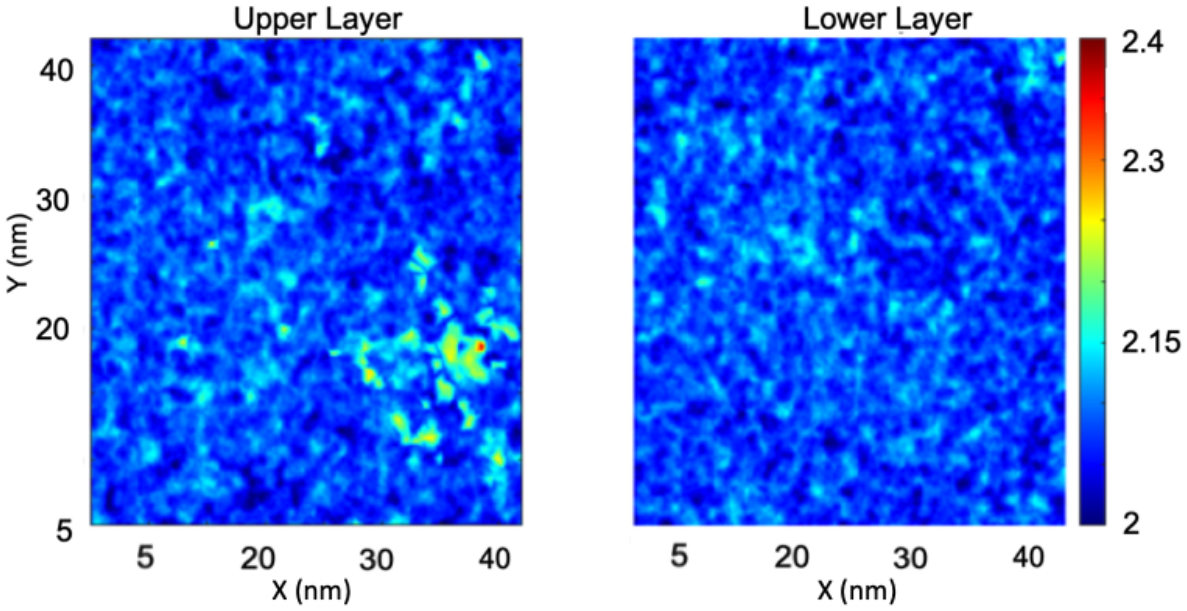


Figure A.7: Thickness maps for the membrane patch of EDM. The upper and lower leaflet were separated at each time-step. The highest and lowest point was determined for each lipid and the membrane thickness at every point was calculated by subtracting both values

Appendix B

Neutron Reflectivity to Study Simple Model Lipid Membranes

B.1 Overview

This project was developed in collaboration with Dr. Giovanna Fragneto and her PhD student, Giacomo Corruci, at the Institut Laue-Langevin (ILL) in France. The goal was to study the interaction of amyloid with a lipid membrane model composed of DPPC, POPC, and cholesterol. We conducted experiments at two temperatures: 22 $°C$ and 37 $°C$. Data collection was completed by G. Corruci at the ILL, and the analysis was carried out by both G. Corruci and myself. Preliminary results are available and have been included in the text here.

B.2 Introduction to Neutron Reflectivity

While both neutron scattering (NS) and neutron reflectivity (NR) techniques utilize the unique properties of neutrons to study materials, neutron reflectivity examines the neutrons reflected from the sample, rather than the scattered neutrons as detailed in the

neutron scattering section. For the successful detection of reflected neutrons from a sample, it typically needs to be supported on a solid substrate. Silicon-based substrates are commonly used because of their advanced surface coating techniques [207]. However, while the vertical sensitivity of the NR technique is exceptional, reaching detection limits of 5 $\mathring{A}$ [206], its lateral sensitivity is not as pronounced. As a result, NR is particularly sensitive to depth-related changes in lipid membrane systems, such as changes in membrane thickness, molecule binding to the membrane surface, molecule transport across the membrane, and lipid rearrangements in asymmetric membranes, among others [207, 206]. Luchini *et al.* recently reported a study on the interaction of SARS-CoV-2 spike proteins with a synthetic lipid membrane (POPS:POPC) and a mixture of extracted lipids from the yeast *Picha pastoris* combined with cholesterol (PC:PS:PE:chol), which resulted in a reduction of membrane coverage [208]. Additionally, Dante *et al.* conducted a study on Aβ peptide interactions with membranes formed from pure POPC or a mixture of POPC/POPS (with one deuterated acyl chain on all lipids) and observed membrane penetration by the peptide [209].

Similar to NS, the contrast between the sample membrane and the background plays a pivotal role in detecting the signal. In NR, three components of the experimental system contribute to this contrast: the buffer, the sample (or membrane), and the substrate. Achieving contrast match follows a process analogous to that described in the NS section. A unique aspect of the NR system is that both the buffer solution and the substrate must have matched contrasts to obtain a reflectivity profile solely from the membrane. This approach facilitates the determination of a layer's composition based on its scattering length density (SLD). As articulated by Fragneto-Cusani (2001), adjusting the H and D ratio in the buffer alters its SLD. Typically, an NR study incorporates four contrasts, as elucidated by Fragneto-Cusani and summarized in Table B.1 [207].

B.3 Experiment

Figure B.1 displays a schematic of the experimental setup. The incident neutron beam illuminates the silicon/membrane interface from the silicon side and is reflected twice at

Contrast Group	SLD ($10^{-6}\mathring{A}^{-2}$)	H_2O	D_2O
H_2O (Pure H_2O)	-0.56	100%	0%
SMW (Silicon Match Water)	2.07	62%	38%
4MW	4	33%	67%
D_2O (Pure D_2O)	6.35	0%	100%

Table B.1: **List of Four Contrasts of Liquid Buffers and Their Composition**.

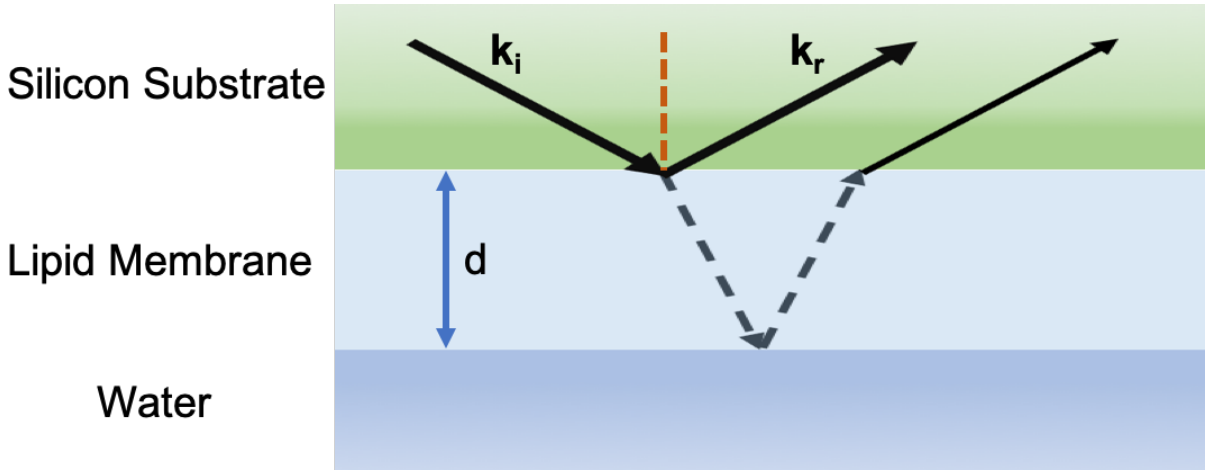


Figure B.1: Illustration of reflections of an incident beam on silicon/membrane and membrane/water interfaces.

two interfaces. In an actual experiment, there are typically more than just these two interfaces. Because the lipid tails and head groups have different SLD values in response to the neutron beam, each interface between two differing SLD values is considered a new reflection plane. When more molecules, such as the Aβ peptide, are introduced into the system, they create additional reflection interfaces depending on the location of the molecular layer buildup. Reflections at different interfaces yield distinct peaks on the spectrum, which can then be analyzed to deduce the distribution of substances in the z-direction.

In the NR study, we used simple model (SPM) as the model lipid membrane to study its interaction with Aβ peptide. We used 4 contrasts: H_2O, D_2O, 4WM and SWM in this

study. Preliminary results show that amyloid could interact with the supported membrane and penetrate into the membrane to create a new reflectivity profile on the opposite side of the membrane (between the membrane and the silicon substrate).

B.4 Preliminary Results

Data presented in Figure B.2 were fitted using the error function model approach, in which each part of the sample along the z-axis is described using error functions. From this model, the SLD profile is calculated and processed using the Parrat formalism (slab method). The fitting process relies on the minimization of χ^2, based initially on the simulated annealing algorithm and subsequently on the steepest descent method. Figures B.2 and B.3 display the reflectivity profiles and the layer distribution of the SPM before the addition of amyloid. A multilamellar formation is evident (indicated by black arrows) and can be fitted using a second layer with a coverage of 3% and a distance of around 80 $\AA$ as seen in Figure B.2. Figure B.3 presents the volume fraction distribution model obtained from the fit. The lipid head group is not directly connected to the substrate; instead, there is a hydration layer between the two layers.

Figures B.4 and B.5 show the reflectivity profiles and the layer distribution of the SPM after the addition of amyloid.In Figure B.4, the fit of the three contrasts after the addition of the peptide. The arrows indicate the presence of bragg peaks from the multilamellar contribution (that persists even after the peptide addition). In this model the multilamellarity is not considered, to avoid the over parametrization of the model. The position of the error function describing the Aβ was left free to move along the z-axis, giving at the end the best position that gave the best chi square. The final model is shown in Figure B.5. There is amyloid distribution between the silicon substrate and the lipid membrane, indicating its ability in penetrating through the membrane, which is in agreement with previous research findings on other membrane models [209].

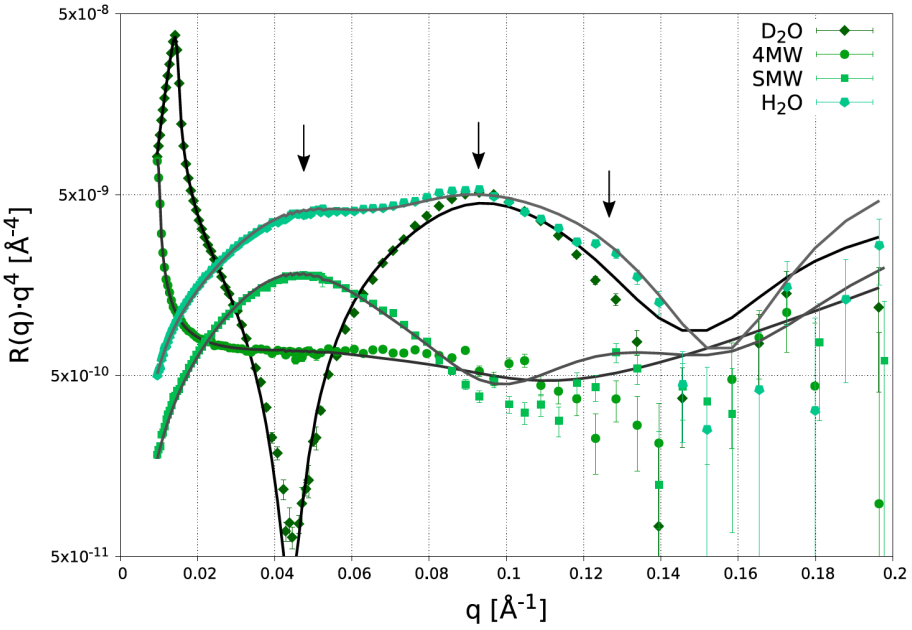


Figure B.2: Neutron reflectivity profiles and fitted curves of the SPM lipid membrane before adding Aβ.

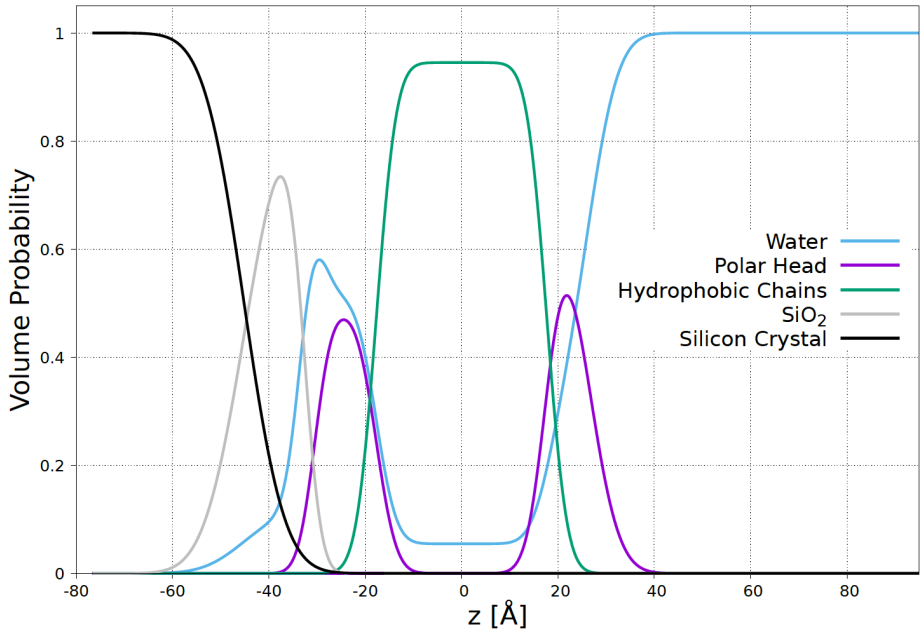


Figure B.3: Density profiles of each layer from fitted curves before adding Aβ.

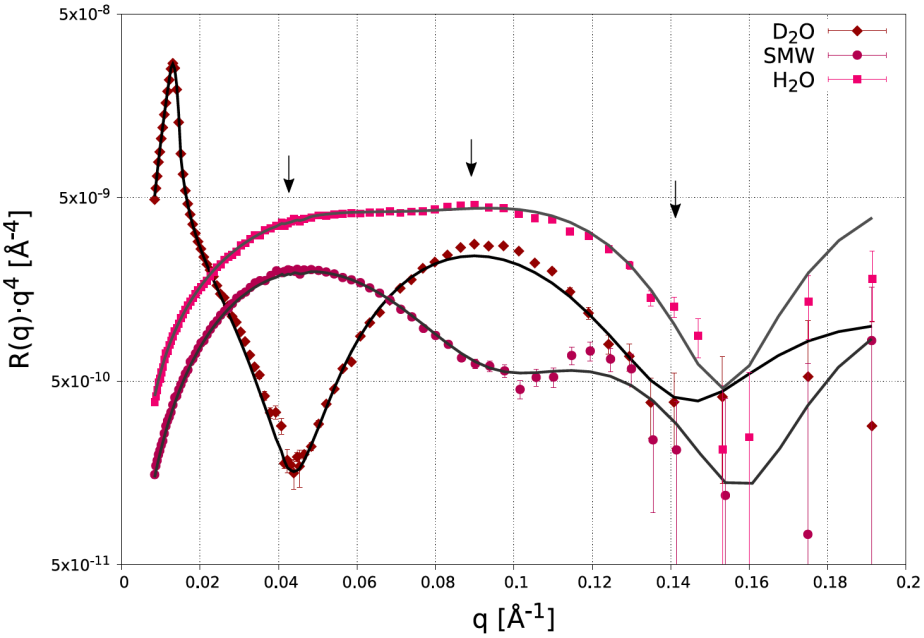


Figure B.4: Neutron reflectivity profiles and fitted curves of the SPM lipid membrane after adding Aβ.

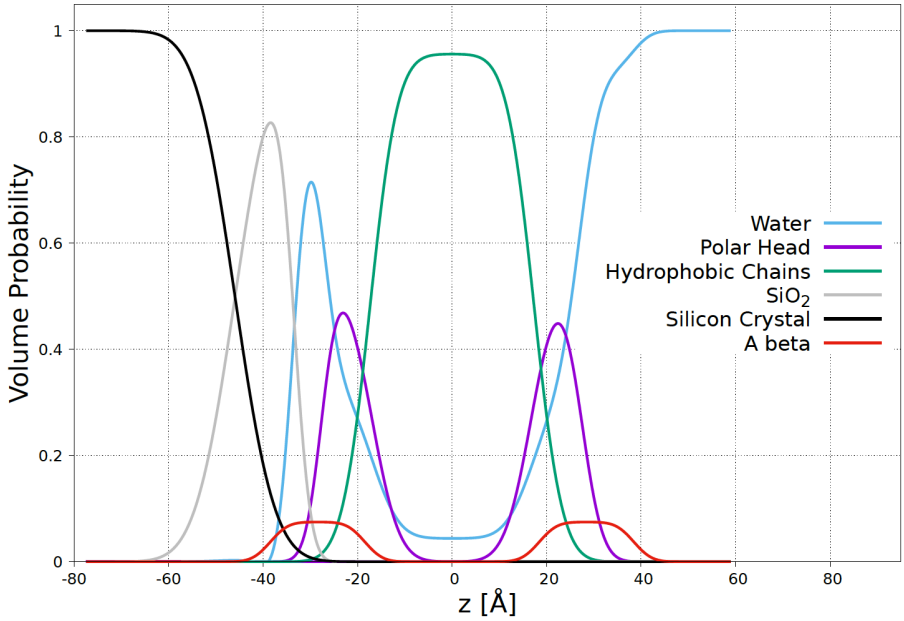


Figure B.5: Density profiles of each layer from fitted curves after adding Aβ.

B.5 Next Steps

While all experiments for this project have been accomplished, data analysis is still ongoing. Apart from the preliminary results shown here, further careful analysis is needed. We expect the outcome of this research to show that the membrane thickness (both head groups and tail groups) varies at different temperatures. Amyloid penetration, resulting in the formation of an amyloid layer on the opposite side of the membrane, would also impact the membrane structure.

Appendix C

High-Speed Atomic Force Microscopy to Study the Dynamics of the Membrane-Amyloid Interaction in the Presence and Absence of Melatonin

C.1 Overview

The high-speed AFM study was funded through a research fellowship by the Nano Life Science Institute (NanoLSI) at Kanazawa University in Japan, hosted by Professor Takeshi Fukuma. Assistant Professors Ayumi Sumino and Ayhan Yurtsever, as well as lab manager Dr. Weilin Wei, collaborated with us on the experimental design and provided invaluable assistance during data acquisition.

The overall goal of this project is to verify that melatonin associates with lipid bilayers so that it changes the lipid surface domain structure, and to determine if the presence of melatonin affects amyloid interaction with the lipid bilayers.

C.2 High-Speed Atomic Force Microscopy

The principle of atomic force microscopy (AFM) has been discussed in the method introduction section. High-speed (HS) AFM inherits all physical principles involved AFM. The HS-AFM a derived AFM technique that allows repeated imaging on the same area of the sample surface. In AFM for biological samples, a sharp-tipped micro-cantilever oscillates and intermittently contacts the sample. This movement is detected using an optical system and converted into a topographical image. Traditional AFM systems face limitations in scan speed, affecting the feedback control that maintains constant interaction between the tip and the sample. HS-AFM was developed to overcome these limitations, employing various techniques and devices, including shorter cantilevers and advanced feedback controls. Established in 2008, HS-AFM can achieve speeds of up to 15 frames per second for imaging individual protein molecules without disrupting their function [210].

Casuso *et al.* used HS-AFM to investigate the movement, dynamics, and arrangement of unlabelled outer membrane protein F (OmpF) in E. coli lipid membranes. They managed to collected videos on frame rate of 477 ms in a 750 $\mathring{A}$ area [211].

In our study with HS-AFM, lipid membrane models SPM, HM and EDM were studied. Amyloid interactions with the supported lipid membranes were recorded over a 2-hour video range. 400 μM melatonin was added to the experimental group to observe any effect on amyloid-membrane interaction.

Data acquisition for this study has been completed, but data analysis has not yet started. I will continue to analyze the data after submitting this thesis.